Received: Added at production | Revised: Added at production | Accepted: Added at production

DOI: xxx/xxxx

RESEARCH ARTICLE

The Shifted Fracture Method

Kangan Li[1] | Nabil M. Atallah[1] | Antonio Rodríguez-Ferran[2] | Dakshina M. Valiveti[3] | Guglielmo Scovazzi*[1]

[1]Department of Civil and Environmental Engineering, Duke University, Durham NC 27708, U.S.A.
[2]Laboratori de Càlcul Numèric (LaCàN), Universitat Politècnica de Catalunya, BarcelonaTech, Barcelona, Spain
[3]Computational & Data Sciences Research Department, ExxonMobil Upstream Research Company, Spring, TX 77389, U.S.A.

Correspondence
*Guglielmo Scovazzi, Department of Civil and Environmental Engineering, Duke University, Durham, NC 27708, USA.
Email: guglielmo.scovazzi@duke.edu

Summary

We propose a new framework for fracture mechanics, based on the idea of an approximate fracture geometry representation combined with approximate interface conditions. Our approach evolves from the shifted interface method, and introduces the concept of an approximate fracture surface composed of the full edges/faces of an underlying grid that are geometrically close to the true fracture geometry. The original interface conditions are then modified on the surrogate fracture geometry, by way of Taylor expansions. The shifted fracture method does not require cut cell computations or complex data structures, since the behavior of the true fracture is mimicked with standard integrals on the approximate fracture surface. Furthermore, the energetics of the true fracture are represented within the accuracy of the underlying polynomial finite element approximation and independently of the grid topology. The computational framework is presented here in its generality and then applied in the specific context of cohesive zone models, with an extensive set of numerical experiments in two and three dimensions.

KEYWORDS:
Shifted boundary method; shifted interface method; fracture mechanics; approximate boundary conditions; embedded methods; extended finite element method

1 | INTRODUCTION AND OVERVIEW

This work presents the Shifted Fracture Method (SFM) as a new computational framework for fracture mechanics. The SFM is based on the idea of approximating the fracture interface conditions on an approximate fracture geometry (the surrogate fracture) that coincides with the edges/faces of the grid that are closest, in some sense, to the true fracture geometry.

The term "shifted" in the name of the method derives from the fact that the fracture conditions are modified (shifted, in fact) in *both location and value* with the purpose of mimicking the true fracture interface conditions on the true geometry of the fracture. It is important to realize that shifting only the location of the interface conditions would produce a computational method analogous to the node-release technique [1–4], with the consequent drawback of mesh dependency of the numerical results.

Instead, by shifting also the value of the fracture interface conditions, the SFM is not affected by such mesh dependencies, and its variational formulation automatically incorporates the projection of the surrogate surface area onto the true surface area, which is instrumental in the representation of the correct energy released by the fracture.

In order to put into perspective the SFM, we attempt to present a brief - and certainly not comprehensive - account of the earlier and most recent contributions to computational fracture mechanics. Some of the earliest computational strategies to simulate fracture propagation problems involve the node-release technique [1–4] and the element deletion approach [4]. In the node release

technique, the fracture is numerically represented by duplicating displacement degrees-of-freedom along the edges/faces of the computational grid in two/three dimensions, and applying appropriate cohesive zone models on the numerical crack faces. The propagation of the fracture cannot then follow an arbitrary direction, but must follow along the edges/faces of the computational grid. With this strategy, the surface area of the fracture is incorrectly captured, and consequently, large errors in fracture release energy may occur. To correct these issues, adaptive mesh refinement can be used to allow the grid to align with the theoretical direction of propagation of the fracture, and alleviate the problem of incorrect fracture surface representations. The drawback of these techniques is the added complexities of managing remeshing data structures as the fracture propagates and the need to transfer information from the old mesh to the new mesh at each adaptive refinement.

More recently, Lew and collaborators developed the Universal Meshes algorithm[5,6], in which a base computational grid is locally adapted as the fracture propagates through the domain. This approach avoids mesh dependencies by mesh adaptation, and has been implemented also in the context of higher-order discretizations[7,8].

Mesh dependencies in the behavior of the fracture are also observed when considering element-deletion techniques[4], and more generally fracture damage modeling techniques[9,10]. There, a damage model is introduced to reduce the stiffness of elements that lie in proximity of a fracture. In their simplest implementation in conjunction with piecewise-linear finite element approximations of the displacements, also element damage models do not correctly capture the energy released in the fracture[11–13]. Part of the limitations of element deletion techniques is due to the piecewise-constant approximation of the stresses (or strains), which is not sufficient to prevent large mesh dependencies in the numerical solution. In a recent development, the authors of[14–21] proposed a new breed of damage models based on mixed formulations of the equations of elasticity, which allow higher-order stresses approximations and avoid the mesh dependencies of earlier contributions. The numerical results are certainly promising and somewhat "resuscitate" methods that have in the simplicity of implementation their strong point.

Over the past two decades, the computational fracture mechanics community explored ideas aimed at circumventing the limitation of node-release techniques. The literature is vast, and a full account is possibly beyond the scope of this work. Nonetheless, it is important to mention a number of essential contributions.

By relating the loss of ellipticity of the partial differential equations governing the classical continuum model to the development of strong discontinuities, Simo *et al.*[22] proposed a general localized failure framework that was later expanded by Armero and Garikipati[23].

Embedded Finite Element Methods (EFEMs) were proposed by several groups[23–30], and rely on the idea of augmenting the finite element shape functions with appropriate enrichments that can be used to approximate the kinematics of the crack. These methods are typically distinguished in approaches with strong discontinuities (introducing displacement jumps)[23,25–29,31] or with weak discontinuity (introducing strain jumps)[24,30,32]. The latter approach is more applicable in the case in which an obvious jump in strains occurs, such as in shear bands of metals and soils. Weak enrichment EFEMs enrich the strains with incompatible modes, and result in non-conforming finite elements, in which, typically, the surface of the fracture is approximated as a globally discontinuous geometric object. Weak enrichment EFEMs typically require a length scale parameter to define the width of the strain jump and as yet have been unable to overcome mesh dependencies[33]. In strong enrichment EFEMs, by means of appropriately constructed enhanced shape functions, elements can properly capture the highly localized modes that prelude failure. Recent developments in this area are found in[34–38].

Later, the eXtended FEM (or XFEM)[39–41] and the Generalized FEM (GFEM)[42–45] were introduced to have a more general description of the kinematic fields in proximity of the fracture, allowing the enrichments to be much more general than in the earlier EFEM. From a general perspective, XFEMs/GFEMs can be considered as Partition of Unity FEMs[46,47], in which the standard finite element basis is locally enriched to represent the displacement and stress fields in close proximity of the fracture. A large body of literature has since been developed, and here we would like to point out the contributions in the realm of cohesive-zone models[48–50], which are the focus of the present work.

On a completely different area of development, new damage models were developed using variational principles to control and drive the evolution of cracks. These approaches follow under the name of gradient damage models[51–53], phase-field models[54–57], and have provided very important tools to numerically simulate crack nucleation, branching and merging. These methods are based on a diffuse representation of the fracture, and the introduction of a damage variable that controls the evolution of fractures. By relying on gradient information, phase-field and gradient damage models are intrinsically nonlocal models, although they rely on a classical partial differential equation description of the fields representing the fracture process. For this reason, they are simpler to implement than nonlocal damage models of the integral type[58,59], as they do not require the computation of a nonlocal state variable as the weighted average of a local state variable in a neighborhood of each point of the computational domain.

An alternative nonlocal approach to fracture is Peridynamics (PD)[60–64], in which the equations of continua are reformulated as an integro-differential equation. At the price of an increased computational cost, PD offers a more general and comprehensive approach to fracture, and has found various implementations, including meshfree/meshless algorithms[65], which had already been proposed as a tool to study crack propagation problems[66–68]. PD shares with phase-field algorithms the ability to more easily attack crack branching and nucleation, although the technical reasons are different.

We would like now to make a few comments on two of the approaches to fracture mentioned above, namely XFEM and phase-field models. As previously mentioned, The XFEM represents the fracture as a sharp interface that can cut across finite elements, and obviates to the severe grid-dependence issues associated with earlier models. It is however of difficult implementation in three-dimensions, since it requires special data structures and special integration procedures that are hard to implement. At the same time the numerical stability and the algebraic system of equations associated with XFEM variational formulation may be affected by the presence of small-cut elements, and a number of stabilization approaches have been proposed[69–73].

Phase-field models, instead, resort to an energetic principle for the characterization of the numerical fracture, and are of easier implementation in the three-dimensional case. However, they introduce a diffuse representation of the fracture itself, and they may be, for this reason, less efficient in the numerical representation of the fracture away from the crack tip. In addition, the location of the crack is not directly given in a phase-field model, but this might be important in studying problems in which other physics are coupled to the propagation of fracture, such as the case of fractured porous media with flow coupling, etc. An approach that blends a phase-field model and a sharp crack representation was presented in[74–76].

The SFM approach described here evolves from the Shifted Interface Method[77,78], an approximate domain approach, in which interfaces are approximated by the set of closest edges on the grid, and interface conditions are appropriately modified (shifted), using Taylor expansions, to achieve a prescribed level of accuracy. In this work, we describe how these ideas can be used in general, and more specifically in the context of cohesive zone models. The description of the crack relies on the definition of a distance (vector) between the location of the true crack (or a sufficiently accurate estimate of it), and the location of the surrogate crack. The SFM does not require cut cell computations or complex data structures, since the behavior of the true fracture is mimicked with standard integrals on the approximate fracture, which preserves the energetics of the true fracture to a high degree of accuracy. In fact, the SFM adopts the same integration quadratures and data structures utilized in common node-release techniques. In this sense, the SFM stands as an interesting alternative to both node-release techniques and XFEM/GFEM approaches, in that it has the computational data structure of a node-release technique but the accuracy of a XFEM/GFEM.

This article is organized as follows: Section 2 describes the classical framework of cohesive zone models and its variational formulation for an XFEM/GFEM approach; Section 3 presents the formalism of the SFM, a general mixed displacement-strain SFM variational formulation, and a simplified version of the same with computational cost comparable to the standard primal displacement formulation; Section 4 describes the details of the SFM implementation from the point of view of nonlinear solution methods and crack propagation strategies; and a comprehensive suite of two- and three-dimensional tests are presented in Section 5.

2 | A COHESIVE APPROACH TO FRACTURE PROPAGATION

In this work we consider fracture propagation problems in linearly elastic solids under the assumption that a *cohesive law* governs the Fracture Process Zone (FPZ). This scenario is typical of cases in which linear elastic fracture mechanics (LEFM) is not applicable, that is when the FPZ at the crack tip is *not* small compared to the size of the crack and the size of the specimen[79]. Cohesive laws have been pioneered in the works of Dugdale[80], Barenblatt[81] and Hillerborg[82], and rely on traction-displacement relations on the portion of the crack faces inside the FPZ to propagate fractures.

Geometrically, a fracture can be described as an embedded interface as depicted in Figure 1. There, Ω is a connected open set in $\mathbb{R}^d$ with Lipschitz boundary $\partial\Omega$ (where $d = 2, 3$ indicates the number of spatial dimensions), Γ_c is the fracture interface, Γ_{coh} is the cohesive zone (the part of Γ_c where cohesive tractions are different from zero), and $\boldsymbol{A}$ is the crack tip.

2.1 | A mixed form of the equations of elasticity

The equations of linear isotropic elastostatics describe the deformation of a solid medium under prescribed external loading. In what follows, we will consider a mixed formulation in terms of displacement and strain variables, since this approach guarantees the possibility of imposition of Dirichlet, Neumann and fracture interface conditions using the shifted boundary approach[83].

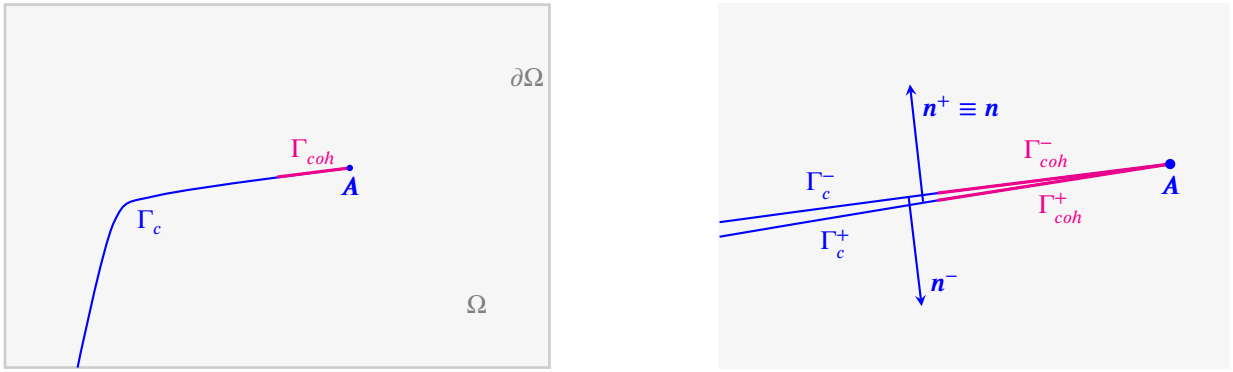

FIGURE 1 The (true) fracture path Γ_c, the cohesive zone Γ_{coh}, and the fracture tip $\boldsymbol{A}$. A zoomed view in the vicinity of the crack tip is presented on the right.

Consider the following displacement/strain mixed form of the linear elastostatics equations:

$$\boldsymbol{0} = \boldsymbol{b} + \nabla \cdot \boldsymbol{\sigma}(\boldsymbol{\varepsilon}) \,, \tag{1a}$$

$$\boldsymbol{\varepsilon} = \nabla^s \boldsymbol{u} \,. \tag{1b}$$

Here, $\boldsymbol{b}$ is a body force, ∇ and $\nabla\cdot$ are the gradient and divergence operators, respectively, $\boldsymbol{\sigma}$ is the stress tensor, and $\boldsymbol{\varepsilon}$ is the strain tensor defined as the symmetric gradient of the displacement field $\boldsymbol{u}$, namely $\nabla^s \boldsymbol{u} = 1/2 \left(\nabla \boldsymbol{u} + \nabla^t \boldsymbol{u} \right)$, where $(\cdot)^t$ is the transpose (or adjoint) operator. For elastic materials, the underlying stress-strain constitutive law is

$$\boldsymbol{\sigma}(\boldsymbol{\varepsilon}) = \mathbf{C}\, \boldsymbol{\varepsilon} \,, \tag{2}$$

where $\mathbf{C} = [\mathsf{C}_{ijkl}]$ is the fourth-order elastic stiffness tensor. For isotropic materials, $\mathbf{C}$ collapses to

$$\mathsf{C}_{ijkl} = \lambda \delta_{ij} \delta_{kl} + \mu (\delta_{ik} \delta_{jl} + \delta_{il} \delta_{jk}) \,. \tag{3}$$

Here λ and μ are the Lamé coefficients, which are related to the Young's modulus E, the Poisson ratio ν, the bulk modulus κ, and the shear modulus G by:

$$\lambda = \frac{E\nu}{(1+\nu)(1-2\nu)} \,, \quad \mu = G = \frac{E}{2(1+\nu)} \,, \quad \kappa = \lambda + 2\mu/3 \,. \tag{4}$$

Under these hypotheses, (2) reduces to

$$\boldsymbol{\sigma}(\boldsymbol{\varepsilon}) = \lambda \, \mathrm{tr}(\boldsymbol{\varepsilon}) \boldsymbol{I} + 2\mu \, \boldsymbol{\varepsilon} \,, \tag{5}$$

where $\mathrm{tr}(\boldsymbol{\varepsilon})$ is the trace of the strain tensor $\boldsymbol{\varepsilon}$ (ε_{kk} in the Einstein repeated index notation). Assuming that the boundary $\Gamma = \partial\Omega$ is partitioned as $\overline{\Gamma_D \cup \Gamma_N}$ with $\Gamma_D \cap \Gamma_N = \emptyset$, displacement boundary conditions

$$\boldsymbol{u}_{|\Gamma_D} = \boldsymbol{u}_D(\boldsymbol{x}) \tag{6a}$$

are enforced on Γ_D and traction boundary conditions

$$\boldsymbol{\sigma}(\boldsymbol{\varepsilon})\, \boldsymbol{n}_{|\Gamma_N} = (\mathbf{C}\, \boldsymbol{\varepsilon})\, \boldsymbol{n}_{|\Gamma_N} = \boldsymbol{t}_N(\boldsymbol{x}) \tag{6b}$$

are enforced on Γ_N, where $\boldsymbol{t}_N$ is the normal traction and $\boldsymbol{n}$ is the outward-pointing normal to the boundary Γ_N.

2.2 | A Cohesive Zone Model

We consider a cohesive zone model that is commonly adopted in many computational approaches to fracture mechanics (see, e.g.,[48] for its application in the XFEM). In particular, we consider a generalized approach that encompasses Mode I and Mode II fracture propagation by means of a constitutive relation between an equivalent traction and an equivalent fracture opening[3,84–88]. The discussion that follows should not be considered as restricted to the particular cohesive zone model chosen, but can easily be generalized to virtually any cohesive zone model.

Consider the crack faces (i.e., the opposite surfaces of the crack on Γ_c shown in the right panel of Figure 1) and their respective normals $\boldsymbol{n}^+$ and $\boldsymbol{n}^-$, such that $\boldsymbol{n}^+ = -\boldsymbol{n}^- = \boldsymbol{n}$. A cohesive zone model relies on the definition of *cohesive tractions* $\boldsymbol{t}^+$ and $\boldsymbol{t}^-$

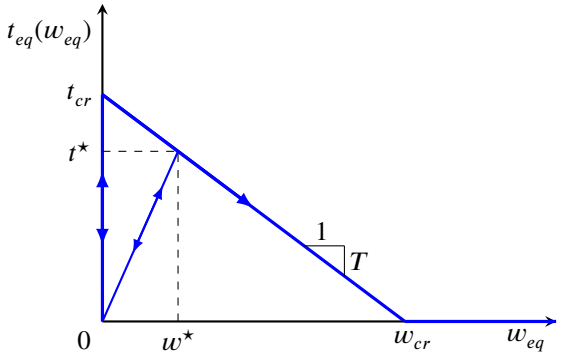

FIGURE 2 The cohesive law $t_{eq}(w_{eq})$.

on the faces of the crack inside the cohesive zone Γ_{coh}. Outside the cohesive zone, that is over the set $\Gamma_c \setminus \Gamma_{coh}$, the cohesive tractions take the zero value. Hence, the cohesive zone model enforces the traction boundary condition

$$\boldsymbol{t} = \boldsymbol{t}_{coh}(\boldsymbol{w}) \quad \text{on } \Gamma_c \,, \tag{7}$$

with $\boldsymbol{t}_{coh} = \boldsymbol{0}$ on $\Gamma_c \setminus \Gamma_{coh}$, where the *crack opening* $\boldsymbol{w} = \boldsymbol{w}(\boldsymbol{u})$ along Γ_c is defined as

$$\boldsymbol{w}(\boldsymbol{u}) = \boldsymbol{u}^- - \boldsymbol{u}^+ = [\![\boldsymbol{u}]\!] \,, \tag{8}$$

in which $[\![\chi]\!] = \chi^- - \chi^+$ is the jump function. Note that the cohesive tractions must equilibrate, that is

$$\boldsymbol{t} \equiv \boldsymbol{t}^+ = \boldsymbol{\sigma}(\boldsymbol{\varepsilon})^+ \cdot \boldsymbol{n}^+ = -\boldsymbol{\sigma}(\boldsymbol{\varepsilon})^- \cdot \boldsymbol{n}^- = -\boldsymbol{t}^- \quad \text{on } \Gamma_c \,. \tag{9}$$

The traction $\boldsymbol{t}_{coh}$ can be decomposed into a normal and tangential component, namely

$$\boldsymbol{t}_{coh} = t_n \boldsymbol{n} + t_s \boldsymbol{\tau} \,, \tag{10a}$$

$$t_n = \boldsymbol{t}_{coh} \cdot \boldsymbol{n} \,, \tag{10b}$$

$$t_s = \boldsymbol{t}_{coh} \cdot \boldsymbol{\tau} \,, \tag{10c}$$

where t_n is the component of the traction normal to the fracture surface and t_s is the component of the traction tangent to the fracture (the sliding component, along a unit vector $\boldsymbol{\tau}$ that is given as a linear combination of the unit vectors $\boldsymbol{\tau}_i$, for $i = 1, \ldots, d-1$). Similarly, the crack opening $\boldsymbol{w}(\boldsymbol{u})$ can be decomposed as

$$\boldsymbol{w}(\boldsymbol{u}) = w_n \boldsymbol{n} + w_s \boldsymbol{\tau} \,, \tag{11a}$$

$$w_n = \boldsymbol{w}(\boldsymbol{u}) \cdot \boldsymbol{n} \,, \tag{11b}$$

$$w_s = \boldsymbol{w}(\boldsymbol{u}) \cdot \boldsymbol{\tau} \,. \tag{11c}$$

In the generalized cohesive models described in [86–88], an equivalent crack opening w_{eq} is introduced, and defined as

$$w_{eq} = \sqrt{w_n^2 + \beta^2 w_s^2} \,, \tag{12}$$

where β is a model parameter. The normal and sliding component of the traction are then expressed as

$$t_n = t_{eq}(w_{eq}) \frac{w_n}{w_{eq}} \,, \tag{13a}$$

$$t_s = \beta^2 \, t_{eq}(w_{eq}) \, \frac{w_s}{w_{eq}} \,, \tag{13b}$$

where these expressions are motivated by considerations on the energetic consistency of the constitutive model. The complete specification of the cohesive zone model involves the definition of the function $t_{eq}(w_{eq})$, which in our case is given as [87,88]

$$t_{eq}(w_{eq}) = \begin{cases} t_{cr} - T w_{eq} & \text{for } 0 < w_{eq} = w^\star < w_{cr} \,, \ \dot{w}^\star > 0 \,, \\ \dfrac{t^\star}{w^\star} \, w_{eq} \,, & \text{for } 0 \le w_{eq} < w^\star < w_{cr} \,, \ \dot{w}^\star = 0 \,, \\ 0 \,, & \text{for } w_{eq} \ge w_{cr} \,, \end{cases} \tag{13c}$$

and is graphically depicted in Figure 2. The extent of the cohesive zone is implicitly defined by way of a critical crack opening parameter w_{cr}, used in the definition of the cohesive traction $\boldsymbol{t}_{coh}$. The interpretation of the cohesive law function $t_{eq}(w_{eq})$ is as follows: the traction force follows a rigid response until the value t_{cr} is reached (the vertical segment from the origin to the point $(0, t_{cr})$ in Fig. 2), at which point the crack faces are allowed to separate ($w_{eq} > 0$) and the cohesive traction follows the line $t_{cr} - T w_{eq}$ (i.e., the cohesive branch). Note also that $T = t_{cr}/w_{cr} > 0$ is the magnitude of the (negative) slope of the linear profile of the cohesive traction law and that, by definition, $t_{eq}(w_{eq}) \geq 0$, which implies that the cohesive traction acts to close the fracture opening. In particular, the state $w \geq w_{cr}$, for which $t_{eq}(w_{eq}) = 0$, corresponds to points on $\Gamma_c \setminus \Gamma_{coh}$. Hence, the range of values $0 < w < w_{cr}$, for which $t_{eq}(w_{eq}) > 0$, implicitly defines Γ_{coh}. In the case in which unloading occurs in the cohesive zone, a history variable $w^\star$ tracks the largest (equivalent) crack opening achieved at a point on the crack surface, and the unloading/reloading occurs along the line $(t^\star/w^\star)w_{eq}$, which is also called the unloading/reloading branch (see again Fig. 2).

The boundary value problem associated with crack propagation involves the solution of (1) under the elastic constitutive law (2), the (outer) boundary conditions (6) and the fracture interface conditions (7). We also define the fracture energy

$$G_F = \int_0^{w_{cr}} t_{eq}(w_{eq}) \, \mathrm{d}w \, , \tag{14}$$

which collapses to $G_F = t_{cr} w_{cr}/2$ for the model at hand.

Remark 1. A well-known drawback of the model presented here is its inability to prevent the interpenetration of the crack faces (i.e., a negative crack opening w). Hence, the reader should not take this model too literally, but consider it instead as an example in the much broader realm of application of the shifted fracture approach.

Remark 2. Note that, for some cohesive zone models, the cohesive zone Γ_{coh} extends over the entire crack surface Γ_c, that is $\Gamma_c \setminus \Gamma_{coh} = \emptyset$. This is the case, for example, when the cohesive law has an exponential scaling, that is $t_{eq}(w_{eq}) = t_{cr} e^{-w_{eq}/w_{cr}}$. The discussion that follows on the shifted fracture approach can easily be adapted to this case, and other variations on this theme.

2.3 | Variational equations

Throughout the rest of the exposition, we will use the Sobolev spaces $H^m(\Omega) = W^{m,2}(\Omega)$ of index of regularity $m \geq 0$ and index of summability 2, equipped with the (scaled) norm

$$\|v\|_{H^m(\Omega)} = \left(\|v\|^2_{L^2(\Omega)} + \sum_{k=1}^{m} \|l(\Omega)^k \boldsymbol{D}^k v\|^2_{L^2(\Omega)} \right)^{1/2} , \tag{15}$$

where $\boldsymbol{D}^k$ is the kth-order spatial derivative operator and $l(A) = (\mathrm{meas}(A))^{1/d}$ is a characteristic length of the domain A. Note that $H^0(\Omega) = L^2(\Omega)$. As usual, we use a simplified notation for norms and semi-norms, i.e., we set $\|v\|_{m;\Omega} = \|v\|_{H^m(\Omega)}$ and $|v|_{k;\Omega} = \|\boldsymbol{D}^k v\|_{0;\Omega} = \|\boldsymbol{D}^k v\|_{L^2(\Omega)}$. In the sequel, $(u, v)_\omega = \int_\omega u \, v \, \mathrm{d}\omega$ denotes the L^2 inner product on a subset $\omega \subset \Omega$ and $\langle u, v \rangle_\zeta = \int_\zeta u \, v \, \mathrm{d}\zeta$ denotes the L^2 inner product on the subset $\zeta \subset \partial\Omega \cup \Gamma_c$.

We consider now a general variational formulation in the context of the infinite-dimensional solution spaces

$$\mathscr{S}_{\boldsymbol{u}}(\Omega \setminus \Gamma_c) = \left\{ \boldsymbol{v} \in \left(H^1(\Omega \setminus \Gamma_c) \right)^d \ : \ \boldsymbol{v}_{|\Gamma_D} = \boldsymbol{u}_D \right\} , \tag{16a}$$

$$\mathscr{S}_{\boldsymbol{\varepsilon}}(\Omega \setminus \Gamma_c) = \left(H^1(\Omega \setminus \Gamma_c) \right)^{d \times d} , \tag{16b}$$

$$\mathscr{V}_{\boldsymbol{u}}(\Omega \setminus \Gamma_c) = \left\{ \boldsymbol{v} \in \left(H^1(\Omega \setminus \Gamma_c) \right)^d \ : \ \boldsymbol{v}_{|\Gamma_D} = \boldsymbol{0} \right\} , \tag{16c}$$

$$\mathscr{V}_{\boldsymbol{\varepsilon}}(\Omega \setminus \Gamma_c) = \mathscr{S}_{\boldsymbol{\varepsilon}}(\Omega \setminus \Gamma_c) \, , \tag{16d}$$

where $H^k(\Omega \setminus \Gamma_c)$ is the Sobolev space of square-integrable functions with square-integrable weak derivatives up to order k, except at the interface Γ_c, that is, on the open set $\Omega \setminus \Gamma_c$. Here $\mathscr{S}_{\boldsymbol{u}}(\Omega \setminus \Gamma_c)$ and $\mathscr{S}_{\boldsymbol{\varepsilon}}(\Omega \setminus \Gamma_c)$ are the set of functions that represent the solution for displacements and strains, and $\mathscr{V}_{\boldsymbol{u}}(\Omega \setminus \Gamma_c)$ and $\mathscr{V}_{\boldsymbol{\varepsilon}}(\Omega \setminus \Gamma_c)$ are the corresponding test function spaces.

Multiplying (1a) and (1b) by $\boldsymbol{\phi} \in \mathscr{V}_u(\Omega \setminus \Gamma_c)$ and $\boldsymbol{\psi} \in \mathscr{V}_{\boldsymbol{\varepsilon}}(\Omega \setminus \Gamma_c)$, we obtain

$$-(\boldsymbol{\phi}, \nabla \cdot \boldsymbol{\sigma}(\boldsymbol{\varepsilon}))_{\Omega \setminus \Gamma_c} = (\boldsymbol{\phi}, \boldsymbol{b})_{\Omega \setminus \Gamma_c} \, , \tag{17a}$$

$$(\boldsymbol{\psi}, \boldsymbol{\varepsilon})_{\Omega \setminus \Gamma_c} = (\boldsymbol{\psi}, \nabla^s \boldsymbol{u})_{\Omega \setminus \Gamma_c} \, . \tag{17b}$$

Equation (9) can be recast in a form of wider applicability when considering the variational statements associated with cohesive zone models. Defining the λ-weighted average $\{\!\{\chi\}\!\}_\lambda = \lambda\chi^+ + (1-\lambda)\chi^-$ of a quantity χ for any $\lambda \in [0,1]$, we can observe that (9) implies two important identities, namely

$$[\![\boldsymbol{\sigma}(\boldsymbol{\varepsilon})]\!]\boldsymbol{n} = \boldsymbol{0} \quad \text{and} \quad \{\!\{\boldsymbol{\sigma}(\boldsymbol{\varepsilon})\}\!\}_\lambda \boldsymbol{n} = \boldsymbol{t}_{coh} \,. \tag{18}$$

Integrating by parts (17a) and accounting for the fact that the solution may not be smooth across Γ_c yields

$$(\nabla\boldsymbol{\phi}, \boldsymbol{\sigma}(\boldsymbol{\varepsilon}))_{\Omega\setminus\Gamma_c} - \langle\boldsymbol{\phi}, \boldsymbol{\sigma}(\boldsymbol{\varepsilon})\boldsymbol{n}\rangle_{\partial\Omega} + \langle[\![\boldsymbol{\phi}]\!], \{\!\{\boldsymbol{\sigma}(\boldsymbol{\varepsilon})\}\!\}_\lambda \boldsymbol{n}\rangle_{\Gamma_c} + \langle\{\!\{\boldsymbol{\phi}\}\!\}_{1-\lambda}, [\![\boldsymbol{\sigma}(\boldsymbol{\varepsilon})]\!]\boldsymbol{n}\rangle_{\Gamma_c} = (\boldsymbol{\phi}, \boldsymbol{b})_{\Omega\setminus\Gamma_c} \,, \tag{19}$$

where we have also used the identity $[\![\boldsymbol{\sigma}(\boldsymbol{\varepsilon})\boldsymbol{\phi}]\!] = \{\!\{\boldsymbol{\sigma}(\boldsymbol{\varepsilon})\}\!\}_\lambda [\![\boldsymbol{\phi}]\!] + [\![\boldsymbol{\sigma}(\boldsymbol{\varepsilon})]\!]\{\!\{\boldsymbol{\phi}\}\!\}_{1-\lambda}$ on Γ_c.

Without loss of generality, we assume that the Dirichlet boundary conditions are enforced strongly, which implies that $\boldsymbol{\phi}_{|\Gamma_D} = \boldsymbol{0}$. Thus, applying the Dirichlet boundary conditions (6a), the Neumann boundary conditions (6b), the cohesive law (13) on Γ_c, and recalling (18), equation (19) can be recast as

$$(\nabla\boldsymbol{\phi}, \boldsymbol{\sigma}(\boldsymbol{\varepsilon}))_{\Omega\setminus\Gamma_c} + \langle[\![\boldsymbol{\phi}]\!], \boldsymbol{t}_{coh}\rangle_{\Gamma_c} = (\boldsymbol{\phi}, \boldsymbol{b})_{\Omega\setminus\Gamma_c} + \langle\boldsymbol{\phi}, \boldsymbol{t}_N\rangle_{\Gamma_N} \,. \tag{20}$$

Combining equation (17b) with (20), we have the final weak form as:

$$(\nabla\boldsymbol{\phi}, \boldsymbol{\sigma}(\boldsymbol{\varepsilon}))_{\Omega\setminus\Gamma_c} + (\boldsymbol{\psi}, \boldsymbol{\varepsilon} - \nabla^s\boldsymbol{u})_{\Omega\setminus\Gamma_c} + \langle[\![\boldsymbol{\phi}]\!], \boldsymbol{t}_{coh}\rangle_{\Gamma_c} - (\boldsymbol{\phi}, \boldsymbol{b})_{\Omega\setminus\Gamma_c} - \langle\boldsymbol{\phi}, \boldsymbol{t}_N\rangle_{\Gamma_N} = 0 \,. \tag{21}$$

Remark 3. (Euler-Lagrangian equations). Integrating (21) back by parts, we obtain

$$-(\boldsymbol{\phi}, \nabla\cdot\boldsymbol{\sigma}(\boldsymbol{\varepsilon}))_{\Omega\setminus\Gamma_c} + (\boldsymbol{\psi}, \boldsymbol{\varepsilon} - \nabla^s\boldsymbol{u})_{\Omega\setminus\Gamma_c} - \langle[\![\boldsymbol{\phi}]\!], \{\!\{\boldsymbol{\sigma}(\boldsymbol{\varepsilon})\}\!\}_\lambda \boldsymbol{n}\rangle_{\Gamma_c} - \langle\{\!\{\boldsymbol{\phi}\}\!\}_{1-\lambda}, [\![\boldsymbol{\sigma}(\boldsymbol{\varepsilon})]\!]\boldsymbol{n}\rangle_{\Gamma_c} + \langle[\![\boldsymbol{\phi}]\!], \boldsymbol{t}_{coh}\rangle_{\Gamma_c}$$
$$- (\boldsymbol{\phi}, \boldsymbol{b})_{\Omega\setminus\Gamma_c} - \langle\boldsymbol{\phi}, \boldsymbol{t}_N\rangle_{\Gamma_N} = 0 \,, \tag{22}$$

which can be reformulated as

$$-(\boldsymbol{\phi}, \nabla\cdot\boldsymbol{\sigma}(\boldsymbol{\varepsilon}) + \boldsymbol{b})_{\Omega\setminus\Gamma_c} + (\boldsymbol{\psi}, \boldsymbol{\varepsilon} - \nabla^s\boldsymbol{u})_{\Omega\setminus\Gamma_c} - \langle\{\!\{\boldsymbol{\phi}\}\!\}_{1-\lambda}, [\![\boldsymbol{\sigma}(\boldsymbol{\varepsilon})]\!]\boldsymbol{n}\rangle_{\Gamma_c} - \langle[\![\boldsymbol{\phi}]\!], \{\!\{\boldsymbol{\sigma}(\boldsymbol{\varepsilon})\}\!\}_\lambda \boldsymbol{n} - \boldsymbol{t}_{coh}\rangle_{\Gamma_c}$$
$$+ \langle\boldsymbol{\phi}, \boldsymbol{\sigma}(\boldsymbol{\varepsilon})\boldsymbol{n} - \boldsymbol{t}_N\rangle_{\Gamma_N} = 0 \,, \tag{23}$$

and corresponds to

$$-\nabla\cdot\boldsymbol{\sigma} - \boldsymbol{b} = \boldsymbol{0} \,, \qquad \text{in } \Omega\setminus\Gamma_c \,, \tag{24a}$$
$$\boldsymbol{\varepsilon} - \nabla^s\boldsymbol{u} = \boldsymbol{0} \,, \qquad \text{in } \Omega\setminus\Gamma_c \,, \tag{24b}$$
$$\boldsymbol{\sigma}\boldsymbol{n} - \boldsymbol{t}_N = \boldsymbol{0} \,, \qquad \text{on } \Gamma_N \,, \tag{24c}$$
$$\{\!\{\boldsymbol{\sigma}\}\!\}_\lambda \boldsymbol{n} - \boldsymbol{t}_{coh} = \boldsymbol{0} \,, \qquad \text{on } \Gamma_c \,, \tag{24d}$$
$$[\![\boldsymbol{\sigma}]\!]\,\boldsymbol{n} = \boldsymbol{0} \,, \qquad \text{on } \Gamma_c \,, \tag{24e}$$

which enforce the governing equations (1), the (outer) traction boundary conditions (6b), the fracture interface conditions (7) and stress equilibration condition (9).

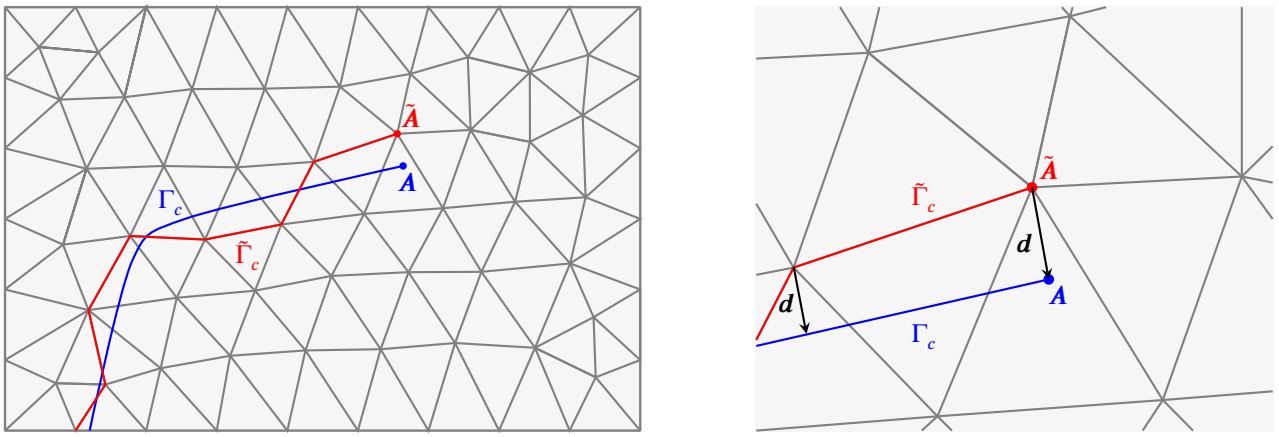

FIGURE 3 The fracture path Γ_c, the surrogate fracture path $\tilde{\Gamma}_c$, and the distance vector $\boldsymbol{d}$ at two locations along $\tilde{\Gamma}_c$.

3 | THE SHIFTED FRACTURE APPROACH

3.1 | The true crack, the surrogate crack and maps

Consider a family $\mathscr{T}_h$ of admissible and shape-regular triangulations of Ω, and assume that each triangulation is cut by the crack Γ_c, depicted as a blue curve in Figure 3.

The key idea in the *Shifted Fracture Method* is to shift the location where the fracture cohesive conditions are applied from the true location of the fracture Γ_c to a surrogate location $\tilde{\Gamma}_c$, represented by the red segmented curve in Figure 3, and to appropriately modify the interface conditions.

There are many ways to define the surrogate fracture. One way is to consider the edges (or faces) in $\mathscr{T}_h$ that are the closest to Γ_c in the sense of the closest point projection. We now define a mapping

$$\boldsymbol{M}_h : \tilde{\Gamma}_c \to \Gamma_c \,, \tag{25a}$$

$$\tilde{\boldsymbol{x}} \mapsto \boldsymbol{x} \,, \tag{25b}$$

using the closest point projection (see [89,90] for more details). $\boldsymbol{M}_h$ associates to any point $\tilde{\boldsymbol{x}} \in \tilde{\Gamma}_c$ on the surrogate crack a point $\boldsymbol{x} = \boldsymbol{M}_h(\tilde{\boldsymbol{x}})$ on the physical crack Γ_c and a corresponding distance vector function $\boldsymbol{d}_{\boldsymbol{M}_h}$, defined as

$$\boldsymbol{d}_{\boldsymbol{M}_h}(\tilde{\boldsymbol{x}}) \;=\; \boldsymbol{x} - \tilde{\boldsymbol{x}} \;=\; [\,\boldsymbol{M} - \boldsymbol{I}\,](\tilde{\boldsymbol{x}}) \,. \tag{26}$$

For the sake of simplicity, we set $\boldsymbol{d} = \boldsymbol{d}_{\boldsymbol{M}_h}$ where $\boldsymbol{d} = \|\boldsymbol{d}\|\boldsymbol{\nu}$ and $\boldsymbol{\nu}$ is a unit vector.

Remark 4. An alternative way of defining the map $\boldsymbol{M}_h$, and correspondingly the distance vector $\boldsymbol{d}$, is a level set description of the true crack, in which $\boldsymbol{d}$ is defined by means of a distance function.

3.2 | General strategy to shift cohesive zone conditions

The goal now is to discretize the linear elasticity equations (1a)–(1b) on Ω with outer boundary conditions (6a)–(6b) on Γ, and to modify the fracture interface conditions (24d)–(24e) so that they are applied on $\tilde{\Gamma}_c$ rather than Γ_c.

To this end, inspired by the ideas introduced in [78,91], a first-order Taylor expansion of $\boldsymbol{u}$ and $\mathbf{C}\,\boldsymbol{\varepsilon}$ is performed at the surrogate crack $\tilde{\Gamma}_c$, in order to "shift" (24d) – (24e) from Γ_c to $\tilde{\Gamma}_c$ (see for reference Figure 3). Thus,

$$\breve{\boldsymbol{u}}(\tilde{\boldsymbol{x}}) \;:=\; \boldsymbol{u}(\boldsymbol{M}_h(\tilde{\boldsymbol{x}})) = \boldsymbol{u}(\tilde{\boldsymbol{x}}) + (\nabla \boldsymbol{u}\, \boldsymbol{d})(\tilde{\boldsymbol{x}}) + \boldsymbol{R}_{\boldsymbol{u}}(\tilde{\boldsymbol{x}}) \,, \qquad \text{on } \tilde{\Gamma}_c \,, \tag{27a}$$

$$\breve{\boldsymbol{\sigma}}(\tilde{\boldsymbol{x}}) \;:=\; \boldsymbol{\sigma}(\boldsymbol{M}_h(\tilde{\boldsymbol{x}})) = \boldsymbol{\sigma}(\tilde{\boldsymbol{x}}) + (\nabla \boldsymbol{\sigma}\, \boldsymbol{d})(\tilde{\boldsymbol{x}}) + \boldsymbol{R}_{\boldsymbol{\sigma}}(\tilde{\boldsymbol{x}}) \,, \qquad \text{on } \tilde{\Gamma}_c \,, \tag{27b}$$

where we have defined the extension functions $\breve{\boldsymbol{u}}(\tilde{\boldsymbol{x}}) := \boldsymbol{u}(\boldsymbol{M}_h(\tilde{\boldsymbol{x}}))$ and $\breve{\boldsymbol{\sigma}}(\tilde{\boldsymbol{x}}) := \boldsymbol{\sigma}(\boldsymbol{M}_h(\tilde{\boldsymbol{x}}))$, and the remainders $\boldsymbol{R}_{\boldsymbol{u}}$ and $\boldsymbol{R}_{\boldsymbol{\sigma}}$ satisfy

$$\|\boldsymbol{R}_{\boldsymbol{u}}(\tilde{\boldsymbol{x}})\| = o(\|\boldsymbol{d}\|) \quad \text{and} \quad \|\boldsymbol{R}_{\boldsymbol{\sigma}}(\tilde{\boldsymbol{x}})\| = o(\|\boldsymbol{d}\|) \quad \text{as} \quad \|\,\boldsymbol{d}\,\| \to 0 \,. \tag{28}$$

Neglecting the remainders $\boldsymbol{R}_{\boldsymbol{u}}$ and $\boldsymbol{R}_{\boldsymbol{\sigma}}$, we have the approximation on $\tilde{\Gamma}_c$

$$\breve{\boldsymbol{u}}(\tilde{\boldsymbol{x}}) \approx \boldsymbol{S}(\boldsymbol{u})(\tilde{\boldsymbol{x}}) \,, \tag{29a}$$

$$\breve{\boldsymbol{\sigma}}(\tilde{\boldsymbol{x}}) \approx \boldsymbol{S}(\boldsymbol{\sigma})(\tilde{\boldsymbol{x}}) \,, \tag{29b}$$

where we have introduced the shift operators:

$$\boldsymbol{S}(\boldsymbol{u})(\tilde{\boldsymbol{x}}) \;:=\; \boldsymbol{u}(\tilde{\boldsymbol{x}}) + (\nabla \boldsymbol{u}\, \boldsymbol{d})(\tilde{\boldsymbol{x}}) \,, \tag{30a}$$

$$\boldsymbol{S}(\boldsymbol{\sigma})(\tilde{\boldsymbol{x}}) \;:=\; \boldsymbol{\sigma}(\tilde{\boldsymbol{x}}) + (\nabla \boldsymbol{\sigma}\, \boldsymbol{d})(\tilde{\boldsymbol{x}}) \,. \tag{30b}$$

Our goal is to enforce the cohesive zone model on the surrogate cohesive crack $\tilde{\Gamma}_c$ rather than on the true cohesive crack Γ_c (see again Figure 3). In order to maintain an optimal accuracy and avoid mesh dependencies, the cohesive zone model (7) also needs to be adapted appropriately. In particular, (7) can be used to express $\breve{\boldsymbol{t}}$ in terms of $\breve{\boldsymbol{u}}$ as

$$\breve{\boldsymbol{t}} = \breve{\boldsymbol{\sigma}}\breve{\boldsymbol{n}} = \boldsymbol{t}_{coh}(\boldsymbol{w}(\breve{\boldsymbol{u}})) \,, \quad \text{on } \tilde{\Gamma}_c \,, \tag{31a}$$

where $\breve{\boldsymbol{n}}(\tilde{\boldsymbol{x}}) := \boldsymbol{n}(\boldsymbol{M}_h(\tilde{\boldsymbol{x}}))$. Approximating $\breve{\boldsymbol{\sigma}}\breve{\boldsymbol{n}} \approx \boldsymbol{S}(\boldsymbol{\sigma})\breve{\boldsymbol{n}}$ and $\boldsymbol{w}(\breve{\boldsymbol{u}}) \approx \boldsymbol{w}(\boldsymbol{S}(\boldsymbol{u}))$, we obtain the shifting of the cohesive zone model:

$$\boldsymbol{S}(\boldsymbol{\sigma})\breve{\boldsymbol{n}} \approx\; \boldsymbol{t}_{coh}(\boldsymbol{w}(\boldsymbol{S}(\boldsymbol{u})) \,, \quad \text{on } \tilde{\Gamma}_c \,. \tag{31b}$$

In the next section we proceed to describe a viable variational discretization of the shifted cohesive zone model.

Remark 5. The proposed approach is based on the validity of the Taylor expansion, which is a reasonable assumption in the context of cohesive zone models. In fact, cohesive zone models are designed to prevent the stress to become unbounded as the grid is refined. Note also that the finite element approximation of gradient quantities typically occurs from below, that is the stresses computed on coarse grids are typically lower than the true gradients. The combination of these two aspects offers a sufficient level of robustness in practical engineering computations for the algorithm to be detailed in what follows.

Remark 6. In principle, the Taylor expansion is not the only tool that can be used to shift the fracture conditions from Γ_c to $\tilde{\Gamma}_c$. Hence, depending on which shift operator is used, the approach described above defines a *family* of computational methods. In this sense, the Shifted Fracture Method can be interpreted as a framework, more than a single computational method.

3.3 | Shifted variational equations

The first step in the derivation of variational equations is the definition of $\mathscr{S}^h_{\boldsymbol{u}}(\Omega \setminus \tilde{\Gamma}_c)$ and $\mathscr{S}^h_{\boldsymbol{\varepsilon}}(\Omega \setminus \tilde{\Gamma}_c)$, the discrete spaces of functions used to approximate the displacement $\boldsymbol{u}$ and the strain $\boldsymbol{\varepsilon}$:

$$\mathscr{S}^h_{\boldsymbol{u}}(\Omega \setminus \tilde{\Gamma}_c) = \{\boldsymbol{v} \in (C^0(\Omega \setminus \tilde{\Gamma}_c))^d \ : \ \boldsymbol{v}_{|\Gamma_D} = \boldsymbol{u}_D \ , \ \boldsymbol{v}\,|_T \in (\mathscr{P}^1(T))^d \ , \ \forall T \in \mathscr{T}_h\} \ , \tag{32a}$$

$$\mathscr{S}^h_{\boldsymbol{\varepsilon}}(\Omega \setminus \tilde{\Gamma}_c) = \{\boldsymbol{\omega} \in (C^0(\Omega \setminus \tilde{\Gamma}_c))^{d\times d} \ : \ \boldsymbol{\omega}\,|_T \in (\mathscr{P}^1(T))^{d\times d} \, , \boldsymbol{\omega} = \boldsymbol{\omega}^t, \ \forall T \in \mathscr{T}_h\} \ , \tag{32b}$$

where $\mathscr{P}^1(T)$ is the space of linear polynomial functions over the element T. Essentially, $\mathscr{S}^h_{\boldsymbol{u}}(\Omega \setminus \tilde{\Gamma}_c)$ and $\mathscr{S}^h_{\boldsymbol{\varepsilon}}(\Omega \setminus \tilde{\Gamma}_c)$ are spaces of vector and symmetric tensor functions that are piecewise-linear and continuous everywhere except across the interface $\tilde{\Gamma}_c$, and are compatible with boundary conditions on $\partial\Omega \setminus \Gamma_c$. Analogously, we can define the test function spaces

$$\mathscr{V}^h_{\boldsymbol{u}}(\Omega \setminus \tilde{\Gamma}_c) = \{\boldsymbol{v} \in (C^0(\Omega \setminus \tilde{\Gamma}_c))^d \ : \ \boldsymbol{v}_{|\Gamma_D} = \boldsymbol{0} \ , \ \boldsymbol{v}\,|_T \in (\mathscr{P}^1(T))^d \ , \ \forall T \in \mathscr{T}_h\} \ , \tag{32c}$$

$$\mathscr{V}^h_{\boldsymbol{\varepsilon}}(\Omega \setminus \tilde{\Gamma}_c) = \mathscr{S}^h_{\boldsymbol{\varepsilon}}(\Omega \setminus \tilde{\Gamma}_c) \ . \tag{32d}$$

Instead of (17a), let us test the strong equations against $\mathscr{V}^h_{\boldsymbol{u}}(\Omega \setminus \tilde{\Gamma}_c)$ and $\mathscr{V}^h_{\boldsymbol{\varepsilon}}(\Omega \setminus \tilde{\Gamma}_c)$, namely

$$-(\boldsymbol{\phi}, \nabla \cdot \boldsymbol{\sigma}(\boldsymbol{\varepsilon}))_{\Omega\setminus\tilde{\Gamma}_c} = (\boldsymbol{\phi}, \boldsymbol{b})_{\Omega\setminus\tilde{\Gamma}_c} \ , \tag{33a}$$

$$(\boldsymbol{\psi}, \boldsymbol{\varepsilon})_{\Omega\setminus\tilde{\Gamma}_c} = (\boldsymbol{\psi}, \nabla^s \boldsymbol{u})_{\Omega\setminus\tilde{\Gamma}_c} \ , \tag{33b}$$

where now the numerical solution may not be smooth across $\tilde{\Gamma}_c$. Integrating by parts (33a) and (33b) yields

$$(\nabla\boldsymbol{\phi}, \boldsymbol{\sigma}(\boldsymbol{\varepsilon}))_{\Omega\setminus\tilde{\Gamma}_c} + \langle [\![\boldsymbol{\phi}]\!], \{\!\{\boldsymbol{\sigma}(\boldsymbol{\varepsilon})\}\!\}_\lambda \tilde{\boldsymbol{n}}\rangle_{\tilde{\Gamma}_c} + \langle \{\!\{\boldsymbol{\phi}\}\!\}_{1-\lambda}, [\![\boldsymbol{\sigma}(\boldsymbol{\varepsilon})]\!]\tilde{\boldsymbol{n}}\rangle_{\tilde{\Gamma}_c} = (\boldsymbol{\phi}, \boldsymbol{b})_{\Omega\setminus\tilde{\Gamma}_c} + \langle \boldsymbol{\phi}, \boldsymbol{t}_N\rangle_{\Gamma_N} \ , \tag{34}$$

where the two faces of the crack $\tilde{\Gamma}_c$ are $\tilde{\Gamma}_c^+$, with outer normal $\tilde{\boldsymbol{n}}^+$, and $\tilde{\Gamma}_c^-$, with outer normal $\tilde{\boldsymbol{n}}^-$. We also define $\tilde{\boldsymbol{n}} = \tilde{\boldsymbol{n}}^+$.

We can now consider the terms $\{\!\{\boldsymbol{\sigma}(\boldsymbol{\varepsilon})\}\!\}_\lambda \tilde{\boldsymbol{n}}$ and $[\![\boldsymbol{\sigma}(\boldsymbol{\varepsilon})]\!]\tilde{\boldsymbol{n}}$ in (34), and express them in terms of shifted fracture interface conditions. Starting from the term $\{\!\{\boldsymbol{\sigma}(\boldsymbol{\varepsilon})\}\!\}_\lambda \tilde{\boldsymbol{n}}$, we have

$$\begin{aligned}\{\!\{\boldsymbol{\sigma}(\boldsymbol{\varepsilon})\}\!\}_\lambda \tilde{\boldsymbol{n}} &= \{\!\{\boldsymbol{\sigma}(\boldsymbol{\varepsilon})\}\!\}_\lambda ((\tilde{\boldsymbol{n}} \cdot \boldsymbol{n})\boldsymbol{n} + (\tilde{\boldsymbol{n}} \cdot \boldsymbol{\tau})\boldsymbol{\tau}) \\ &= (\tilde{\boldsymbol{n}}(\tilde{\boldsymbol{x}}) \cdot \check{\boldsymbol{n}}(\tilde{\boldsymbol{x}}))\, \{\!\{\boldsymbol{\sigma}(\boldsymbol{\varepsilon}(\tilde{\boldsymbol{x}}))\}\!\}_\lambda \check{\boldsymbol{n}}(\tilde{\boldsymbol{x}}) + (\tilde{\boldsymbol{n}}(\tilde{\boldsymbol{x}}) \cdot \check{\boldsymbol{\tau}}(\tilde{\boldsymbol{x}}))\, \{\!\{\boldsymbol{\sigma}(\boldsymbol{\varepsilon}(\tilde{\boldsymbol{x}}))\}\!\}_\lambda \check{\boldsymbol{\tau}}(\tilde{\boldsymbol{x}}) \ .\end{aligned} \tag{35}$$

Observing that $\{\!\{\boldsymbol{\sigma}(\boldsymbol{\varepsilon}(\tilde{\boldsymbol{x}}))\}\!\}_\lambda \check{\boldsymbol{n}}(\tilde{\boldsymbol{x}}) = \{\!\{\boldsymbol{\sigma}\,\check{\boldsymbol{n}}\}\!\}_\lambda = \{\!\{(\check{\boldsymbol{\sigma}} - \nabla\boldsymbol{\sigma}\,\boldsymbol{d})\,\check{\boldsymbol{n}}\}\!\}_\lambda = \{\!\{\check{\boldsymbol{t}} - (\nabla\boldsymbol{\sigma}\,\boldsymbol{d})\,\check{\boldsymbol{n}}\}\!\}_\lambda = \check{\boldsymbol{t}} - \{\!\{(\nabla\boldsymbol{\sigma}\,\boldsymbol{d})\}\!\}_\lambda \check{\boldsymbol{n}}$, since $\check{\boldsymbol{t}}(\tilde{\boldsymbol{x}})$ and $\check{\boldsymbol{n}}(\tilde{\boldsymbol{x}})$ are uniquely defined on $\tilde{\Gamma}_c$, and applying the Taylor expansion (27b), we obtain

$$\{\!\{\boldsymbol{\sigma}(\boldsymbol{\varepsilon})\}\!\}_\lambda \tilde{\boldsymbol{n}} = (\tilde{\boldsymbol{n}} \cdot \check{\boldsymbol{n}})\,(\check{\boldsymbol{t}} - \{\!\{(\nabla\boldsymbol{\sigma}(\boldsymbol{\varepsilon})\,\boldsymbol{d})\}\!\}_\lambda \check{\boldsymbol{n}}) + (\tilde{\boldsymbol{n}} \cdot \check{\boldsymbol{\tau}})\, \{\!\{\boldsymbol{\sigma}(\boldsymbol{\varepsilon})\}\!\}_\lambda \check{\boldsymbol{\tau}} \ , \quad \text{on } \tilde{\Gamma}_c \ . \tag{36}$$

Hence, using (24d), (24e), (31a) and (31b),

$$\begin{aligned}\langle [\![\boldsymbol{\phi}]\!], \{\!\{\boldsymbol{\sigma}(\boldsymbol{\varepsilon})\}\!\}_\lambda \tilde{\boldsymbol{n}}\rangle_{\tilde{\Gamma}_c} &= \langle [\![\boldsymbol{\phi}]\!], (\tilde{\boldsymbol{n}} \cdot \check{\boldsymbol{n}})\,(\check{\boldsymbol{t}} - \{\!\{(\nabla\boldsymbol{\sigma}(\boldsymbol{\varepsilon})\,\boldsymbol{d})\}\!\}_\lambda \check{\boldsymbol{n}}) + (\tilde{\boldsymbol{n}} \cdot \check{\boldsymbol{\tau}})\, \{\!\{\boldsymbol{\sigma}(\boldsymbol{\varepsilon})\}\!\}_\lambda \check{\boldsymbol{\tau}}\rangle_{\tilde{\Gamma}_c} \\ &= \langle [\![\boldsymbol{\phi}]\!], (\tilde{\boldsymbol{n}} \cdot \check{\boldsymbol{n}})\, \boldsymbol{t}_{coh}(\boldsymbol{w}(\boldsymbol{u} + \nabla\boldsymbol{u}\,\boldsymbol{d}))\rangle_{\tilde{\Gamma}_c} - \langle [\![\boldsymbol{\phi}]\!], (\tilde{\boldsymbol{n}} \cdot \check{\boldsymbol{n}})\,(\{\!\{(\nabla\boldsymbol{\sigma}(\boldsymbol{\varepsilon})\,\boldsymbol{d})\}\!\}_\lambda \check{\boldsymbol{n}}) - (\tilde{\boldsymbol{n}} \cdot \check{\boldsymbol{\tau}})\, \{\!\{\boldsymbol{\sigma}(\boldsymbol{\varepsilon})\}\!\}_\lambda \check{\boldsymbol{\tau}}\rangle_{\tilde{\Gamma}_c} \\ &= \langle [\![\boldsymbol{\phi}]\!], (\tilde{\boldsymbol{n}} \cdot \check{\boldsymbol{n}})\, \boldsymbol{t}_{coh}(\boldsymbol{w}(\boldsymbol{u} + \nabla\boldsymbol{u}\,\boldsymbol{d}))\rangle_{\tilde{\Gamma}_c} + \langle [\![\boldsymbol{\phi}]\!], \{\!\{\boldsymbol{\sigma}(\boldsymbol{\varepsilon})\}\!\}_\lambda \tilde{\boldsymbol{n}} - \{\!\{\boldsymbol{\sigma}(\boldsymbol{\varepsilon}) + \nabla\boldsymbol{\sigma}(\boldsymbol{\varepsilon})\boldsymbol{d}\}\!\}_\lambda (\tilde{\boldsymbol{n}} \cdot \check{\boldsymbol{n}})\check{\boldsymbol{n}}\rangle_{\tilde{\Gamma}_c} \ ,\end{aligned} \tag{37}$$

where we have used again the decomposition of the normal $\tilde{\boldsymbol{n}}$ in terms of its components along $\check{\boldsymbol{n}}$ and $\check{\boldsymbol{\tau}}$. Similarly, applying to the term $\langle \{\!\{\boldsymbol{\phi}\}\!\}_{1-\lambda}, [\![\boldsymbol{\sigma}(\boldsymbol{\varepsilon})]\!]\tilde{\boldsymbol{n}}\rangle_{\tilde{\Gamma}_c}$ the first of (18), that is $[\![\check{\boldsymbol{\sigma}}(\boldsymbol{\varepsilon})]\!]\,\check{\boldsymbol{n}} = \boldsymbol{0}$, yields

$$\begin{aligned}\langle \{\!\{\boldsymbol{\phi}\}\!\}_{1-\lambda}, [\![\boldsymbol{\sigma}(\boldsymbol{\varepsilon})]\!]\tilde{\boldsymbol{n}}\rangle_{\tilde{\Gamma}_c} &= \langle \{\!\{\boldsymbol{\phi}\}\!\}_{1-\lambda}\, , (\tilde{\boldsymbol{n}} \cdot \check{\boldsymbol{n}})\, [\![\check{\boldsymbol{\sigma}}(\boldsymbol{\varepsilon}) - \nabla\boldsymbol{\sigma}(\boldsymbol{\varepsilon})\boldsymbol{d}]\!]\,\check{\boldsymbol{n}} + (\tilde{\boldsymbol{n}} \cdot \check{\boldsymbol{\tau}})\, [\![\boldsymbol{\sigma}(\boldsymbol{\varepsilon})]\!]\,\check{\boldsymbol{\tau}}\rangle_{\tilde{\Gamma}_c} \\ &= \langle \{\!\{\boldsymbol{\phi}\}\!\}_{1-\lambda}\, , -(\tilde{\boldsymbol{n}} \cdot \check{\boldsymbol{n}})\, [\![\nabla\boldsymbol{\sigma}(\boldsymbol{\varepsilon})\boldsymbol{d}]\!]\,\check{\boldsymbol{n}} + (\tilde{\boldsymbol{n}} \cdot \check{\boldsymbol{\tau}})\, [\![\boldsymbol{\sigma}(\boldsymbol{\varepsilon})]\!]\,\check{\boldsymbol{\tau}}\rangle_{\tilde{\Gamma}_c}\end{aligned}$$

$$= \langle \{\!\{ \boldsymbol{\phi} \}\!\}_{1-\lambda} , [\![\boldsymbol{\sigma}(\boldsymbol{\varepsilon})]\!] \tilde{\boldsymbol{n}} - (\tilde{\boldsymbol{n}} \cdot \check{\boldsymbol{n}}) [\![\boldsymbol{\sigma}(\boldsymbol{\varepsilon}) + \nabla \boldsymbol{\sigma}(\boldsymbol{\varepsilon}) \boldsymbol{d}]\!] \check{\boldsymbol{n}} \rangle_{\tilde{\Gamma}_c} \ . \tag{38}$$

Substituting (37) and (38) into (34) and including the strain equation, we obtain

$$\begin{aligned} (\nabla \boldsymbol{\phi}, \boldsymbol{\sigma}(\boldsymbol{\varepsilon}))_{\Omega \setminus \tilde{\Gamma}_c} + (\boldsymbol{\psi}, \boldsymbol{\varepsilon} - \nabla^s \boldsymbol{u})_{\Omega \setminus \tilde{\Gamma}_c} + \langle [\![\boldsymbol{\phi}]\!], (\tilde{\boldsymbol{n}} \cdot \boldsymbol{n}) \boldsymbol{t}_{coh}(\boldsymbol{w}(\boldsymbol{u} + \nabla \boldsymbol{u}\, \boldsymbol{d})) \rangle_{\tilde{\Gamma}_c} + \langle [\![\boldsymbol{\phi}]\!], \{\!\{ \boldsymbol{\sigma}(\boldsymbol{\varepsilon}) \}\!\}_{\lambda} \tilde{\boldsymbol{n}} - \{\!\{ \boldsymbol{\sigma}(\boldsymbol{\varepsilon}) + \nabla \boldsymbol{\sigma}(\boldsymbol{\varepsilon}) \boldsymbol{d} \}\!\}_{\lambda} (\tilde{\boldsymbol{n}} \cdot \boldsymbol{n}) \boldsymbol{n} \rangle_{\tilde{\Gamma}_c} \\ + \langle \{\!\{ \boldsymbol{\phi} \}\!\}_{1-\lambda} , [\![\boldsymbol{\sigma}(\boldsymbol{\varepsilon})]\!] \tilde{\boldsymbol{n}} - (\tilde{\boldsymbol{n}} \cdot \boldsymbol{n}) [\![\boldsymbol{\sigma}(\boldsymbol{\varepsilon}) + \nabla \boldsymbol{\sigma}(\boldsymbol{\varepsilon}) \boldsymbol{d}]\!] \boldsymbol{n} \rangle_{\tilde{\Gamma}_c} - (\boldsymbol{\phi}, \boldsymbol{b})_{\Omega \setminus \tilde{\Gamma}_c} - \langle \boldsymbol{\phi}, \boldsymbol{t}_N \rangle_{\Gamma_N} = 0 , \end{aligned} \tag{39}$$

where we have omitted the symbol $\check{(\cdot)}$ over $\boldsymbol{n}$, for the sake of simplicity, and it is understood that all the fracture interface integrals are taken over $\tilde{\Gamma}_c$. In what follows, we will omit $\check{(\cdot)}$ over $\boldsymbol{n}$ whenever it does not cause confusion. We then obtain the final variational problem

Find $[\boldsymbol{u}, \boldsymbol{\varepsilon}] \in \mathscr{S}_{\boldsymbol{u}}^h(\Omega \setminus \tilde{\Gamma}_c) \times \mathscr{S}_{\boldsymbol{\varepsilon}}^h(\Omega \setminus \tilde{\Gamma}_c)$ *such that,* $\forall [\boldsymbol{\phi}, \boldsymbol{\psi}] \in \mathscr{V}_{\boldsymbol{u}}^h(\Omega \setminus \tilde{\Gamma}_c) \times \mathscr{V}_{\boldsymbol{\varepsilon}}^h(\Omega \setminus \tilde{\Gamma}_c)$,

$$\mathscr{B}_{\text{SFM}}^{[\Omega \setminus \tilde{\Gamma}_c]}([\boldsymbol{u}, \boldsymbol{\varepsilon}]; [\boldsymbol{\phi}, \boldsymbol{\psi}]) - \mathscr{L}_{\text{SFM}}^{[\Omega \setminus \tilde{\Gamma}_c]}([\boldsymbol{\phi}, \boldsymbol{\psi}]) = \langle \boldsymbol{\phi}, \boldsymbol{t}_N \rangle_{\Gamma_N} , \tag{40a}$$

where

$$\begin{aligned} \mathscr{B}_{\text{SFM}}^{[\Omega \setminus \tilde{\Gamma}_c]}([\boldsymbol{u}, \boldsymbol{\varepsilon}]; [\boldsymbol{\phi}, \boldsymbol{\psi}]) - \mathscr{L}_{\text{SFM}}^{[\Omega \setminus \tilde{\Gamma}_c]}([\boldsymbol{\phi}, \boldsymbol{\psi}]) - (\boldsymbol{\phi}, \boldsymbol{b})_{\Omega \setminus \tilde{\Gamma}_c} = \ & (\nabla \boldsymbol{\phi}, \boldsymbol{\sigma}(\boldsymbol{\varepsilon}))_{\Omega \setminus \tilde{\Gamma}_c} + (\boldsymbol{\psi}, \boldsymbol{\varepsilon} - \nabla^s \boldsymbol{u})_{\Omega \setminus \tilde{\Gamma}_c} \\ & + \langle [\![\boldsymbol{\phi}]\!], \boldsymbol{t}_{coh}(\boldsymbol{w}(\boldsymbol{S}(\boldsymbol{u}))) \rangle_{\tilde{\Gamma}_c} \\ & + \langle [\![\boldsymbol{\phi}]\!], \{\!\{ \boldsymbol{\sigma}(\boldsymbol{\varepsilon}) \}\!\}_{\lambda} \tilde{\boldsymbol{n}} - \{\!\{ \boldsymbol{S}(\boldsymbol{\sigma}(\boldsymbol{\varepsilon})) \}\!\}_{\lambda} (\tilde{\boldsymbol{n}} \cdot \boldsymbol{n}) \boldsymbol{n} \rangle_{\tilde{\Gamma}_c} \\ & + \langle \{\!\{ \boldsymbol{\phi} \}\!\}_{1-\lambda} , [\![\boldsymbol{\sigma}(\boldsymbol{\varepsilon})]\!] \tilde{\boldsymbol{n}} - (\tilde{\boldsymbol{n}} \cdot \boldsymbol{n}) [\![\boldsymbol{S}(\boldsymbol{\sigma}(\boldsymbol{\varepsilon}))]\!] \boldsymbol{n} \rangle_{\tilde{\Gamma}_c} . \end{aligned} \tag{40b}$$

Remark 7. The reason why we have left the term $\langle \boldsymbol{\phi}, \boldsymbol{t}_N \rangle_{\Gamma_N}$ out of the bilinear form will be apparent in Section 3.6, and we ask the reader to be patient in the meantime.

3.4 | Shifted Euler-Lagrangian equations

Integrating the first term of equation (39) by parts and accounting for potential discontinuities across the surrogate cohesive crack $\tilde{\Gamma}_c$, we have

$$\begin{aligned} (\boldsymbol{\phi}, -\nabla \cdot \boldsymbol{\sigma}(\boldsymbol{\varepsilon}) - \boldsymbol{b})_{\Omega \setminus \tilde{\Gamma}_c} - \langle \{\!\{ \boldsymbol{\phi} \}\!\}_{1-\lambda}, [\![\boldsymbol{\sigma}(\boldsymbol{\varepsilon})]\!] \tilde{\boldsymbol{n}} \rangle_{\tilde{\Gamma}_c} - \langle [\![\boldsymbol{\phi}]\!], \{\!\{ \boldsymbol{\sigma}(\boldsymbol{\varepsilon}) \}\!\}_{\lambda} \tilde{\boldsymbol{n}} \rangle_{\tilde{\Gamma}_c} + (\boldsymbol{\psi}, \boldsymbol{\varepsilon} - \nabla^s \boldsymbol{u})_{\Omega \setminus \tilde{\Gamma}_c} + \langle \boldsymbol{\phi}, \boldsymbol{\sigma}(\boldsymbol{\varepsilon}) \boldsymbol{n} - \boldsymbol{t}_N \rangle_{\Gamma_N} \\ + \langle [\![\boldsymbol{\phi}]\!], (\tilde{\boldsymbol{n}} \cdot \boldsymbol{n}) \boldsymbol{t}_{coh}(\boldsymbol{w}(\boldsymbol{u} + \nabla \boldsymbol{u}\, \boldsymbol{d})) \rangle_{\tilde{\Gamma}_c} + \langle [\![\boldsymbol{\phi}]\!], \{\!\{ \boldsymbol{\sigma}(\boldsymbol{\varepsilon}) \}\!\}_{\lambda} \tilde{\boldsymbol{n}} - \{\!\{ \boldsymbol{\sigma}(\boldsymbol{\varepsilon}) + \nabla \boldsymbol{\sigma}(\boldsymbol{\varepsilon}) \boldsymbol{d} \}\!\}_{\lambda} (\tilde{\boldsymbol{n}} \cdot \boldsymbol{n}) \boldsymbol{n} \rangle_{\tilde{\Gamma}_c} \\ + \langle \{\!\{ \boldsymbol{\phi} \}\!\}_{1-\lambda} , [\![\boldsymbol{\sigma}(\boldsymbol{\varepsilon})]\!] \tilde{\boldsymbol{n}} - (\tilde{\boldsymbol{n}} \cdot \boldsymbol{n}) [\![\boldsymbol{\sigma}(\boldsymbol{\varepsilon}) + \nabla \boldsymbol{\sigma}(\boldsymbol{\varepsilon}) \boldsymbol{d}]\!] \boldsymbol{n} \rangle_{\tilde{\Gamma}_c} = 0 , \end{aligned} \tag{41}$$

which, after simplifying some boundary terms, yields

$$\begin{aligned} (\boldsymbol{\phi}, -\nabla \cdot \boldsymbol{\sigma}(\boldsymbol{\varepsilon}) - \boldsymbol{b})_{\Omega \setminus \tilde{\Gamma}_c} + (\boldsymbol{\psi}, \boldsymbol{\varepsilon} - \nabla^s \boldsymbol{u})_{\Omega \setminus \tilde{\Gamma}_c} + \langle \boldsymbol{\phi}, \boldsymbol{\sigma}(\boldsymbol{\varepsilon}) \boldsymbol{n} - \boldsymbol{t}_N \rangle_{\Gamma_N} \\ - \langle [\![\boldsymbol{\phi}]\!], (\tilde{\boldsymbol{n}} \cdot \boldsymbol{n}) (\{\!\{ \boldsymbol{\sigma}(\boldsymbol{\varepsilon}) + \nabla \boldsymbol{\sigma}(\boldsymbol{\varepsilon}) \boldsymbol{d} \}\!\}_{\lambda} \boldsymbol{n} - \boldsymbol{t}_{coh}(\boldsymbol{w}(\boldsymbol{u} + \nabla \boldsymbol{u}\, \boldsymbol{d}))) \rangle_{\tilde{\Gamma}_c} - \langle \{\!\{ \boldsymbol{\phi} \}\!\}_{1-\lambda} , (\tilde{\boldsymbol{n}} \cdot \boldsymbol{n}) [\![\boldsymbol{\sigma}(\boldsymbol{\varepsilon}) + \nabla \boldsymbol{\sigma}(\boldsymbol{\varepsilon}) \boldsymbol{d}]\!] \boldsymbol{n} \rangle_{\tilde{\Gamma}_c} = 0 , \end{aligned} \tag{42}$$

and corresponds to

$$-\nabla \cdot \boldsymbol{\sigma} - \boldsymbol{b} = \boldsymbol{0} , \qquad \text{in } \Omega \setminus \tilde{\Gamma}_c , \tag{43a}$$

$$\boldsymbol{\varepsilon} - \nabla^s \boldsymbol{u} = \boldsymbol{0} , \qquad \text{in } \Omega \setminus \tilde{\Gamma}_c , \tag{43b}$$

$$\boldsymbol{\sigma} \boldsymbol{n} - \boldsymbol{t}_N = \boldsymbol{0} , \qquad \text{on } \Gamma_N , \tag{43c}$$

$$(\tilde{\boldsymbol{n}} \cdot \boldsymbol{n}) \left(\{\!\{ \boldsymbol{S}(\boldsymbol{\sigma}(\boldsymbol{\varepsilon})) \}\!\}_{\lambda} \boldsymbol{n} - \boldsymbol{t}_{coh}(\boldsymbol{w}(\boldsymbol{S}(\boldsymbol{u}))) \right) = \boldsymbol{0} , \qquad \text{on } \tilde{\Gamma}_c , \tag{43d}$$

$$(\tilde{\boldsymbol{n}} \cdot \boldsymbol{n}) [\![\boldsymbol{S}(\boldsymbol{\sigma}(\boldsymbol{\varepsilon}))]\!] \boldsymbol{n} = \boldsymbol{0} , \qquad \text{on } \tilde{\Gamma}_c , \tag{43e}$$

where the first three equalities are the enforcement of the balance of forces, the definition of the strain, and the traction boundary conditions, while the last two conditions are associated with the crack interface. In particular, (43d) enforces the cohesive law - approximated by the Taylor expansion and (43e) enforces the continuity of the normal component of the stress - again with the Taylor approximation - along all of $\tilde{\Gamma}_c$.

Remark 8. Role of $(\tilde{\boldsymbol{n}} \cdot \boldsymbol{n})$ *in* (43). The residuals (43d)–(43e) are multiplied by the weight $(\tilde{\boldsymbol{n}} \cdot \boldsymbol{n})$, which represents the projection of the curve/surface measure of the edges/faces in $\tilde{\Gamma}_c$ onto Γ_c, in the two/three-dimensional case, respectively. This area correction term is essential for the correct computation of the work associated with the crack cohesive forces, and to avoid severe

mesh dependencies in numerical computations. This is to say that the virtual work statement associated with (43d)–(43e) is automatically self-correcting for the effective true crack surface area. Instead, when node release techniques over the edges/faces of the grid are combined with cohesive zone models, the discrete crack area and associated virtual work statement are grossly inaccurate and induce severe mesh dependencies. We will return to this point when discussing, later on, the numerical results.

3.5 | A stabilized Shifted Fracture Method

If equal-order piecewise linear interpolation is used for both variables $\boldsymbol{u}$ and $\boldsymbol{\varepsilon}$, the overall finite element formulation is not numerically stable. It is however possible to stabilize the formulation (40a) by adding appropriate variational multiscale stabilization terms proposed in [92–94]. In these works, sub-grid components of the solution expressed by means of the residual of the discrete equations were used to enhance numerical stability. In the present work, the following modified form of the mixed system (40a) is used:

$$\mathscr{B}_{\text{SFM}}^{[\Omega\setminus\tilde{\Gamma}_c]}([\boldsymbol{u},\boldsymbol{\varepsilon}];[\boldsymbol{\phi},\boldsymbol{\psi}]) - \mathscr{L}_{\text{SFM}}^{[\Omega\setminus\tilde{\Gamma}_c]}([\boldsymbol{\phi},\boldsymbol{\psi}]) + (\nabla\cdot\boldsymbol{\sigma}(\boldsymbol{\psi}), \tau_{\boldsymbol{u}} h^2/2\mu(\nabla\cdot\boldsymbol{\sigma}(\boldsymbol{\varepsilon})+\boldsymbol{b}))_{\Omega\setminus\tilde{\Gamma}_c} \\ -(\boldsymbol{\psi}-\nabla^s\boldsymbol{\phi}, 2\mu\tau_{\boldsymbol{\varepsilon}}(\boldsymbol{\varepsilon}-\nabla^s\boldsymbol{u}))_{\Omega\setminus\tilde{\Gamma}_c} = \langle\boldsymbol{\phi},\boldsymbol{t}_N\rangle_{\Gamma_N}\,, \tag{44}$$

where the parameters $\tau_{\boldsymbol{\varepsilon}} = 0.5$ and $\tau_{\boldsymbol{u}} = 10$ are chosen for all computations shown in Section 5. The choice of $\tau_{\boldsymbol{\varepsilon}}$ and $\tau_{\boldsymbol{u}}$ was already explored in [92,93] for the Darcy flow operator, with an analysis of stability and convergence. The same choice of stabilization was made when adopting the Shifted Boundary Method for immersed solid mechanics computations [83], and was mathematically proved stable and accurate.

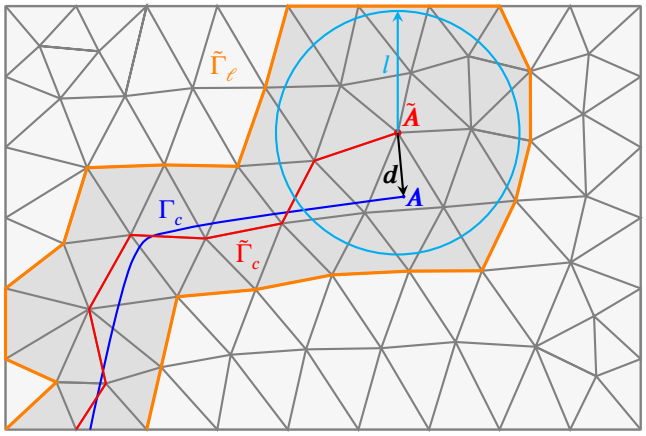

FIGURE 4 The true crack Γ_c (blue), the surrogate crack $\tilde{\Gamma}_c$ (red), and the boundary $\tilde{\Gamma}_L$ (orange) of the layer of elements.

3.6 | An efficient numerical implementation: the shifted fracture layer

The SFM described so far relies on a mixed displacements/strains formulation, which could be undesirable, due to the increase in degrees of freedom and thus the associated computational cost. At the same time, a primal formulation with piecewise-linear interpolation of $\boldsymbol{u}$ would lead to a first-order accurate method, because the cohesive traction conditions are akin to Robin conditions and the SFM would then require second-order derivatives of the displacement field. In fact, replacing $\boldsymbol{\varepsilon} = \nabla^s\boldsymbol{u}$ in the stress definition leads to $\nabla(\boldsymbol{\sigma}(\nabla^s\boldsymbol{u})) = \boldsymbol{0}$, in the case of piecewise linear interpolation.

This section introduces a strategy that significantly reduces the computational burden of solving the mixed system without reducing the accuracy of the displacement solution $\boldsymbol{u}$. This approach was proposed by Atallah *et al.* [83] and successfully tested for Dirichlet and Neumann conditions in linear elasticity.

Recalling the definitions of $\tilde{\Gamma}_c$ in Section 3.1, we define $\tilde{\Omega}_\ell$ as the set of elements $T \in \mathscr{T}_h$ with at least one node on $\tilde{\Gamma}_c \cup B(\tilde{\boldsymbol{A}}, l)$ (here $B(\tilde{\boldsymbol{A}}, l)$ is the ball of center $\tilde{\boldsymbol{A}}$ and radius l), that is,

$$\tilde{\Omega}_\ell = \{\cup_{T\in\mathscr{T}_h} T \,:\, T\cap(\tilde{\Gamma}_c \cup B(\tilde{\boldsymbol{A}}, l)) \neq \emptyset\}\,. \tag{45}$$

The set $\tilde{\Omega}_\ell$ can be described as the set of elements that are neighboring the surrogate crack surface, augmented by a cluster of elements around the tip of the surrogate crack, as shown in Figure 4. The radius l of the ball $B(\tilde{\boldsymbol{A}}, l)$ is chosen to scale like the mesh size h, and typically $l \in [2h, 3h]$. More details on the choice of l are included in Section 4.1.1. Observe that the boundary of $\tilde{\Omega}_\ell$ may include a portion of the boundaries Γ_D and Γ_N. Consider now the variational formulation:

Find $[\boldsymbol{u}, \boldsymbol{\varepsilon}] \in V_{\boldsymbol{u},h}(\Omega) \times V_{\boldsymbol{\varepsilon},h}(\tilde{\Omega}_\ell)$ *such that,* $\forall [\boldsymbol{\phi}, \boldsymbol{\psi}] \in V_{\boldsymbol{u},h}(\Omega) \times V_{\boldsymbol{\varepsilon},h}(\tilde{\Omega}_\ell)$,

$$\mathscr{B}_{\text{SFM}}([\boldsymbol{u}, \boldsymbol{\varepsilon}]; [\boldsymbol{\phi}, \boldsymbol{\psi}]) = \mathscr{L}_{\text{SFM}}([\boldsymbol{\phi}, \boldsymbol{\psi}]) \,, \tag{46a}$$

where

$$\mathscr{B}_{\text{SFM}}([\boldsymbol{u}, \boldsymbol{\varepsilon}]; [\boldsymbol{\phi}, \boldsymbol{\psi}]) = \; (\mathbf{C}\, \nabla^s \boldsymbol{u}, \nabla^s \boldsymbol{\phi})_{\Omega \setminus \tilde{\Omega}_\ell} + \mathscr{B}_{\text{SFM}}^{[\tilde{\Omega}_\ell \setminus \tilde{\Gamma}_c]}([\boldsymbol{u}, \boldsymbol{\varepsilon}]; [\boldsymbol{\phi}, \boldsymbol{\psi}]) \,, \tag{46b}$$

$$\mathscr{L}_{\text{SFM}}([\boldsymbol{\phi}, \boldsymbol{\psi}]) = \; (\boldsymbol{\phi}, \boldsymbol{b})_{\Omega \setminus \tilde{\Omega}_\ell} + \langle \boldsymbol{\phi}, \boldsymbol{t}_N \rangle_{\Gamma_N} + \mathscr{L}_{\text{SFM}}^{[\tilde{\Omega}_\ell \setminus \tilde{\Gamma}_c]}([\boldsymbol{\phi}, \boldsymbol{\psi}]) \;\; . \tag{46c}$$

This variational formulation is a combination of a standard primal formulation for the displacement unknown $\boldsymbol{u}$, and the mixed formulation (40) described in Section 3.3, but this time restricted to the domain $\tilde{\Omega}_\ell \setminus \tilde{\Gamma}_c$. Using integration by parts, it is possible to recover the following Euler-Lagrange equations. Here we focus on their restriction to $\Omega \setminus \tilde{\Omega}_\ell$ and its boundaries:

$$-\nabla \cdot \boldsymbol{\sigma}(\nabla^s \boldsymbol{u}) = \; \boldsymbol{b} \,, \qquad \text{in } \Omega \setminus \tilde{\Omega}_\ell \,, \tag{47a}$$

$$\boldsymbol{\sigma}(\nabla^s \boldsymbol{u}^+)\, \boldsymbol{n}^+ + \boldsymbol{\sigma}(\boldsymbol{\varepsilon})^- \boldsymbol{n}^- = \; \boldsymbol{0} \,, \qquad \text{on } \tilde{\Gamma}_\ell \,, \tag{47b}$$

$$(\mathbf{C}\, \nabla^s \boldsymbol{u})\, \boldsymbol{n} = \; \boldsymbol{t}_N \,, \qquad \text{on } \Gamma_N \cap \partial(\Omega \setminus \tilde{\Omega}_\ell) \,, \tag{47c}$$

where the "+" and "−" signs refer to the primal ($\Omega \setminus \tilde{\Omega}_\ell$) and mixed ($\tilde{\Omega}_\ell$) sides of the domain, respectively. Equation (47b) enforces continuity of the normal component of the stress across the interface $\tilde{\Gamma}_\ell$. Note that the discrete displacement $\boldsymbol{u}$ is by definition continuous over all of $\Omega \setminus \tilde{\Gamma}_c$.

Remark 9. The formulation (46) requires to solve the irreducible primal formulation over the major portion of the domain, $\Omega \setminus \tilde{\Omega}_\ell$, and to restrict the mixed variational formulation only on a small layer of elements $\tilde{\Omega}_\ell$ near the surrogate fracture $\tilde{\Gamma}_c$. In this context, the mixed formulation (40) described in Section 3.3 can be interpreted as a gradient reconstruction technique, built to ensure optimal error convergence for the SFM.

Remark 10. In the case in which multiple cracks are present with multiple (possibly overlapping) regions $\Omega \setminus \tilde{\Omega}^i_\ell$, the proposed efficient implementation would still be applicable and effective, since it would amount to use the mixed formulation on the union $\bigcup_i \left(\Omega \setminus \tilde{\Omega}^i_\ell\right)$, and the primal formulation elsewhere.

4 | IMPLEMENTATION OF THE SHIFTED FRACTURE METHOD

In this section, we discuss in detail the implementation of the SFM, which has computational complexity similar to a node release technique[2–4].

The propagation of the fracture is tracked by an iterative algorithm, which requires at every step the choice of a direction of propagation and an increment of crack length. The selection of the propagation direction is detailed in Section 4.1, the crack propagation algorithms and data structures are described in Section 4.2, and the crack length increments are chosen via the arc-length control strategy described in Section 4.3.

4.1 | Selection of the crack propagation direction

The SFM is not tied to any particular strategy for selecting the fracture propagation direction and we describe next two possibilities, which will be tested and compared in the numerical experiments: 1) the maximal principal tensile stress criterion, described in Section 4.1.1, and 2) the stress intensity factor (SIF) criterion, described in Section 4.1.2.

4.1.1 | Maximal principal stress criterion

The maximal principal stress criterion (e.g., see[49,95] and references therein) is based on the idea of propagating the crack tip along a plane orthogonal to the maximal principal stress. This approach has the advantage of simplicity, although it might not

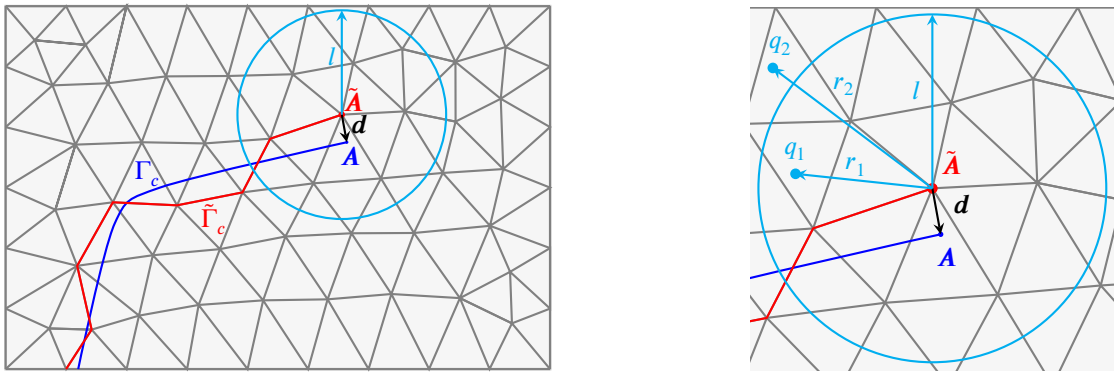

FIGURE 5 Estimation of the principal stresses at the tip of the true crack: The quadrature points used for the averaging of $\boldsymbol{\sigma}_{\tilde{\boldsymbol{A}}}$ and $\nabla\boldsymbol{\sigma}_{\tilde{\boldsymbol{A}}}$.

always be sufficiently accurate. This is especially the case for curved cracks propagating in geometries with corners[41,88], as confirmed by the numerical tests of Section 5.1.2. In the three-dimensional case, the implementation of the maximal principal stress criterion is, in general, simpler than the implementation of stress intensity factor criterion, and for this reason is preferred in the present work, although we stress it is not the only option for the SFM.

Because at the crack tip the stresses are typically less accurate, it is common practice to take a weighted average of the stresses in a neighborhood of the crack tip[95]. In the context of the SFM, this strategy needs to be appropriately shifted to the surrogate crack. The principal stresses are computed using an eigenvalue/eigenvector decomposition of the stress tensor $\boldsymbol{\sigma}(\boldsymbol{A})$ at the true crack tip $\boldsymbol{A}$, which is in turn estimated using a Taylor expansion centered at the surrogate tip $\tilde{\boldsymbol{A}}$, namely,

$$\boldsymbol{\sigma}(\boldsymbol{A}) = \langle\boldsymbol{\sigma}\rangle_{\tilde{\boldsymbol{A}}} + \langle\nabla\boldsymbol{\sigma}\rangle_{\tilde{\boldsymbol{A}}}\boldsymbol{d}\ . \tag{48}$$

Here, $\langle\boldsymbol{\sigma}\rangle_{\tilde{\boldsymbol{A}}}$ and $\langle\nabla\boldsymbol{\sigma}\rangle_{\tilde{\boldsymbol{A}}}$ are the weighted averages of the stress and stress gradient around the surrogate tip $\tilde{\boldsymbol{A}}$. For a scalar a, the operator $\langle\cdot\rangle_{\tilde{\boldsymbol{A}}}$ is defined as in[49], that is,

$$\langle a\rangle_{\tilde{\boldsymbol{A}}} = \frac{\int_{B(\tilde{\boldsymbol{A}},l)\cap\Omega} w\, a\ \mathrm{d}\Omega}{\int_{B(\tilde{\boldsymbol{A}},l)\cap\Omega} w\ \mathrm{d}\Omega}\ , \tag{49}$$

where $B(\tilde{\boldsymbol{A}},l)\cap\Omega$ is the ball of center $\tilde{\boldsymbol{A}}$ and radius l and

$$w = \frac{e^{-\frac{r^2}{2l^2}}}{(2\pi)^{3/2}l^3}\ , \tag{50}$$

with $r = r(\boldsymbol{y}) = |\boldsymbol{y} - \tilde{\boldsymbol{A}}|$ the Euclidean distance from the surrogate crack tip. Note that w is a Gaussian function centered at $\tilde{\boldsymbol{A}}$ and l determines how fast the weight function decays from the crack tip. Figure 5 shows the set $B(\tilde{\boldsymbol{A}},l)$ used in the definition of the weighted average operator. For example, in Figure 5, the quadrature point q_1 is used to compute (49), while q_2 is not, as it lies outside of the ball $B(\tilde{\boldsymbol{A}},l)$. In all numerical tests presented in Section 5, we take $l = 2.5h$.

Remark 11. Since a cohesive zone model is utilized in this work, the magnitude of the stress gradients becomes correlated with the cohesive length, which does not change as the grid is refined. Hence, as the grid resolution is increased, stress gradients are approximated with increasing accuracy. Overall, this approach proved robust and accurate in the representation of the crack curvature.

4.1.2 | Stress intensity factor (SIF) criterion

The stress intensity factor criterion is computationally more involved than the maximum principal stress criterion, but certainly offers many advantages. First and foremost, accuracy: since the SIFs are integral quantities, they converge with a much higher rate than the stress for a given discretization[41,88]. In addition, when shear effects are important in the development of cracks, the SIF approach is significantly superior.

Here we follow the approach proposed by Unger *et al.*[88], which avoids the computation of interaction integrals by linking the analytic representation of the near-tip displacement field for a traction-free crack surface to the stress intensity factors through

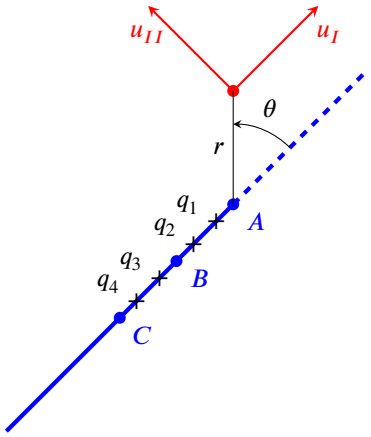

FIGURE 6 Displacement components around the crack tip in a polar coordinate system, and quadrature sampling points.

the formula

$$u_I(r,\theta) = K_I \frac{1}{2\mu}\sqrt{\frac{r}{2\pi}}\cos\left(\frac{\theta}{2}\right)\left[\kappa - 1 + 2\sin^2\left(\frac{\theta}{2}\right)\right] + K_{II}\frac{1}{2\mu}\sqrt{\frac{r}{2\pi}}\sin\left(\frac{\theta}{2}\right)\left[\kappa + 1 + 2\cos^2\left(\frac{\theta}{2}\right)\right], \tag{51a}$$

$$u_{II}(r,\theta) = K_I \frac{1}{2\mu}\sqrt{\frac{r}{2\pi}}\sin\left(\frac{\theta}{2}\right)\left[\kappa + 1 - 2\cos^2\left(\frac{\theta}{2}\right)\right] - K_{II}\frac{1}{2\mu}\sqrt{\frac{r}{2\pi}}\cos\left(\frac{\theta}{2}\right)\left[\kappa - 1 - 2\sin^2\left(\frac{\theta}{2}\right)\right], \tag{51b}$$

where r and θ are polar coordinates (see Fig. 6), $\kappa = \frac{3-\nu}{1+\nu}$ for plane stress, $\kappa = 3 - 4\nu$ for plane strain and $\mu = \frac{E}{2(1+\nu)}$. As shown in Figure 6, the polar coordinate system is aligned with the crack direction at the true tip A. Looking at Figure 6, consider now the first two fractured edges on the surrogate fracture $\tilde{\Gamma}_c$ and their projections BA and CB onto the (estimated) true fracture Γ_c. Consider also the quadrature points q_1, q_2, q_3 or q_4 associated to BA and CB, where the displacement components u_I and u_{II} satisfy equation (51b) with $\theta = \pi$ or $-\pi$ representing the opposite faces of the crack. Then, at each quadrature point, $\frac{K_I}{K_{II}} = \frac{u_{II}}{u_I}$, and a more reliable mean value can be obtained averaging over the four quadrature points (eight samples in total, since two crack faces lie at every quadrature point). The crack direction is associated with the maximum circumferential (hoop) tensile stress and can be computed using the formula

$$\tan\left(\frac{\alpha_c}{2}\right) = \frac{1}{4}\frac{K_I}{K_{II}} \pm \frac{1}{4}\sqrt{\left(\frac{K_I}{K_{II}}\right) + 8}\,, \tag{52}$$

where the sign is chosen so that the hoop stress $\sigma_n = \frac{1}{2}(\boldsymbol{\sigma}_{I,I} + \boldsymbol{\sigma}_{II,II}) + \frac{1}{2}(\boldsymbol{\sigma}_{I,I} - \boldsymbol{\sigma}_{II,II})\cos(2\alpha_c) + \boldsymbol{\tau}_{I,II}\sin(2\alpha_c)$ is maximal.

4.2 | Crack propagation algorithms and data structures

The typical SFM algorithms and data structures required to propagate the fracture in two and three dimensions are not much different from the data structures required in a node-release technique[3]. A detailed presentation is outlined next. We start with the two-dimensional case, since it is more intuitive, and then explain how the key procedures and data structures need to be modified in the three-dimensional case.

4.2.1 | Two-dimensional case

In the two-dimensional case, once a direction of propagation for the (true) fracture has been found (with the methods described in Section 4.1), the idea is to propagate the surrogate fracture $\tilde{\Gamma}_c$ and to track the location of the estimated true crack tip using the distance vector $\boldsymbol{d}$, as shown in Figure 7. This leads to a pseudo-loading step, in which the topology of the fracture is updated.

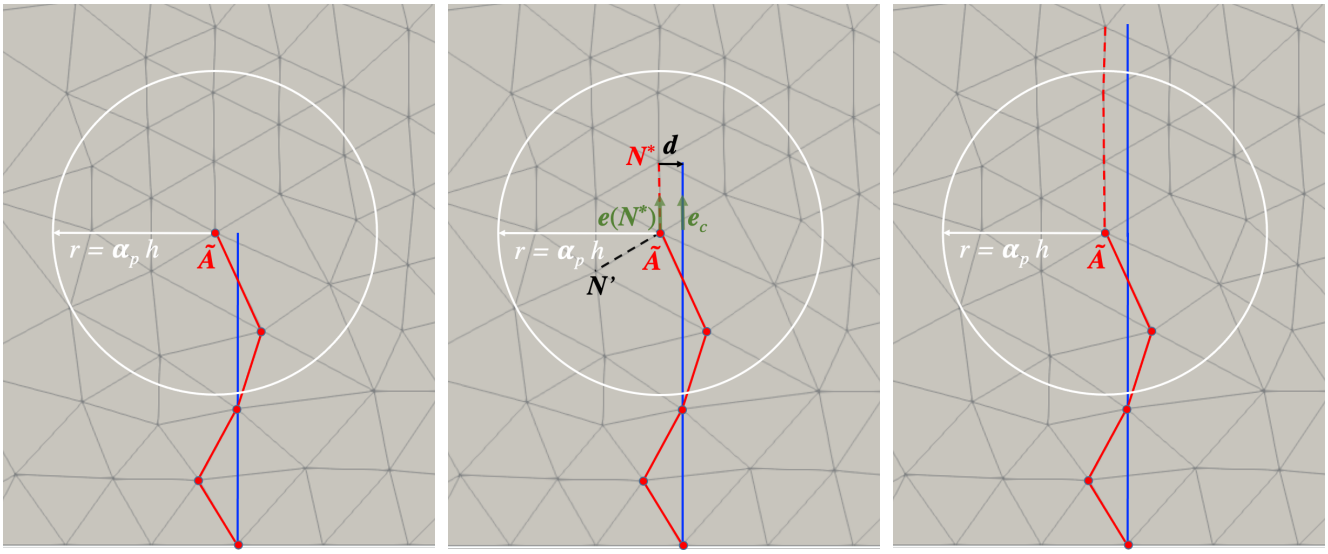

FIGURE 7 SFM strategy for the propagation of a two-dimensional fracture.

Algorithm 1 Topological update of the fracture in two dimensions.

initialization ($n = 0$)**:** set the initial surrogate crack tip $\tilde{\boldsymbol{A}}_0$ (as the closest boundary node to the true tip $\boldsymbol{A}_0$)
loop over n (fracture topology step)
  Compute the weighted stress at the true tip $\boldsymbol{\sigma}(\boldsymbol{A}_n) = \langle \boldsymbol{\sigma} \rangle_{\tilde{\boldsymbol{A}}_n} + \langle \nabla \boldsymbol{\sigma} \rangle_{\tilde{\boldsymbol{A}}_n} \boldsymbol{d}$ using (48), (49) and (50)
  Compute the maximum tensile principal stress σ_p associated with $\boldsymbol{\sigma}(\boldsymbol{A}_n)$
  if $\sigma_p > t_{cr}$
    Define the ball $B(\tilde{\boldsymbol{A}}_n, r) = \{\boldsymbol{x} \in \mathbb{R}^2 : \|\boldsymbol{x} - \tilde{\boldsymbol{A}}_n\| < r\}$ with radius $r = \alpha_p h$
    Compute the fracture propagation direction at $\boldsymbol{A}_n$ (unit vector $\boldsymbol{e}_c$) using either:
      • the maximum tensile principal stress criterion (Section 4.1.1), or
      • the SIF criterion (Section 4.1.2)
    initialization: iterate $(i) = 0$ and $\tilde{\boldsymbol{A}}_{n+1}^{(0)} = \tilde{\boldsymbol{A}}_n$
    while $\tilde{\boldsymbol{A}}_{n+1}^{(i)} \in B(\tilde{\boldsymbol{A}}_n, r)$ **loop** over the iterate (i)
      Define $\mathcal{N}(\tilde{\boldsymbol{A}}_{n+1}^{(i)})$ as the set of nodes that are connected to $\tilde{\boldsymbol{A}}_{n+1}^{(i)}$ by an edge
      loop over every node $\bar{\boldsymbol{N}}^* \in \mathcal{N}(\tilde{\boldsymbol{A}}_{n+1}^{(i)})$
        Set $\boldsymbol{e}(\bar{\boldsymbol{N}}^*)$ as the oriented edge connecting $\tilde{\boldsymbol{A}}_{n+1}^{(i)}$ and $\bar{\boldsymbol{N}}^* \in \mathcal{N}(\tilde{\boldsymbol{A}}_{n+1}^{(i)})$, that is $\boldsymbol{e}(\bar{\boldsymbol{N}}^*) = \tilde{\boldsymbol{A}}_{n+1}^{(i)} \bar{\boldsymbol{N}}^*$
        if $\boldsymbol{e}_c \cdot \boldsymbol{e}(\bar{\boldsymbol{N}}^*) > 0$
          Compute the distance $\boldsymbol{d}(\bar{\boldsymbol{N}}^*)$ from $\bar{\boldsymbol{N}}^*$ to the half-line emanating from $\boldsymbol{A}_n$ in the direction $\boldsymbol{e}_c$ (see Fig. 7b)
          Add $\bar{\boldsymbol{N}}^*$ to the set $\mathcal{N}^+(\tilde{\boldsymbol{A}}_{n+1}^{(i)}) = \{\boldsymbol{M}^* \in \mathcal{N}(\tilde{\boldsymbol{A}}_{n+1}^{(i)}) : \boldsymbol{e}_c \cdot \boldsymbol{e}(\boldsymbol{M}^*) > 0\}$
        end if
      end loop over $\mathcal{N}(\tilde{\boldsymbol{A}}_{n+1}^{(i)})$
      Select $\boldsymbol{N}^* = \arg\min_{\bar{\boldsymbol{N}}^* \in \mathcal{N}^+(\tilde{\boldsymbol{A}}_{n+1}^{(i)})} \boldsymbol{d}(\bar{\boldsymbol{N}}^*)$
      Add the edge $\boldsymbol{e}(\boldsymbol{N}^*)$ to the surrogate fracture $\tilde{\Gamma}_c$
      Update $\tilde{\boldsymbol{A}}_{n+1}^{(i+1)} = \boldsymbol{N}^*$
    end while loop over iterate (i)
  end if
  Apply arc-length Algorithm 3 to solve the nonlinear system of equations
end loop over n

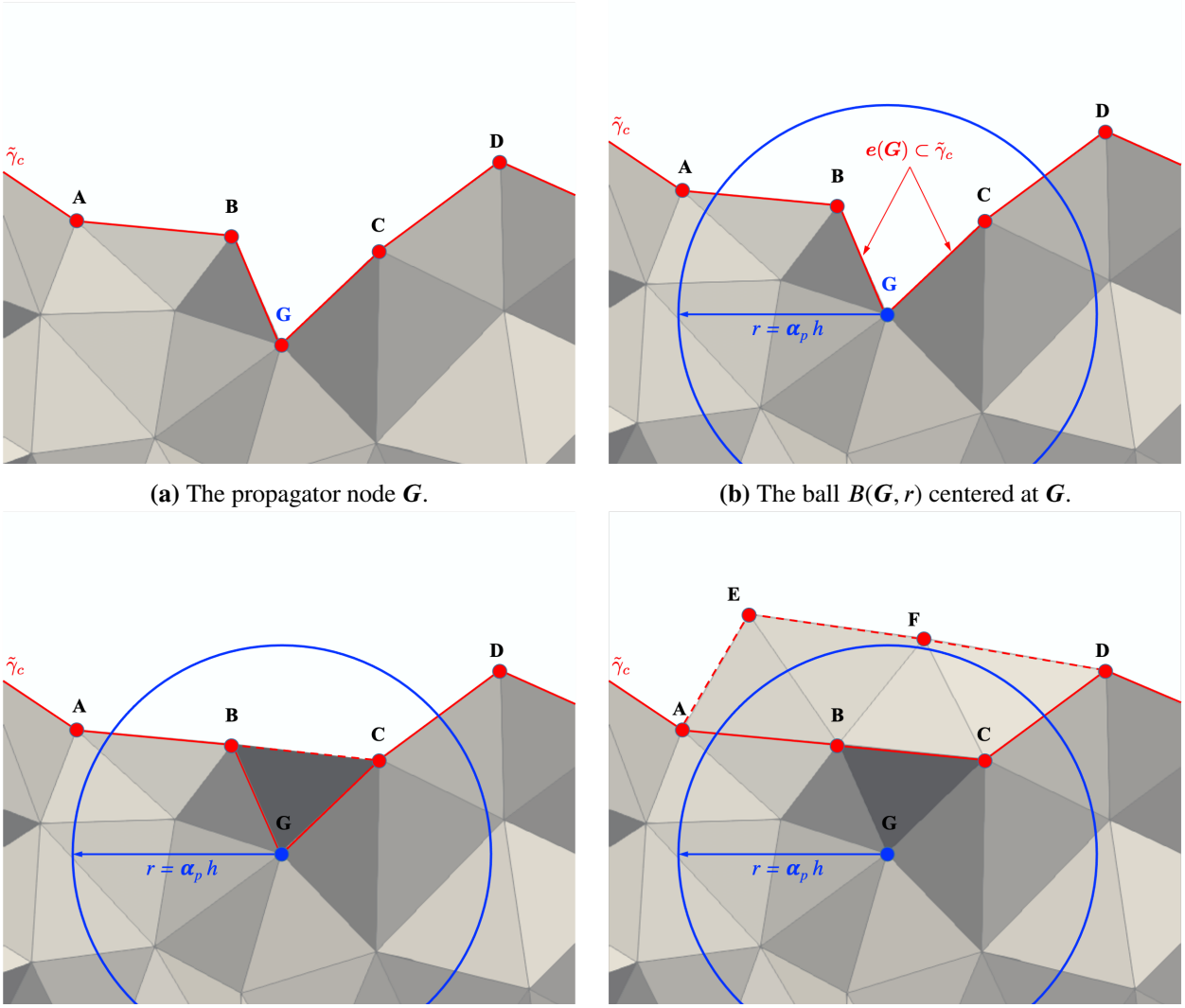

(a) The propagator node $\boldsymbol{G}$.

(b) The ball $B(\boldsymbol{G}, r)$ centered at $\boldsymbol{G}$.

(c) The face $\boldsymbol{GBC}$ is added to $\tilde{\Gamma}_c$ to prevent holes.

(d) Propagation continues inside $B(\boldsymbol{G}, r)$.

FIGURE 8 The three-dimensional propagation of the crack surface from a propagator node $\boldsymbol{G}$.

Due to the very general topology that the computational grid can assume, and similar to XFEMs/GFEMs[48] and node-release techniques[3], it is not always feasible for the SFM algorithm to precisely enforce that only one new surrogate edge is released at every incremental update of the fracture topology.

Our approach, similar to XFEMs/GFEMs, is to allow multiple edges of $\tilde{\Gamma}_c$ to release, as long as they are contained in or intersect the ball (or disk) $B(\tilde{\boldsymbol{A}}, r)$, centered at the surrogate tip $\tilde{\boldsymbol{A}}$ and of radius r, shown in Figure 7a. Specifically, we take $r = \alpha_p h$ with $\alpha_p = 2.5$, that is, we allow about three surrogate edges at a time to release, as shown in Figure 7c. In some sense, the parameter α_p relates to the arc-length parameter Δl discussed in Section 4.3, to which the reader is referred for a thorough discussion.

An additional requirement is that the surrogate fracture must propagate forward, that is, as shown in Figure 7b, that the inner product of the unit vector $\boldsymbol{e}_c$ (aligned in the fracture propagation direction) and the unit vector $\boldsymbol{e}(\boldsymbol{N}^*)$ (aligned from the current surrogate tip $\tilde{\boldsymbol{A}}$ to the candidate new tip location $\boldsymbol{N}^*$) be positive and of minimal in magnitude. For example, looking again at Figure 7b, the edge $\tilde{\boldsymbol{A}}\boldsymbol{N}^*$ (associated with the nodes $\tilde{\boldsymbol{A}}$ and $\boldsymbol{N}^*$) is allowed as a candidate to propagate the fracture, while edge $\tilde{\boldsymbol{A}}\boldsymbol{N}'$ is disallowed. The edge $\tilde{\boldsymbol{A}}\boldsymbol{N}^*$ is eventually chosen since the inner product $\boldsymbol{e}_c \cdot \boldsymbol{e}(\boldsymbol{N}^*)$ is minimal among all the edges connected to the surrogate tip $\tilde{\boldsymbol{A}}$. The specific details of the two-dimensional fracture propagation algorithm are presented in Algorithm 1.

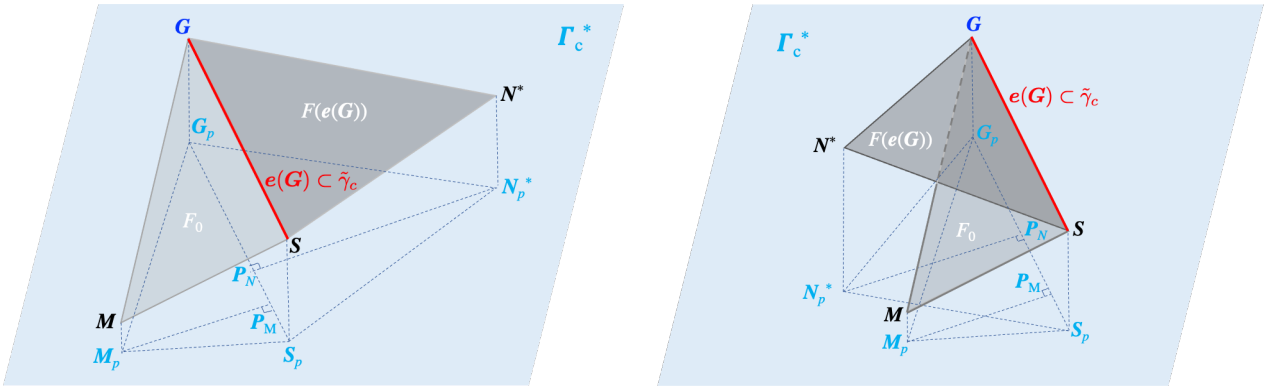

FIGURE 9 Strategy for forward-propagation of the three-dimensional surrogate crack surface. Given the edge $\boldsymbol{e}(\boldsymbol{G})$ connecting the nodes $\boldsymbol{G}$ and $\boldsymbol{S}$ on the crack front $\tilde{\gamma}_c$, consider the two faces attached to it, namely F_0 (with nodes $\boldsymbol{G}$, $\boldsymbol{S}$, and $\boldsymbol{M}$) and $F(\boldsymbol{e}(\boldsymbol{G}))$ (with nodes $\boldsymbol{G}$, $\boldsymbol{S}$, and $\boldsymbol{N}^*$). Let Γ_c^* be a candidate plane of propagation of the true crack and $\boldsymbol{G}_p$, $\boldsymbol{S}_p$, $\boldsymbol{M}_p$ and $\boldsymbol{N}_p^*$ the projections on Γ_c^* of $\boldsymbol{G}$, $\boldsymbol{S}$, $\boldsymbol{M}$ and $\boldsymbol{N}^*$, respectively. Let then $\boldsymbol{P}_M$ and $\boldsymbol{P}_N$ be the projections of $\boldsymbol{M}$ and $\boldsymbol{N}^*$ on the segment connecting $\boldsymbol{G}_p$ and $\boldsymbol{S}_p$. Only faces for which the inner product of $\boldsymbol{P}_M\boldsymbol{M}_p \cdot \boldsymbol{P}_N\boldsymbol{N}_p^* < 0$ are accepted as possible candidates on the updated surrogate fracture $\tilde{\Gamma}_c$. That is to say that the face $F(\boldsymbol{e}(\boldsymbol{G}))$ is accepted for a configuration as in Figure 9a and discarded for one as in Figure 9b. Because of the basic space-filling features of three-dimensional grids, the forward propagation constraint will always be satisfied by at least one candidate face. See for more details Algorithm 2.

Remark 12. The idea of "forward" propagation of the crack is purely spatial, in the sense that we select the edges of the surrogate fracture surface to be the best approximate representation of the true fracture surface. In a number of preliminary tests not reported here for the sake of brevity, the SFM proved to work also in the case of back-and-forth zig-zagging surrogate crack patterns, thanks to the area correction associated with the term $\boldsymbol{n} \cdot \tilde{\boldsymbol{n}}$. We prefer however to avoid this scenario, and for this reason the condition of forward spatial crack propagation has been added. Note also that non-monotonic loading is possible for the current cohesive zone model, which can be also be modified to incorporate contact in the case of full crack closure.

4.2.2 | Three-dimensional case

The algorithm and data structures for the propagation of the three-dimensional fracture is more complex than in the two-dimensional case, but still of similar complexity with respect to a three-dimensional node-release technique[3]. In the three-dimensional case, the fracture is a front (a continuous, possibly non-smooth curve, in $\mathbb{R}^3$) and enforcing continuity of the surrogate (and true) fracture surface is more challenging. However, the geometric framework of the SFM, which is based on the distance vector function $\boldsymbol{d}$, offers many advantages over a XFEM/GFEM approach in this regard, because it is considerably easier to manipulate distances than cuts/intersections, for the purpose of tracking the evolution of the fracture and enforcing continuity of the crack surface. For the SFM, in fact, the continuity property of the fracture surface is equivalent to the requirement that the distance vector function $\boldsymbol{d}$ between $\tilde{\Gamma}_c$ and Γ_c is single valued.

The key idea in developing three-dimensional SFM data structures is to define a *surrogate fracture front* $\tilde{\gamma}_c \subset \tilde{\Gamma}_c$ (see Fig. 8a) and a propagation strategy for it. A node $\boldsymbol{G} \subset \tilde{\gamma}_c$ for which the maximum principal tensile stress is above t_{cr} (node release condition) becomes a member of the set $\mathcal{G}_{\tilde{\gamma}_c}$ of *fracture propagators*. Let $B(\boldsymbol{G}, r)$ be the ball of radius $r = \alpha_p h$ (with $\alpha_p \sim 3$) centered at $\boldsymbol{G} \in \mathcal{G}_{\tilde{\gamma}_c}$, and $\pi(\boldsymbol{G})$ the plane orthogonal to the eigenvector $\boldsymbol{e}_p(\boldsymbol{G})$ associated with the maximal tensile principal stress at $\boldsymbol{G}$. The union of these balls, $\{\cup_{\boldsymbol{G}} B(\boldsymbol{G}, r) \,:\, \boldsymbol{G} \in \mathcal{G}_{\tilde{\gamma}_c}\}$, defines an envelope region where the crack is allowed to propagate. Inside each ball $B(\boldsymbol{G}, r)$, propagation will occur in a direction approximately aligned with the plane $\pi(\boldsymbol{G})$, as shown next.

The algorithm loops over the propagators in the set $\mathcal{G}_{\tilde{\gamma}_c}$. Let $\boldsymbol{G} \in \mathcal{G}_{\tilde{\gamma}_c}$ be the first of such propagators in the loop, and consider an oriented edge $\boldsymbol{e}(\boldsymbol{G}) \subset \tilde{\gamma}_c$ attached to $\boldsymbol{G}$. In particular, there will be two such edges if $\boldsymbol{G}$ is an internal node, or one such edge if $\boldsymbol{G}$ is on the exterior boundary. We note that it is sufficient to pick one edge of this type, which always exists. Then, $\tilde{\Gamma}_c$ is updated by adding to it a (triangular) face $F(\boldsymbol{e}(\boldsymbol{G}))$ of the grid that has two nodes on the edge $\boldsymbol{e}(\boldsymbol{G})$ and an additional node $\boldsymbol{N}^*$ outside $\boldsymbol{e}(\boldsymbol{G})$ (see Fig. 8b).

Algorithm 2 Topological update of the fracture in three dimensions

1: **initialization** ($n = 0$)**:** set the initial surrogate crack front $\tilde{\gamma}_{c;0}$ (as the closest-point projection to the initial crack front $\gamma_{c;0}$)
2: **loop** over n (fracture topology step)
3: Set $\mathscr{N}(\tilde{\gamma}_c)$ as the set of nodes on the crack front $\tilde{\gamma}_c$ (e.g., $\boldsymbol{A} \in \mathscr{N}(\tilde{\gamma}_c)$ in Fig. 8a)
4: Initialize the set of *fracture propagators* $\mathscr{G}_{\tilde{\gamma}_c} = \emptyset$
5: **loop** over the nodes $\boldsymbol{N}_i \in \mathscr{N}(\tilde{\gamma}_c)$
6: Compute the weighted average stress at the true tip $\boldsymbol{\sigma}(\boldsymbol{N}_i) = \langle \boldsymbol{\sigma} \rangle_{\boldsymbol{N}_i} + \langle \nabla \boldsymbol{\sigma} \rangle_{\boldsymbol{N}_i} \boldsymbol{d}$ using (48), (49) and (50)
7: Compute the maximum tensile principal stress $\boldsymbol{\sigma}_p$ associated with $\boldsymbol{\sigma}(\boldsymbol{N}_i)$ and associated unit eigenvector $\boldsymbol{e}_p(\boldsymbol{N}_i)$
8: **if** $\boldsymbol{\sigma}_p > t_{cr}$
9: Add $\boldsymbol{N}_i$ to the set of *fracture propagators* $\mathscr{G}_{\tilde{\gamma}_c}$
10: Define the ball $B(\boldsymbol{N}_i, r) = \{\boldsymbol{x} \in \mathbb{R}^3 \,:\, \|\boldsymbol{x} - \boldsymbol{N}_i\| < r\}$ with radius $r = \alpha_p h$ (see Fig. 8b where $\boldsymbol{N}_i = \boldsymbol{G}$)
11: Compute the candidate fracture propagation plane $\pi(\boldsymbol{N}_i)$ through $\boldsymbol{N}_i$ and orthogonal to $\boldsymbol{e}_p(\boldsymbol{N}_i)$
12: **end if**
13: **end loop** over $\mathscr{N}(\tilde{\gamma}_c)$
14: **loop** over the propagators $\boldsymbol{G}_j \in \mathscr{G}_{\tilde{\gamma}_c}$
15: **initialization:** iterate $(k) = 0$, $\tilde{\gamma}^{(0)} = \tilde{\gamma}_c$ and $\mathscr{N}^{(0)} = \{\boldsymbol{G}_j\}$
16: **while** $\mathscr{N}^{(k)} \neq \emptyset$ **loop** over the iterate k
17: Pick a node $\boldsymbol{N} \in \mathscr{N}^{(k)}$ and find an edge $\boldsymbol{e}(\boldsymbol{N}) \subset \tilde{\gamma}^{(k)}$ attached to it
18: Set `boolean fillGap = false`
19: Set $\mathscr{F}(\boldsymbol{e}(\boldsymbol{N}))$ as the set of triangular faces attached to $\boldsymbol{e}(\boldsymbol{N})$
20: Set $\mathscr{F}^+ = \emptyset$ (set of forward propagating faces)
21: **loop** over $F \in \mathscr{F}(\boldsymbol{e}(\boldsymbol{N}))$
22: Set $\bar{\boldsymbol{N}}^*$ as the vertex (node) of F opposite to $\boldsymbol{e}(\boldsymbol{N})$
23: **if** $\bar{\boldsymbol{N}}^* \in \tilde{\gamma}_c^k$
24: Set `boolean fillGap = true`.
25: Add F to the surrogate fracture surface $\tilde{\Gamma}_c$ (see Fig. 8c)
26: Update $\tilde{\gamma}_c^{(k+1)}$
27: **exit loop** over $F \in \mathscr{F}(\boldsymbol{e}(\boldsymbol{N}))$ and continue from line 40
28: **else**
29: **if** F satisfies the forward fracture propagation condition (see Fig. 9) **then**
30: Add F to $\mathscr{F}^+$
31: Compute the average distance $\langle \boldsymbol{d}(\bar{\boldsymbol{N}}^*) \rangle$ to the planes $\pi(\boldsymbol{G}')$ with $\boldsymbol{G}' \in \mathscr{G}(\boldsymbol{N}^*)$
32: **end if**
33: **end if**
34: **end loop** over $F \in \mathscr{F}(\boldsymbol{e}(\boldsymbol{N}))$
35: **if** `fillGap = false`
36: Add $F^* = \arg\min_{\mathscr{F}^+} \langle \boldsymbol{d}(\bar{\boldsymbol{N}}^*) \rangle$ to the surrogate fracture $\tilde{\Gamma}_c$ (see Fig. 8d)
37: Add $\boldsymbol{N}^*$ to $\mathscr{N}^{(k+1)}$ ($\boldsymbol{N}^*$ is the vertex of F^* opposite to $\boldsymbol{e}(\boldsymbol{N})$)
38: Update $\tilde{\gamma}_c^{(k+1)}$: remove $\boldsymbol{e}(\boldsymbol{N})$ and add the two opposite edges of F^*
39: **end if**
40: Update $\mathscr{N}^{(k+1)}$: remove nodes that do not belong to $\tilde{\gamma}_c^{(k+1)}$
41: **end while loop** over iterate (k)
42: Update $\tilde{\gamma}_c = \tilde{\gamma}_c^{(k+1)}$, and similarly for $\mathscr{N}(\tilde{\gamma}_c)$
43: **end loop** over the propagators $\boldsymbol{G}_j \in \mathscr{G}_{\tilde{\gamma}_c}$
44: Apply arc-length Algorithm 3 to solve the nonlinear system of equations
45: **end loop** over n

The procedure to select $F(\boldsymbol{e}(\boldsymbol{G}))$ (i.e. $\boldsymbol{N}^*$) is as follows: first, if $\boldsymbol{N}^*$ already belongs to $\tilde{\gamma}_c$, the face $F(\boldsymbol{e}(\boldsymbol{G}))$ is added to $\tilde{\Gamma}_c$, to avoid the formation of spurious holes in $\tilde{\Gamma}_c$ (see Fig. 8b); otherwise, for every candidate face $F(\boldsymbol{e}(\boldsymbol{G}))$, the set $\mathcal{G}(\boldsymbol{N}^*) = \{\boldsymbol{G}' \in \mathcal{G}_{\tilde{\gamma}_c} \,:\, \boldsymbol{N}^* \in B(\boldsymbol{G}', r)\}$ is defined as the set of propagators $\boldsymbol{G}'$ that have $\boldsymbol{N}^*$ contained inside $B(\boldsymbol{G}', r)$; the average distance $\langle \boldsymbol{d}(\boldsymbol{N}^*)\rangle$ of $\boldsymbol{N}^*$ from the planes $\pi(\boldsymbol{G}')$ with $\boldsymbol{G}' \in \mathcal{G}(\boldsymbol{N}^*)$ is computed; finally, the face $F(\boldsymbol{e}(\boldsymbol{G}))$ is chosen so that $\langle \boldsymbol{d}(\boldsymbol{N}^*)\rangle$ is minimal, and $\langle \boldsymbol{d}(\boldsymbol{N}^*)\rangle$ is stored for the corresponding node $\boldsymbol{N}^*$. Once a face is added to $\tilde{\Gamma}_c$, the set $\tilde{\gamma}_c$ is updated, and propagation of the crack continues from the new edges added to $\tilde{\gamma}_c$. Eventually, the fracture propagation is completed inside the ball $B(\boldsymbol{G}, r)$ associated with the propagator $\boldsymbol{G}$, and can continue inside the balls $B(\boldsymbol{G}', r)$ associated to the additional propagators $\boldsymbol{G}' \in \mathcal{G}_{\tilde{\gamma}_c}$, until it extends to the entire envelope $\{\cup_{\boldsymbol{G}} B(\boldsymbol{G}, r) \,:\, \boldsymbol{G} \in \mathcal{G}_{\tilde{\gamma}_c}\}$.

Note that, also in the three-dimensional case, the constraint of forward-propagation of the surrogate fracture is enforced, following the approach described in Figure 9. Because of the basic space-filling features of three-dimensional grids, the forward propagation constraint will always be satisfied by at least one candidate face.

Remark 13. In principle, the shape of the surrogate fracture surface may depend on the order with which the loop over the propagators is performed, but in practice if sufficient mesh resolution is available, this is not the case.

Remark 14. The proposed strategy yields a continuous surrogate fracture surface without spurious holes.

The operations described above involve local grid operations, and parallel implementation comes with relative ease, if the set $\tilde{\gamma}_c$ is available to all processors.

Of course, the proposed approach to propagate topologically the fracture is not the only choice, and alternative, more efficient strategies can be considered. The key point here is that the propagation of the fracture, as in the two-dimensional case, occurs on the surrogate fracture interface $\tilde{\Gamma}_c$, and that, through the distance d, an estimate of the location of the true fracture surface Γ_c is found.

4.3 | A Newton-Raphson method with crack-opening arc-length control

The propagation of fractures in solids may induce global softening responses and snap-back patterns, as sketched in Figure 10a. It is well-known that the Newton-Raphson method with displacement control cannot appropriately capture the unloading branch of the force/displacement curve in a snap-back problem (the dashed line seen in Fig. 10b). Analogous issues are encountered with a force control strategy, which only captures the response up to the peak load.

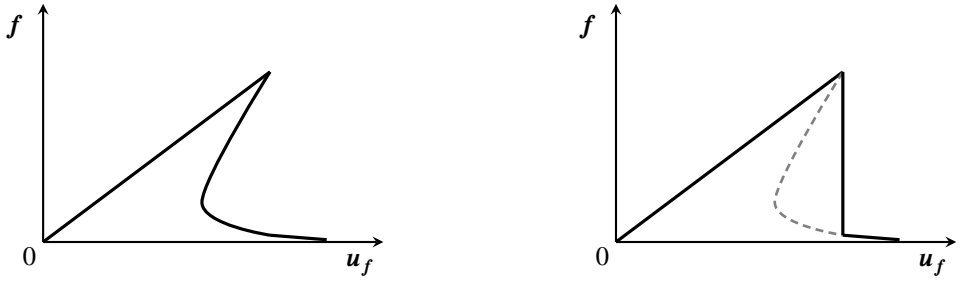

(a) An example of snap-back. **(b)** Displacement control for a snap-back problem.

FIGURE 10 Snap-back example and limitation of the displacement control strategy for a Newton-Raphson method.

Arc-length methods[96–98] offer considerable advantages for this class of problems, in terms of robustness and accuracy. In the version of the arc-length method we propose, the control variable is tuned to scale with the crack opening $w_{eq}(\boldsymbol{u})$. We start with a classical estimate[1,48] of the cohesive zone length l_{coh}, namely:

$$l_{coh} = \frac{G_F E}{(1-\nu^2) t_{cr}^2} \,, \tag{53}$$

where G_F is the fracture energy defined in (14). Observe that l_{coh} does not change through the fracture process. For a characteristic mesh size h, the total number of elements in the cohesive zone is given by

$$N_{coh} = l_{coh}/h \, . \tag{54}$$

The evolution of the fracture occurs in a number of (loading) steps. Each loading step extends the surrogate fracture by an amount roughly corresponding to $r = \alpha_p h$, where h is the mesh size and the quantity r has already been defined in Sections 4.2.1 and 4.2.2. Hence, the assumption that the fracture propagates approximately by an amount r leads to the estimate $\Delta w_{eq} \approx \alpha_p \, w_{cr}/N_{coh}$ of the crack opening increment. In our computations, it was found beneficial to take a slightly more restrictive constraint, that is:

$$\Delta w_{eq} = \frac{\alpha_p \, w_{cr}}{2 \, N_{coh}} \, , \tag{55}$$

which corresponds to allowing the fracture to propagate by $r/2$ at each loading step.

Let $\mathscr{Q}_{\tilde{\Gamma}_{coh}}$ denote the set of quadrature points q of position $\boldsymbol{x}_q$, for the edges/faces of the surrogate cohesive zone $\tilde{\Gamma}_{coh}$. The control parameter Δl in the arc-length method is defined as the norm of the vector of crack opening increments at the quadrature points on the surrogate crack:

$$\sum_{q \in \mathscr{Q}_{\tilde{\Gamma}_{coh}}} \left(\Delta w_{eq}(\boldsymbol{u}(\boldsymbol{x}_q)) \right)^2 = \Delta l^2 \tag{56a}$$

$$\Delta l^2 = n_{q_f} N_{coh} \left(\frac{\alpha_p \, w_{cr}}{2 N_{coh}} \right)^2 = \alpha_p^2 \, n_{q_f} \, \frac{h \, (1 - \nu^2)}{E \, G_F} \left(\frac{t_{cr} w_{cr}}{4} \right)^2 = \alpha_p^2 \, n_{q_f} \, h \, (1 - \nu^2) \, \frac{G_F}{E} \, , \tag{56b}$$

where n_{q_f} if the number of quadrature points per edge/face of the elements attached to the fracture surface (in two/three dimensions, respectively). Note that equation (56a) is the constraint that characterizes the size of an increment in this crack-opening arc-length control strategy, whereas equation (56b) is a mechanics-based expression for Δl obtained by combining equations (53)–(55).

Consider now a discretization of the solution (in our case, by piecewise-linear approximating finite element spaces), so that the unknown pair $(\boldsymbol{u}, \boldsymbol{\varepsilon})$ is approximated in terms of the degrees-of-freedom pair $(\mathbf{y}, \mathbf{z})$, where $\mathbf{y}$ and $\mathbf{z}$ indicate arrays of degrees of freedom. In particular, through the finite element shape functions, it holds the relation $\boldsymbol{u}(\boldsymbol{x}) = \boldsymbol{u}[\mathbf{y}](\boldsymbol{x})$ and $\boldsymbol{\varepsilon}(\boldsymbol{x}) = \boldsymbol{\varepsilon}[\mathbf{z}](\boldsymbol{x})$, where we have made explicit the dependency of $(\boldsymbol{u}, \boldsymbol{\varepsilon})$ on $(\mathbf{y}, \mathbf{z})$. Then the variational form (46) leads to an algebraic system

$$\mathbf{R}((\mathbf{y}, \mathbf{z}); \lambda) = \mathbf{F}_{int}(\mathbf{y}, \mathbf{z}) - \lambda \mathbf{F}_{ext} = 0 \, , \tag{57}$$

where $\mathbf{F}_{int}(\mathbf{y}, \mathbf{z})$ is associated with the internal mechanical forces, and $\mathbf{F}_{ext}$ is a reference external load. The parameter λ controls the amount of load applied. We present next a strategy to relate the increment $\Delta\lambda$ to Δl defined in (56), which in turns relates $\Delta\lambda$ with the fracture energy G_F, the elasticity moduli E and G, and the grid spacing h. In what follows, we will use the notation $\mathbf{x} = (\mathbf{y}, \mathbf{z})$. For a step n in the loading process, the system of equations (57) can be linearized about the iterate (i) as

$$\begin{aligned} 0 = \; & \mathbf{F}_{int}(\mathbf{x}_n^{(i)}) + \left[\frac{\partial \mathbf{F}_{int}(\mathbf{x})}{\partial \mathbf{x}} \right]_n^{(i)} \delta \mathbf{x}_n^{(i)} - (\lambda_n^{(i)} + \delta \lambda_n^{(i)}) \mathbf{F}_{ext} \\ = \; & \mathbf{R} \left(\mathbf{x}_n^{(i)}; \lambda_n^{(i)} \right) + \mathbf{K}_n^{(i)} \, \delta \mathbf{x}_n^{(i)} - \delta \lambda_n^{(i)} \mathbf{F}_{ext} \, , \end{aligned} \tag{58}$$

where $\mathbf{x}_n^{(i)} = (\mathbf{y}_n^{(i)}, \mathbf{z}_n^{(i)})$ and $\mathbf{K}_n^{(i)} = \left[\partial \mathbf{F}_{int}(\mathbf{x}) / \partial \mathbf{x} \right]_n^{(i)}$. The solution of (58) is

$$\delta \mathbf{x}_n^{(i)} = \; \delta \mathbf{x}_{int;n}^{(i)} + \delta \lambda_n^{(i)} \, \mathbf{x}_{ext;n}^{(i)} \, , \tag{59}$$

where $\delta \mathbf{x}_{int;n}^{(i)} = -[\mathbf{K}_n^{(i)}]^{-1} \, \mathbf{R} \left(\mathbf{x}_n^{(i)}; \lambda_n^{(i)} \right)$ and $\mathbf{x}_{ext;n}^{(i)} = [\mathbf{K}_n^{(i)}]^{-1} \, \mathbf{F}_{ext}$. Equation (58) needs to be solved at each iterate of the Newton-Raphson procedure associated with a specific loading step n. The overall solution and load control parameter at step n and a final iterate (I) can be expressed as

$$\mathbf{x}_n^{(I)} = \; \underbrace{\mathbf{x}_0 + \sum_{k=1}^{n-1} \Delta \mathbf{x}_k}_{\mathbf{x}_{n-1}} + \underbrace{\sum_{i=1}^{I} \delta \mathbf{x}_n^{(i)}}_{\Delta \mathbf{x}_n^{(I)}} \, , \tag{60a}$$

$$\lambda_n^{(I)} = \; \underbrace{\lambda_0 + \sum_{k=1}^{n-1} \Delta \lambda_k}_{\lambda_{n-1}} + \underbrace{\sum_{i=1}^{I} \delta \lambda_n^{(i)}}_{\Delta \lambda_n^{(I)}} \, , \tag{60b}$$

Algorithm 3 Arc-length method based on the crack opening control.

1: **while** $\|\mathbf{R}(\mathbf{x}_n^{(i)};\lambda_n^{(i)})\| > \varepsilon_{toll}\|\mathbf{R}(\mathbf{x}_n^{(0)};\lambda_n^{(0)})\|$ (with $\mathbf{R}(\mathbf{x});\lambda$) defined in (57))
2: Compute $\delta\mathbf{x}_{int;n}^{(i)} = -[\mathbf{K}_n^{(i)}]^{-1}\,\mathbf{R}\left(\mathbf{x}_n^{(i)};\lambda_n^{(i)}\right)$ and $\mathbf{x}_{ext;n}^{(i)} = [\mathbf{K}_n^{(i)}]^{-1}\,\mathbf{F}_{ext}$
3: Substitute $\delta\mathbf{x}_{int;n}^{(i)}$ and $\mathbf{x}_{ext;n}^{(i)}$ into (62) and find the two roots to the quadratic equation in $\delta\lambda_n^{(i)}$
4: **for** each of the roots $\delta\lambda_{n;1}^{(i)}$ and $\delta\lambda_{n;2}^{(i)}$
5: Compute $\delta\mathbf{x}_n^{(i)}$ using (59)
6: Update the total increments $\Delta\mathbf{x}_n^{(i)} = \Delta\mathbf{x}_n^{(i-1)} + \delta\mathbf{x}_n^{(i)}$
7: Compute $\Xi[\delta\lambda_n^{(i)}] = \Delta w_{eq,n-1}^T \Delta w_{eq,n}^{(i)}$
8: **end for**
9: **if** $\max(\Xi[\delta\lambda_{n;1}^{(i)}],\Xi[\delta\lambda_{n;2}^{(i)}]) < 0$ **then**
10: **exit the while loop**
11: **return** to line 1 and increase the arc-length radius Δl^2 (to avoid the closing of the crack)
12: **else**
13: Set $\delta\lambda_n^{(i)} = \arg\max(\Xi[\delta\lambda_{n;1}^{(i)}],\Xi[\delta\lambda_{n;2}^{(i)}])$
14: Update $\mathbf{x}_n^{(I)}$ and $\lambda_n^{(I)}$ using equations (60a) and (60b)
15: Update iterate $(i) \to (i+1)$
16: Compute the residual $\mathbf{R}(\mathbf{x}_n^{(i+1)};\lambda_n^{(i+1)})$ in equation (57)
17: **end if**
18: **end while**

where $\mathbf{x}_n^{(0)} = \mathbf{x}_{n-1}$ and $\lambda_n^{(0)} = \lambda_{n-1}$. Then (56) can be used to define the arc-length control strategy

$$\sum_{q\in\mathcal{Q}_{\tilde{\Gamma}_{coh}}} \left(w_{eq}\left(\boldsymbol{u}[\,\mathbf{y}_n^{(i-1)} + \delta\mathbf{y}_{int;n}^{(i)} + \delta\lambda_n^{(i)}\,\mathbf{y}_{ext;n}^{(i)}\,](\boldsymbol{x}_q)\right) - w_{eq}\left(\boldsymbol{u}[\,\mathbf{y}_{n-1}\,](\boldsymbol{x}_q)\right)\right)^2 = \Delta l^2\,, \tag{61}$$

where (58) has been restricted to only the unknown $\mathbf{y}$, with $\mathbf{y}_n^{(i-1)} + \delta\mathbf{y}_{int;n}^{(i)} + \delta\lambda_n^{(i)}\,\mathbf{y}_{ext;n}^{(i)} = \mathbf{y}_n^{(i)}$. Equation (61) is a quadratic equation in $\delta\lambda_n^{(i)}$ and can be recast as

$$a_1\left(\delta\lambda_n^{(i)}\right)^2 + a_2\,\delta\lambda_n^{(i)} + a_3 = 0\,, \tag{62a}$$

with

$$a_1 = \sum_{q\in\mathcal{Q}_{\tilde{\Gamma}_{coh}}} w_{eq}\left(\boldsymbol{u}[\mathbf{y}_{ext;n}^{(i)}](\boldsymbol{x}_q)\right)^2\,, \tag{62b}$$

$$a_2 = 2\sum_{q\in\mathcal{Q}_{\tilde{\Gamma}_{coh}}} \left(w_{eq}\left(\boldsymbol{u}[\,\mathbf{y}_n^{(i-1)} + \delta\mathbf{y}_{int;n}^{(i)}\,](\boldsymbol{x}_q)\right) - w_{eq}\left(\boldsymbol{u}[\,\mathbf{y}_{n-1}\,](\boldsymbol{x}_q)\right)\right) w_{eq}\left(\boldsymbol{u}[\mathbf{y}_{ext;n}^{(i)}](\boldsymbol{x}_q)\right)\,, \tag{62c}$$

$$a_3 = \sum_{q\in\mathcal{Q}_{\tilde{\Gamma}_{coh}}} \left(w_{eq}\left(\boldsymbol{u}[\,\mathbf{y}_n^{(i-1)} + \delta\mathbf{y}_{int;n}^{(i)}\,](\boldsymbol{x}_q)\right) - w_{eq}\left(\boldsymbol{u}[\,\mathbf{y}_{n-1}\,](\boldsymbol{x}_q)\right)\right)^2 - \Delta l^2\,. \tag{62d}$$

The quadratic equation (62) has in general two roots, and we select the one that satisfies the condition

$$\Xi = \Delta w_{eq,n-1}^T(\Delta w_{eq,n}^{(i-1)} + \delta w_{eq,n}^{(i)}) = \Delta w_{eq,n-1}^T \Delta w_{eq,n}^{(i)} \geq 0\,, \tag{63}$$

implying that the increment $\Delta w_{eq,n-1}$ and $\Delta w_{eq,n}^{(i)}$ must be roughly pointing in the same direction. The overall arc-length strategy is summarized in Algorithm 3

5 | NUMERICAL RESULTS

A number of computational tests in two and three dimensions are presented, with comparison with classical benchmark tests in the field.

5.1 | Two-dimensional tests

We consider here three classical examples that have been widely studied in the literature, both experimentally and numerically: the three-point bending specimen test [1,48,99], the L-shape panel test [87,88,100] and the four-point bending specimen test [48,99,101]. The first produces a straight crack path, while the other two produce curved crack paths. The tests are ordered so as to respect the increasing complexity of the nonlinear snap-back response in the case of brittle materials. The plane strain assumption is adopted for all two-dimensional numerical simulations.

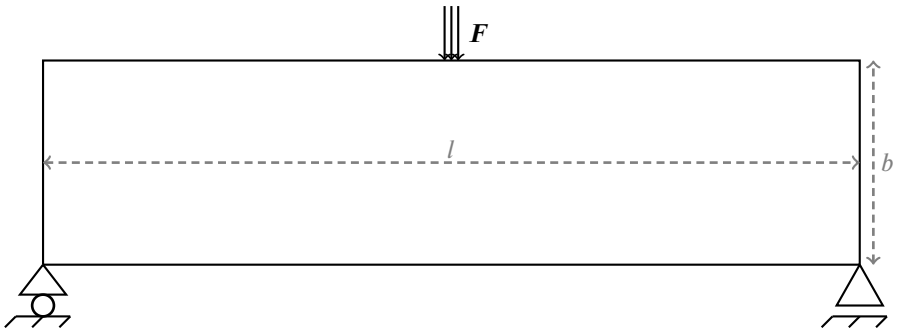

FIGURE 11 Geometry and setup of the three-point bending specimen.

5.1.1 | Three-point bending specimen

The geometry of the three-point bending specimen is shown in Figure 11 and is constituted of a rectangular beam of height $b = 0.15$ m, length $l = 4b$, and thickness $s = b$. The material properties are: $E = 36.5$ GPa, $\nu = 0.1$, $t_{cr} = 3.19$ MPa, where E is Young's modulus, ν is Poisson's ratio and t_{cr} is the normal critical stress. The load F is distributed over a strip of length 0.01 m, symmetric with respect to the midpoint of the beam. The beam is simply supported at both ends and the horizontal displacement is prevented by the right support, as shown in Figure 11. The performance of the SFM is assessed for values of the fracture energy $G_F = 5$ N/m, $G_F = 50$ N/m and $G_F = 200$ N/m, which span from brittle to ductile fracture behavior.

Four computational grids (denoted Mesh 1, 2, 3 and 4) are used in the calculations, whose details are presented in Table 1. Meshes 1, 2, 3, and 4 have an average mesh size $h = 5$ mm, $h = 2.5$ mm, $h = 1.25$ mm and $h = 0.625$ mm. Meshes 2, 3, and 4 are obtained by nested refinement of Mesh 1, and the sizes of the grids refer to a neighborhood of the crack path, since they are slightly coarsened away from it.

Meshes	Number of elements	Number of nodes	Average element size around crack path
Mesh 1	1,565	851	5 mm
Mesh 2	3,477	1,828	2.5 mm
Mesh 3	10,513	5,385	1.25 mm
Mesh 4	19,318	9,774	0.625 mm

TABLE 1 Mesh properties for the three-point bending specimen.

As the load F increases, the bottom of the mid section is the location where the principal stress first reaches the normal critical stress t_{cr}, and a crack develops upward. Because of the symmetry of the problem, the crack path is vertical.

Figure 12a shows the non-dimensional load-deflection curves for both the fully mixed formulation described in Section 3 and the fracture layer approach described in Section 3.6. The fracture energy is $G_F = 5$ N/m and induces a sharp snap-back response. For both formulations, the load-deflection curves converge to the same limit after four levels of mesh refinement. Since the fracture layer approach gives very similar results to the mixed variational formulation, we will only show results for the former from now on. Figure 12b shows that the SFM solution converges to values in very good agreement with both the

work of Carpinteri and Colombo[1], which used adaptive mesh refinement in combination with a node release technique, and of Moës and Belytschko[48], which used the XFEM. Figure 13 shows the true/surrogate crack paths and the subdomains $\tilde{\Omega}_\ell$ and

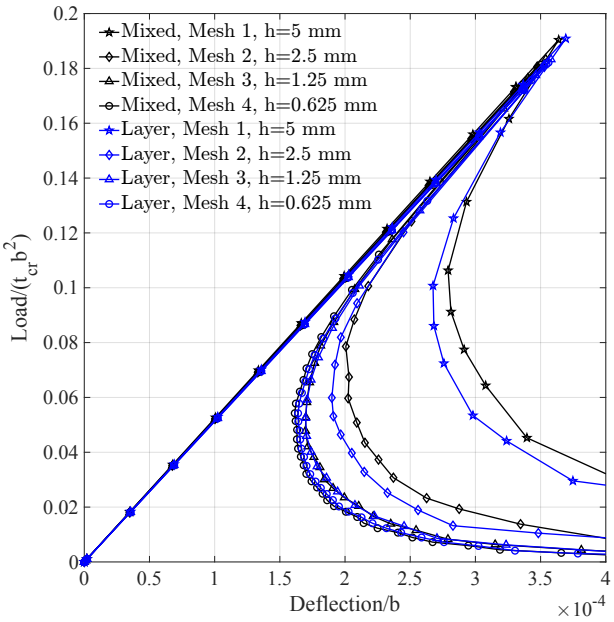

(a) Comparison between the fully mixed formulation (40) and fracture layer variational formulation (46).

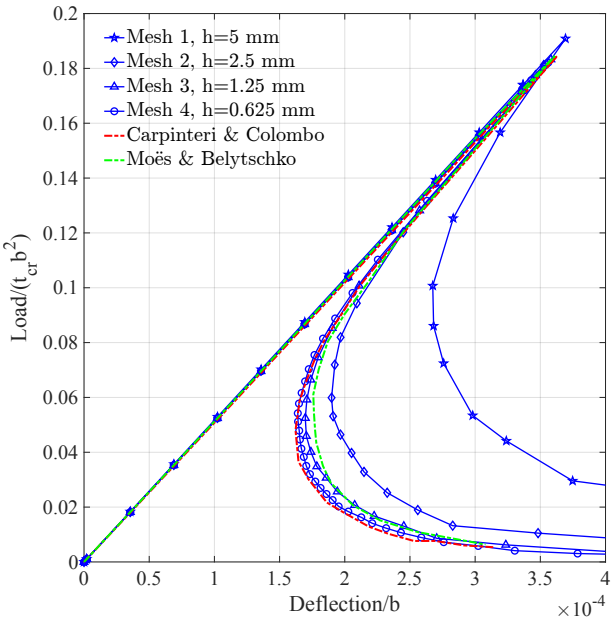

(b) Comparison of the fracture layer SFM formulation against references.

FIGURE 12 SFM computations of the three-point bending test: Non-dimensional load-deflection curves for brittle response ($G_F = 5$ N/m).

$\Omega \setminus \tilde{\Omega}_\ell$ for the fracture layer implementation of the SFM. We consider here different loading stages for Mesh 1 and again $G_F = 5$ N/m. Note that, for the SFM, the true crack path is computed from the surrogate crack path using the distance vector $\boldsymbol{d}$ and the maximal principal tensile stress criterion.

Remark 15. The SFM estimate of the true crack path is very accurate, considering that the computational grid is unstructured and without symmetries. We believe this is due to the combination of the use of a cohesive zone model, which prevents gradients to grow unbounded as the grid is refined, and the approximation properties of the Taylor expansion, which remain valid under these conditions.

It is worthwhile at this point to compare the SFM with the node-release technique (NRT), which in practice corresponds to the case of a primal (displacement-based) variational formulation of the SFM with the distance vector enforced to be $\boldsymbol{d} = \boldsymbol{0}$. Figure 14 shows a comparison of the numerical results obtained with the SFM and the NRT (the latter is clearly mesh dependent), for a fracture energy $G_F = 5$ N/m. For the NRT, the approximate crack path follows the edges of the grid, and the cohesive interface conditions are imposed on the approximate crack (depicted in green in the two plots on the left of Figure 14). As already mentioned, in the case of the SFM, the crack path is estimated from the surrogate crack path using the distance $\boldsymbol{d}$, and this results in a considerably more accurate result (marked in blue). For comparison, the black dashed line indicates the exact fracture path.

This difference in approximation has also very important consequences in the profiles of the non-dimensional load-deflection curves, shown in the right panel of Figure 14. The NRT produces large oscillations in the load-deflection curves and a large overshoot for the peak load, because the direction of propagation of the crack is highly influenced by the orientation of the candidate edges. The edges in the crack path obtained with the NRT can easily form angles between 30° and 90° with respect to the true crack direction. As a result, whether the crack propagation direction is chosen by way of stress intensity factors or maximum (averaged) principal stresses, a much larger load is required to reach the critical value t_{cr} on those edges. In this way, both overshoot and oscillations can be observed in the load-deflection curves. Instead, for the SFM, the crack direction is not tied to the edges' orientation, and, as a consequence, we obtain very smooth load-deflection curves without overshoots or

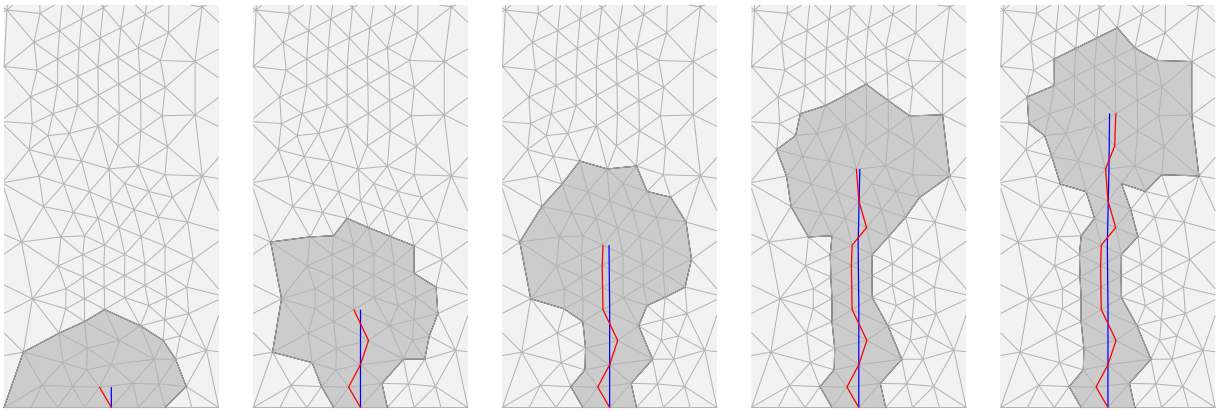

FIGURE 13 SFM computations of the three-point bending test: Crack path and layer at different stages of the fracture propagation. Simulations are performed for a brittle material ($G_F = 5$ N/m) and Mesh 1. The estimated true crack path is plotted in blue and the shifted (surrogate) crack path is plotted in red for different loading stages. The estimated true crack path is obtained by shifting the edges of the surrogate crack path by the distance vector $\boldsymbol{d}$. The dark gray area represents $\tilde{\Omega}_\ell$, the layer where the mixed SFM formulation is applied. A standard displacement-based primal formulation is applied elsewhere.

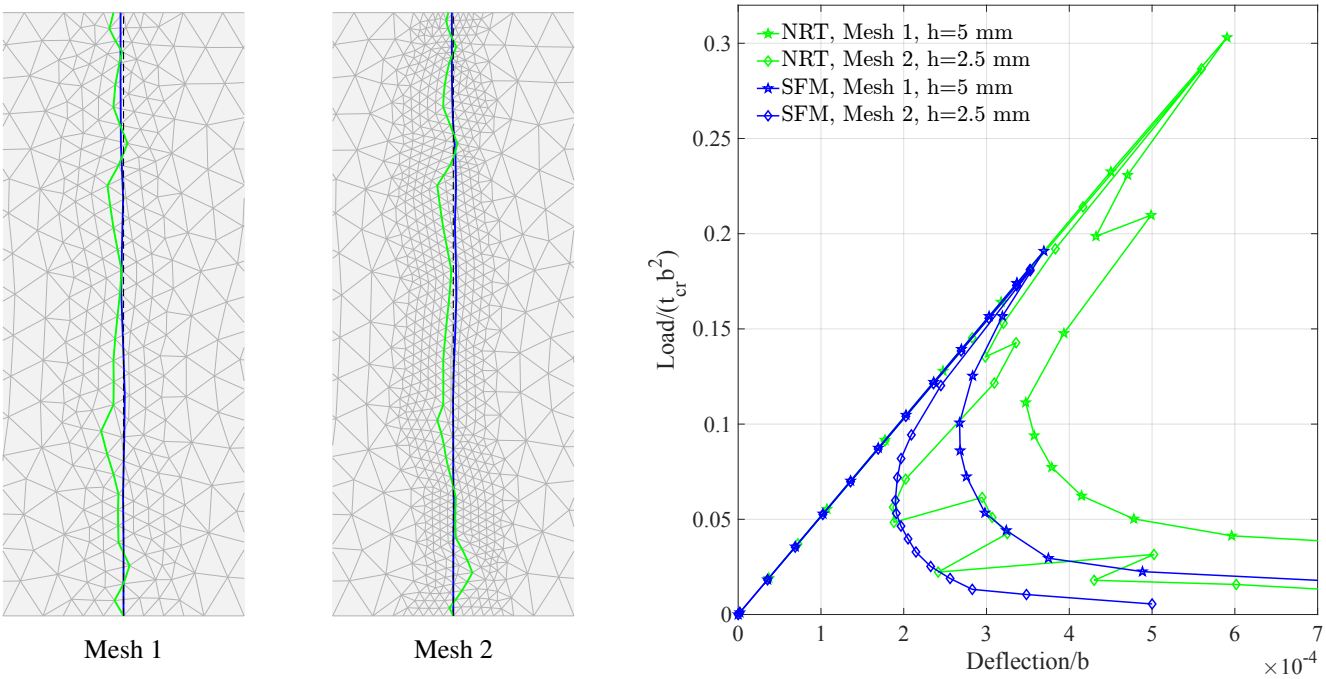

FIGURE 14 Three-point bending specimen with fracture energy $G_F = 5$ N/m. On the left, the crack path for the NRT (green) and the SFM (blue) with fracture energy $G_F = 5$ N/m on different meshes. The black dashed line shows the exact vertical crack path. On the right, the non-dimensional load-deflection curves for the NRT (green curves) and the SFM (blue curves).

oscillations. Note also that the SFM produces a very good approximation to the overall fracture surface area, because of the area correction factor $\boldsymbol{n} \cdot \tilde{\boldsymbol{n}}$ discussed in Remark 8 of Section 3.4.

The three-point bending specimen test can also be used to evaluate the accuracy of the SFM and NRT in estimating the position of the crack path at various resolutions. A measure of the error in location of the surrogate crack and the exact crack path is the shaded area shown on the left of Figure 15. An analogous definition would hold for the error between the estimated

true crack path location and the exact crack path location. A definition that encompasses all these measures of error is

$$e_p = \int_{\Gamma_p} |x_e - x_p| \, |\boldsymbol{n}_p \cdot \boldsymbol{n}_e| \, \mathrm{d}\Gamma_p \tag{64}$$

where Γ_p is a computed crack path, and x_e and x_p are the x-components of points $\boldsymbol{x}_e$ and $\boldsymbol{x}_p$ on the exact and computed crack paths $\Gamma_{c;e}$ and Γ_p, respectively. In the specific case of the SFM, (64) can be evaluated with $\Gamma_p = \tilde{\Gamma}_c$, for the surrogate crack path, or $\Gamma_p = \Gamma_c$, for the estimated true crack path. In the case of the NRT, instead, (64) can only be evaluated on $\Gamma_p = \tilde{\Gamma}_{c;\mathrm{NRT}}$, that is a fracture path composed of full edges of the grid. Note that, in general, $\tilde{\Gamma}_{c;\mathrm{NRT}} \neq \tilde{\Gamma}_c$, because of the known mesh dependencies in the selection of the fracture path in the NRT. See the left panel of Figure 15 for a visual depiction of the error e_p, represented as the shaded area between the surrogate and exact crack paths. Note also that in the case of the three-point bending specimen, the exact crack path is vertical and $\boldsymbol{n}_e = (1, 0)$.

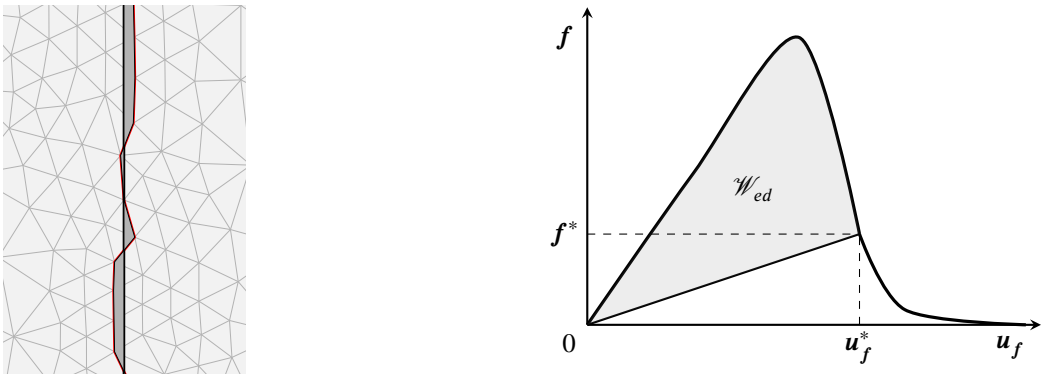

FIGURE 15 On the left, the crack position error, depicted as the dark gray area between the surrogate crack path (red) and the exact path (black). On the right, the work of external load in a load-displacement plot.

Another measure of the accuracy of the proposed approach is the error between the total dissipated fracture energy and the total work of external loads. The work of an external load $\boldsymbol{f}$ that produces a cumulative displacement $\boldsymbol{u}_f$ at its point of application can be abstractly defined as

$$\mathscr{W}_{ex} = \int_{\boldsymbol{0}}^{\boldsymbol{u}_f} \boldsymbol{f} \cdot d\boldsymbol{u} \,, \tag{65}$$

where the case of a distributed load can be handled with slight modifications. In the case of the three-point bending specimen the load is applied vertically but it is distributed over a small area, over which the work has to be integrated. Part of $\mathscr{W}_{ex}$ is dissipated by the crack and the other is stored as elastic energy in the domain. The dissipated energy by the crack can be computed as $\mathscr{W}_{ed} = \int_{\boldsymbol{0}}^{\boldsymbol{u}_f^*} \boldsymbol{f} \cdot d\boldsymbol{u} - \frac{1}{2}\boldsymbol{u}_f^* \cdot \boldsymbol{f}^*$. Once the crack has completely separated the structural specimen, all the external work would be dissipated by the crack, that is $\mathscr{W}_{ed} = \mathscr{W}_{ex}$. As shown in Figure 15, $\mathscr{W}_{ed}$ is graphically depicted as the shaded area. The energy dissipated by the crack can be calculated as the integral of the fracture energy over the surface of the crack. As shown in Figure 2, for a cohesive zone model, the dissipated energy by the crack is

$$\mathscr{W}_{cd} = \int_{\Gamma_c} \left(\int_0^{w^*} t \, dw - \frac{1}{2} t^* w^* \right) d\Gamma_c \,. \tag{66}$$

Similarly, when the crack is fully developed, $\mathscr{W}_{cd} = \int_{\Gamma_c} (\int_0^w t \, dw) d\Gamma_c \approx \int_{\tilde{\Gamma}_c} G_F \, |\tilde{\boldsymbol{n}} \cdot \boldsymbol{n}| \, d\tilde{\Gamma}_c$. Then we can introduce

$$e_{\mathscr{W}} = |\mathscr{W}_{ed} - \mathscr{W}_{cd}| \,, \tag{67}$$

that is, the misfit between the fracture energy and the work of the external load(s).

Figure 16 shows the errors e_p and $e_{\mathscr{W}}$ for the three-point bending specimen test, comparing the SFM and NRT. The left panel of the picture shows that the crack position error e_p *does not converge* for the NRT, while it converges with first-order accuracy

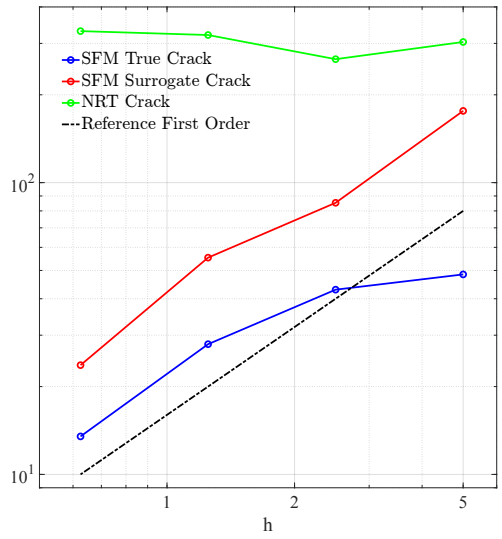

(a) Crack position error e_p.

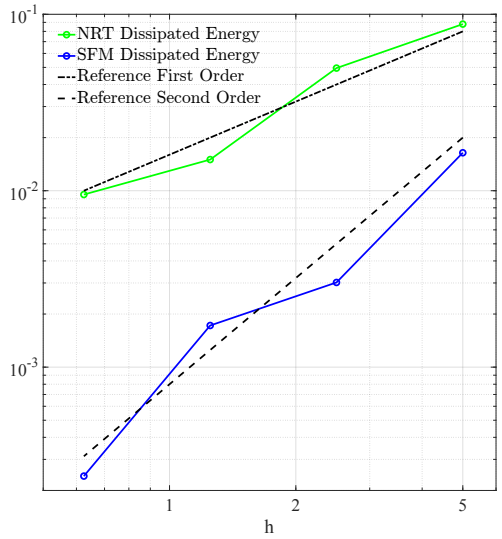

(b) Dissipated fracture energy error $e_{\mathscr{W}}$.

FIGURE 16 Three-point bending specimen: Convergence rate of the SFM and the NRT on crack position error e_p and the error in the fracture energy budget $e_{\mathscr{W}}$, for $G_F = 5$ N/m.

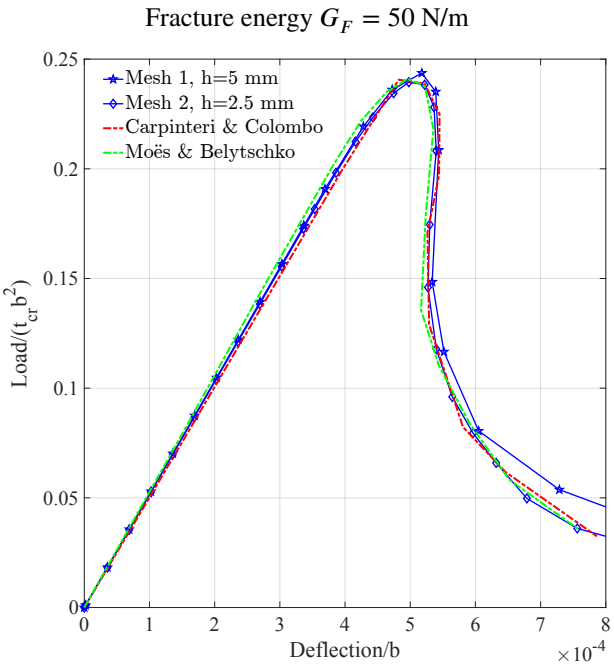

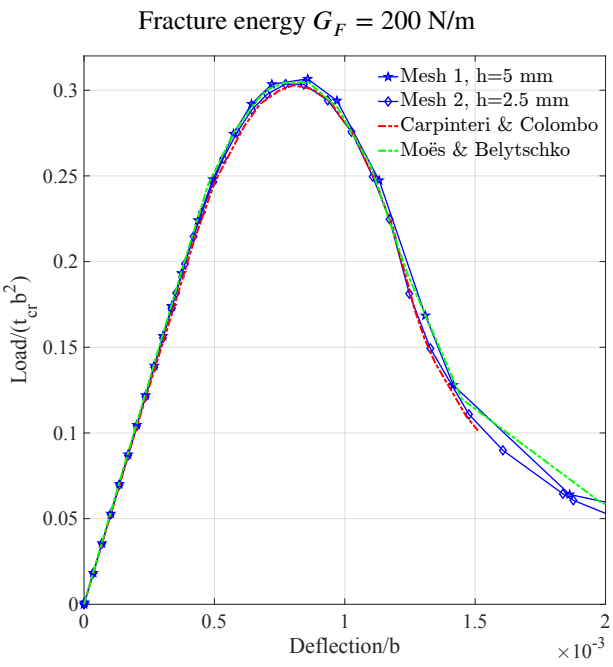

FIGURE 17 Non-dimensional load-deflection curves for the three-point bending test with fracture energy $G_F = 50$ N/m and $G_F = 200$ N/m.

for the SFM. The right panel of the picture shows that while the NRT has a first-order converging $e_{\mathscr{W}}$, the SFM provides a quadratic convergence for the same quantity.

For completeness, we show in Figure 17 the results from three-point bending specimen simulations with the SFM and higher levels of fracture energy, which induce more ductile behavior. In particular, Figure 17 shows the non-dimensional load-deflection curves with fracture energy $G_F = 50$ N/m and $G_F = 200$ N/m. Also in this case the SFM solutions agree closely with the classic references [1,48]. Similar fracture energetic considerations apply in this case.

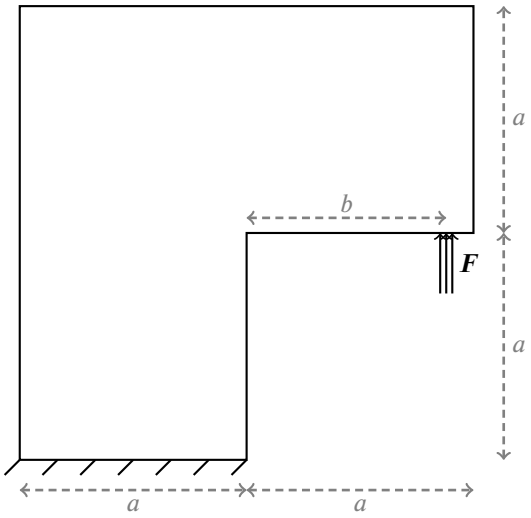

FIGURE 18 Geometry and setup of the L-shape panel.

5.1.2 | L-shape panel

In this second numerical example, a mixed-mode crack is investigated in an L-shape panel[87,88,100]. The geometry, loading and boundary conditions are shown in Figure 18, where $a = 0.25$ m, $b = 0.22$ m and the thickness $t = 0.1$ m. The material properties are Young's modulus $E = 20$ GPa, Poisson's ratio $\nu = 0.18$, fracture energy $G_F = 100$ N/m, normal critical stress $t_{cr} = 2.2$ MPa and shear effect parameter $\beta = 1.5$. The load F is distributed over a strip of length 0.01 m centered at the location indicated in Figure 18. As mentioned by references[87,88], the maximal tensile principal stress criterion of Section 4.1.1 does not produce a correct crack path for this mixed-mode L-shape panel test. In fact, for this approach, shear effects are not fully accounted for around the crack tip, leading to a less accurate direction of propagation of the crack. Therefore, the SIF approach described in Section 4.1.2 is used here to select the crack propagation direction.

Figure 19a shows the comparison of the SFM true crack path against Dumstorff and Meschke's[87] numerical result and Winkler's[100] experimental results. The SFM solution agrees well with the reference numerical result of Dumstorff and Meschke[87] and lies within the experimental uncertainty bracket of the experiments of Winkler[100]. In Figure 19b, the load-deflection curves of SFM also match the reference numerical and experimental results. Figure 19c shows a comparison of the crack paths obtained from SFM and NRT for Mesh 1. The NRT crack path does not match the experimental results. Figure 19d compares the load-deflection curves for SFM and NRT. The NRT produces a higher peak load compared with the SFM and the reference computational and experimental results.

Remark 16. The SFM estimate of the curved true crack path is fairly accurate. The cohesive zone model prevents the stress gradients to become unbounded and this in turns guarantees the validity of the Taylor expansion approach.

5.1.3 | Four-point bending specimen

Next, we consider the four point bending specimen[101], described by the setup of Figure 20. The geometrical parameters are $b = 0.2$ m, $l = 4b$, $a = 0.2b$, $c = 0.4b$ and the material properties are Young's modulus $E = 28$ GPa, Poisson's ratio $\nu = 0.1$, fracture energy $G_F = 100$ N/m, and normal critical stress $t_{cr} = 1.75$ MPa. Both loads F_1 and F_2 are distributed over a strip of length 0.02 m centered at the locations indicated in Figure 20.

Figure 21a and 21b show a comparison of the SFM crack paths for different meshes against the classical references in the literature[48,101]. As shown in Figure 21a, the curved crack paths computed with the SFM and the maximum principal tensile stress criterion agree well with the numerical results of Carpinteri *et al.*[101], in which the same criterion was used. Similarly, in Figure 21b, the SFM crack paths agree well with the XFEM computations of Moës and Belytschko[48], where in this case both methods use the SIF criterion for fracture propagation.

Figure 21c and 21d show that the load-deflection curves for both F_1 and F_2 are in good agreement with the numerical data[48,101]. In particular, when using the stress intensity factor criterion to estimate the direction of the fracture propagation,

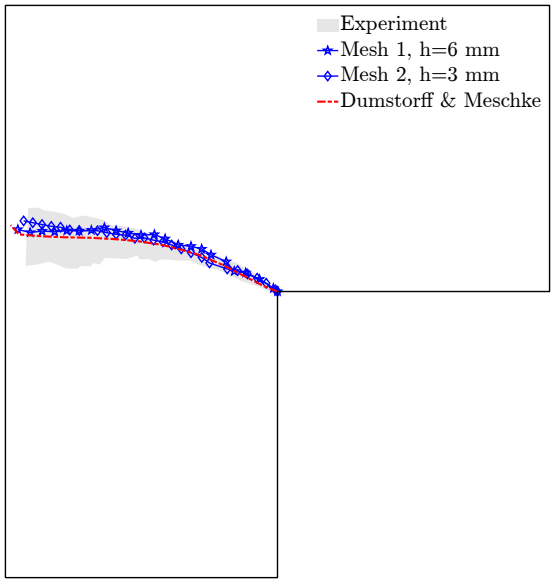

(a) SFM true crack path for the L-shape panel test with SIF.

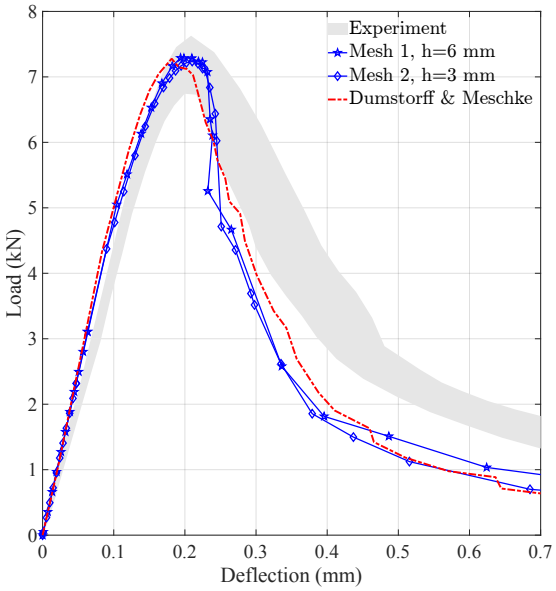

(b) Load-deflection curve for the L-shape panel test with SIF.

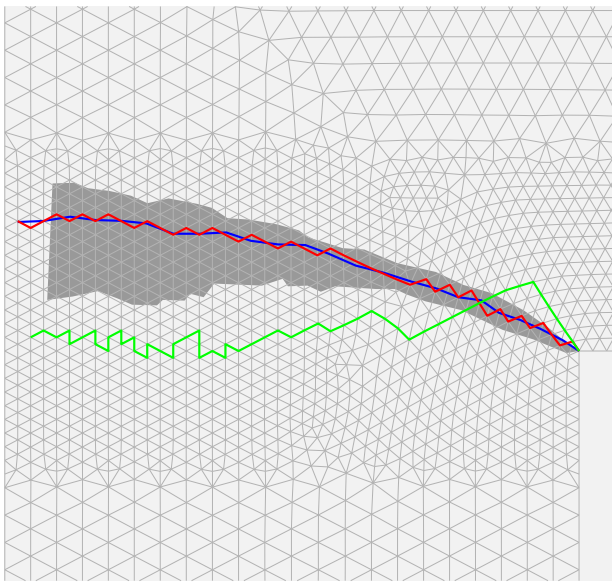

(c) SFM true crack path (blue), surrogate crack path (red) and NRT crack path (green) for the L-shape panel test.

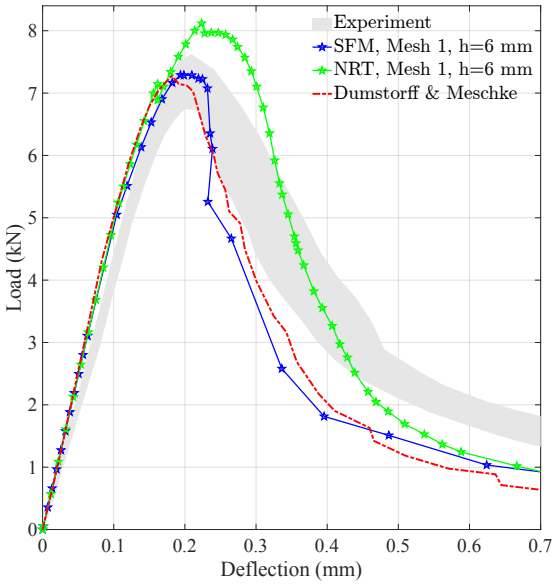

(d) SFM and NRT load-deflection curves for the L-shape panel test.

FIGURE 19 L-shape panel test[87,100]. Crack path (left) and load-deflection plot (right).

the SFM results are in very good agreement with the numerical results of[48], which also proposed stress intensity factors for propagating cracks. A very severe snap-back is observed for the $F_1 - \delta_1$ curve, where δ_1 is the deflection under the load F_1.

Figure 22 compares SFM and NRT crack paths at different loading stages on Mesh 1. Similar to previous tests, SFM provides mesh independent and overall more accurate crack paths, compared to NRT. Figure 23 shows the stress components and true crack paths at three different loading stages.

It becomes clear from this test, that the SFM, if complemented with appropriate strategies for estimating the direction of fracture propagation, is in very good agreement with results of XFEM/GFEM, while maintaining a relatively simple data structure.

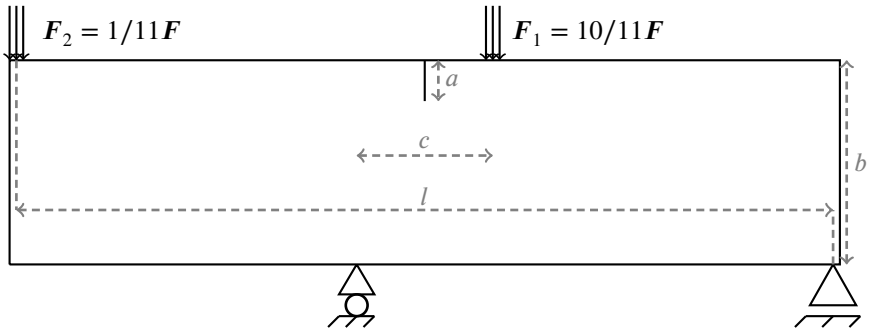

FIGURE 20 Geometry and setup of the four-point bending specimen.

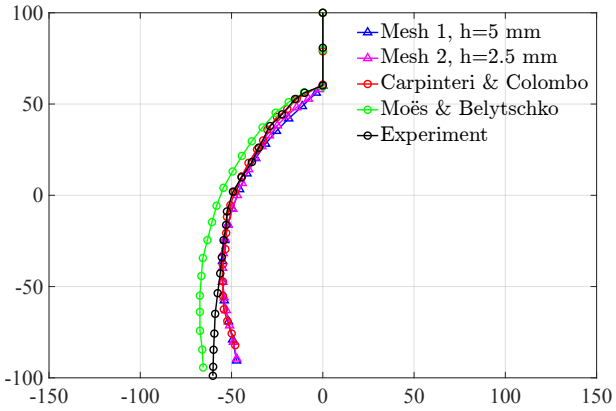

(a) SFM true crack path computed with the maximal tensile principal stress criterion.

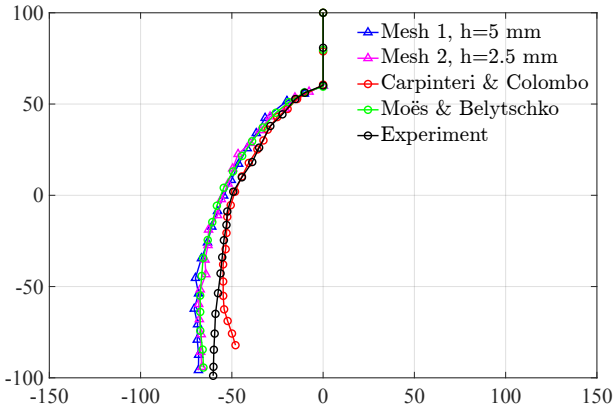

(b) SFM true crack path computed with the stress intensity factor criterion.

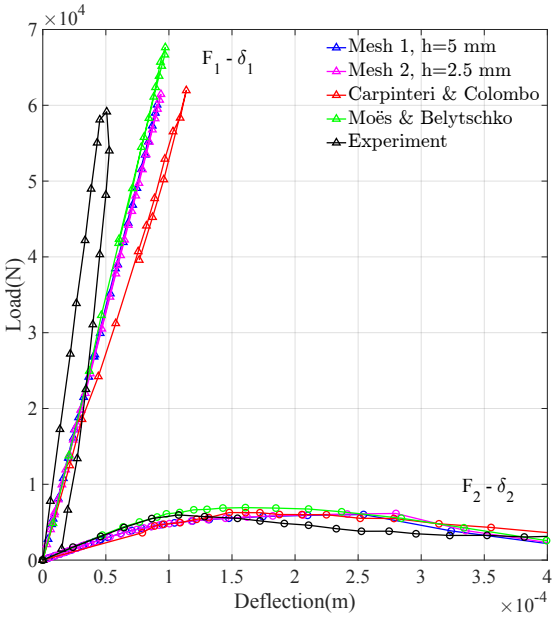

(c) Load-deflection curves for the loads F_1 and F_2 (maximal tensile principal stress criterion).

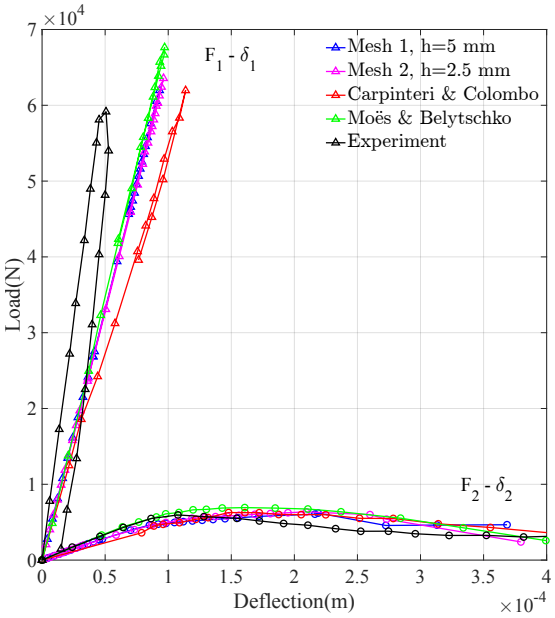

(d) Load-deflection curves for the loads F_1 and F_2 (SIF criterion).

FIGURE 21 Four point bending problem[48,101]. Crack path (left) and load-deflection plots (right). The results in Figures 21a and 21c are computed estimating the crack propagation direction with the maximum tensile principal stress criterion. The results in Figures 21b and 21d are computed estimating the crack propagation direction with the stress intensity factor (SIF) criterion.

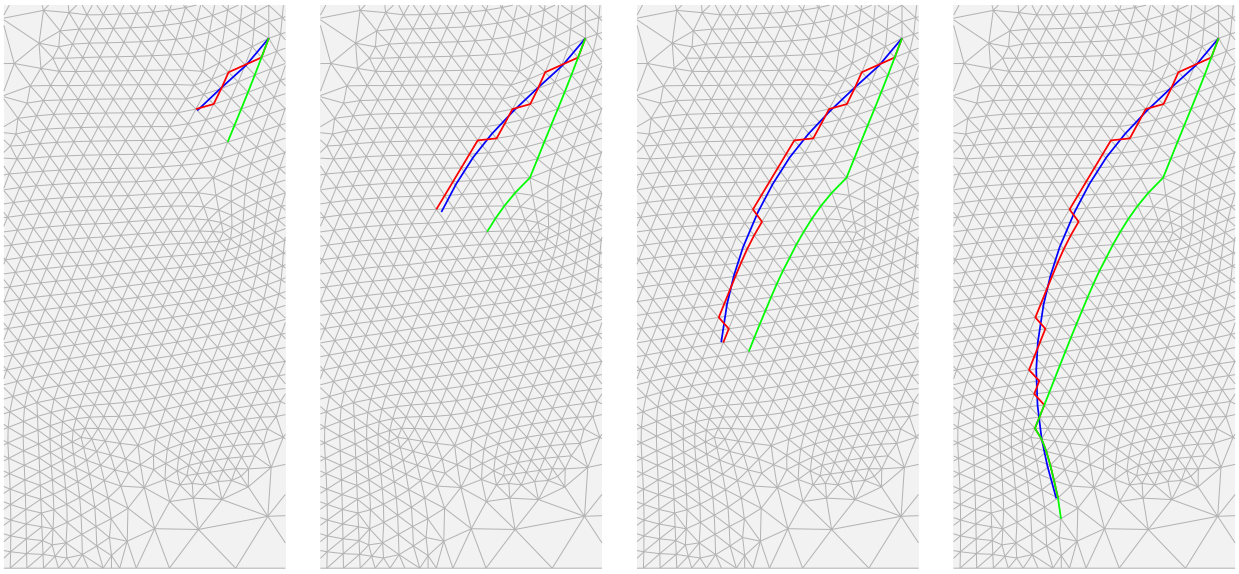

FIGURE 22 SFM true (blue) and surrogate (red) crack paths and NRT crack paths (green) at different loading stages for the four-point bending problem. The computations utilize the maximum principal tensile stress criterion for crack propagation, but analogous results can be obtained with the stress intensity factor criterion.

5.2 | Three-dimensional tests

5.2.1 | Three-point bending specimen

This example revisits the numerical test in Section 5.1.1. The material properties, boundary and loading conditions are the same, except here the third dimension about the thickness is also considered. Figure 24 shows the non-dimensional load-deflection curve with fracture energy $G_F = 50$ N/m. The result are similar to the two-dimensional version of the test. Figure 25 shows the propagation of the true (blue) and surrogate (red) crack surfaces at different loading stages. The true crack surface propagates very close to vertically. Two computational grids are employed: Mesh 1, with 5,118 elements and 1,087 nodes; and Mesh 2, with 19,130 elements and 3,657 nodes. The corresponding mesh sizes in proximity of the fracture are 13 mm and 6.5 mm, respectively.

5.2.2 | Pull-out test

Next, we consider a pull-out test of a steel anchor embedded in a cylinder concrete. The geometry and boundary conditions are shown in Figure 26. The material properties are Young's modulus $E = 30$ GPa, Poisson's ratio $\nu = 0.2$, fracture energy $G_F = 106$ N/m, normal critical stress $t_{cr} = 3$ MPa and shear effect parameter $\beta = 1.0$. Load F is applied on the green surface in Figure 26. Table 2 shows the average sizes and properties of the three meshes used in the SFM computations.

Meshes	Number of elements	Number of nodes	Average element size around crack path
Mesh 1	10,690	2,176	50 mm
Mesh 2	13,122	2,745	30 mm
Mesh 3	23,443	4,791	15 mm

TABLE 2 Mesh properties for three-dimensional pull-out test.

Figure 27a shows the comparison with the work of Gasser and Holzapfel [34], who used a nonlinear hyperelastic framework in combination with an exponential cohesive zone model, namely $t_{eq}(w_{eq}) = t_{cr} e^{-a w_{eq}^b}$, where $a = 11.323$, $b = 0.674$. For the sake of comparison, we added this model to the SFM framework we developed in the context of linear elasticity.

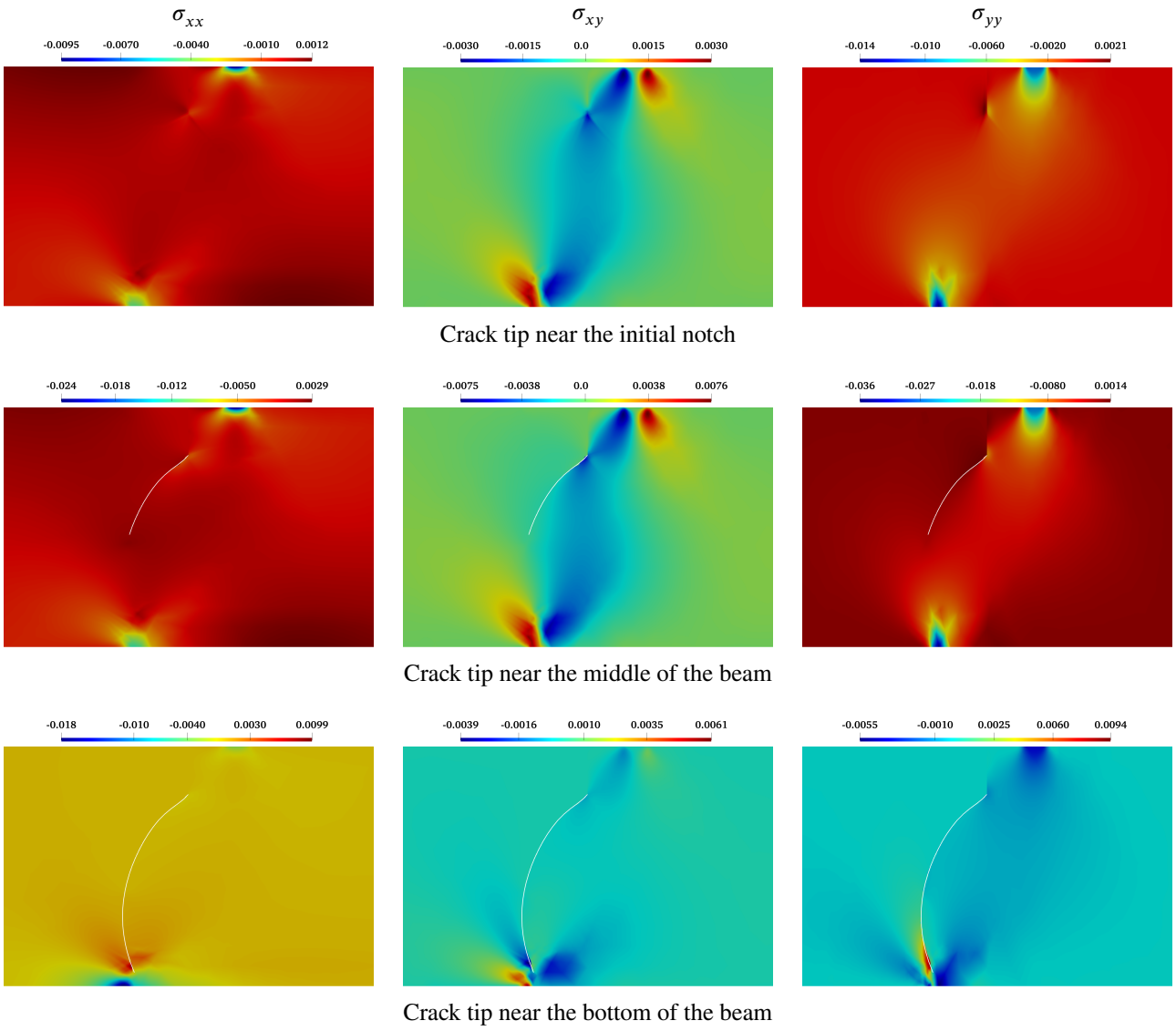

FIGURE 23 Stress distribution near the crack and true crack path (white line) at different loading stages.

As shown in Figure 27a, the SFM results with the exponential cohesive zone model and Mesh 2 seem in good agreement with the results of Gasser and Holzapfel [34], and the differences could be attributed to the fact that in this work we only consider linearly elastic media.

Figure 28 shows the propagation of the true (blue) and surrogate (red) crack surfaces at different loading stages. The true crack surface shape agrees well with the results in [34], where a cone-shaped crack is obtained.

6 | CONCLUSIONS

We have presented a new framework for computational fracture mechanics based on the idea of shifting the fracture interface conditions to a surrogate fracture composed of full edges/faces (resp., in two/three dimensions) of the grid in close proximity of the true fracture location. By appropriately modifying with Taylor expansions the interface conditions at the surrogate fracture surface, we have shown that it is possible to develop methods with accuracy comparable to XFEM/GFEM, with much simpler computational complexity.

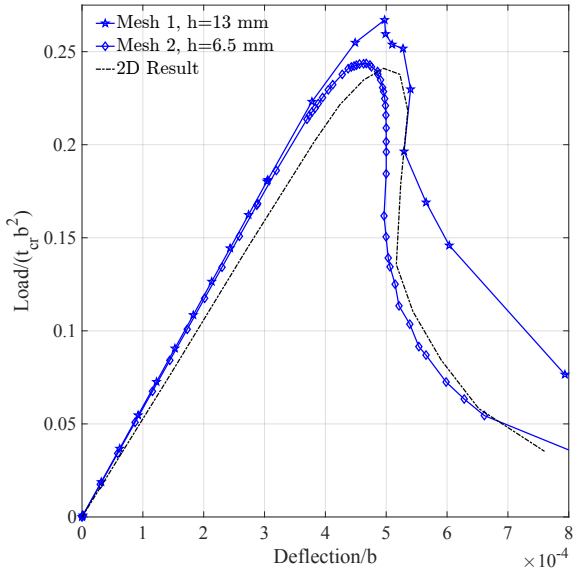

FIGURE 24 Non-dimensional load-deflection curves for the three-dimensional three-point bending specimen test with fracture energy $G_F = 50$ N/m.

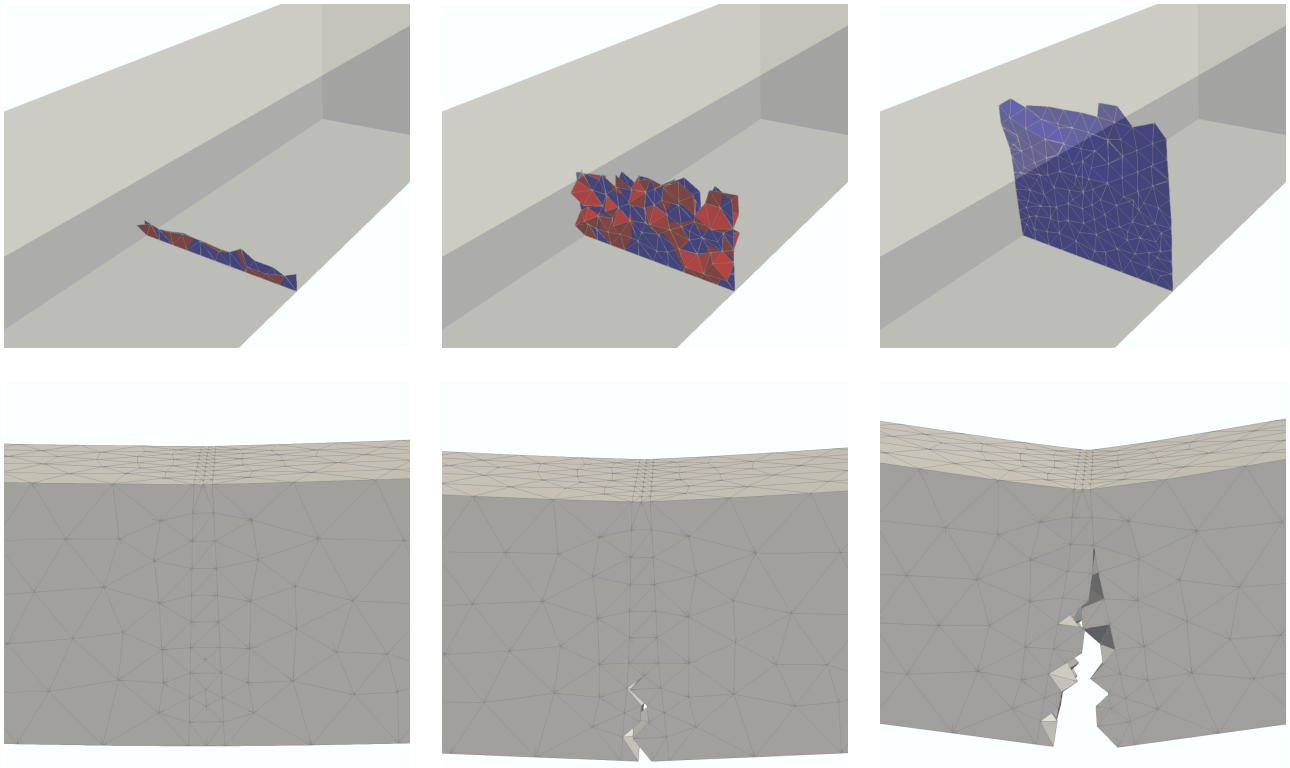

FIGURE 25 Three-dimensional three-point bending specimen test. The top row shows the crack surface (blue) and surrogate crack surface (red) at different steps in the evolution of the fracture. Observe that the estimate true surface is virtually flat and vertical. The bottom row shows a side view of the surrogate fracture surface

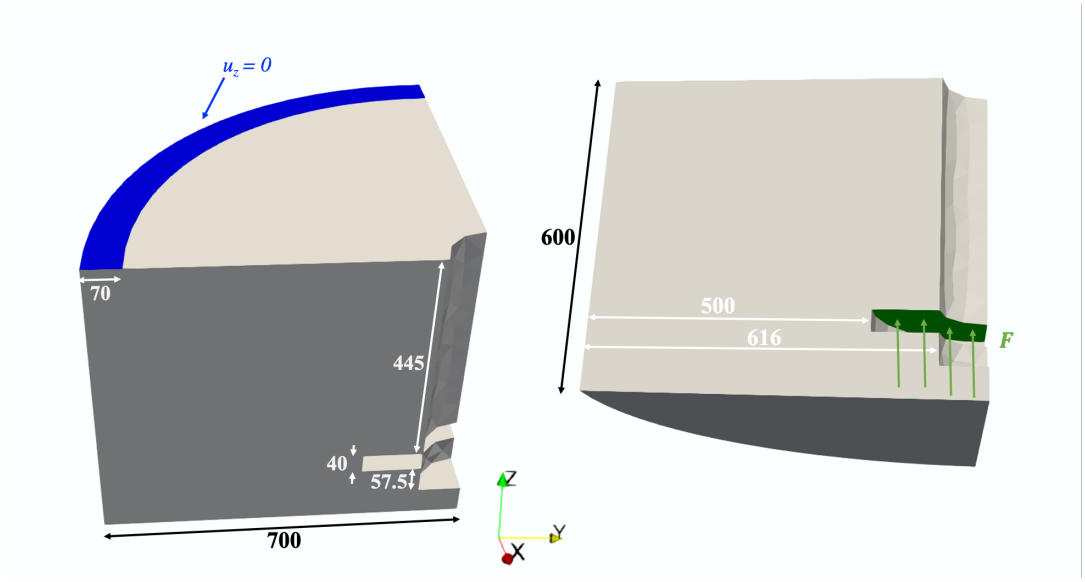

FIGURE 26 Geometry and setup of the three-dimensional pull-out test.

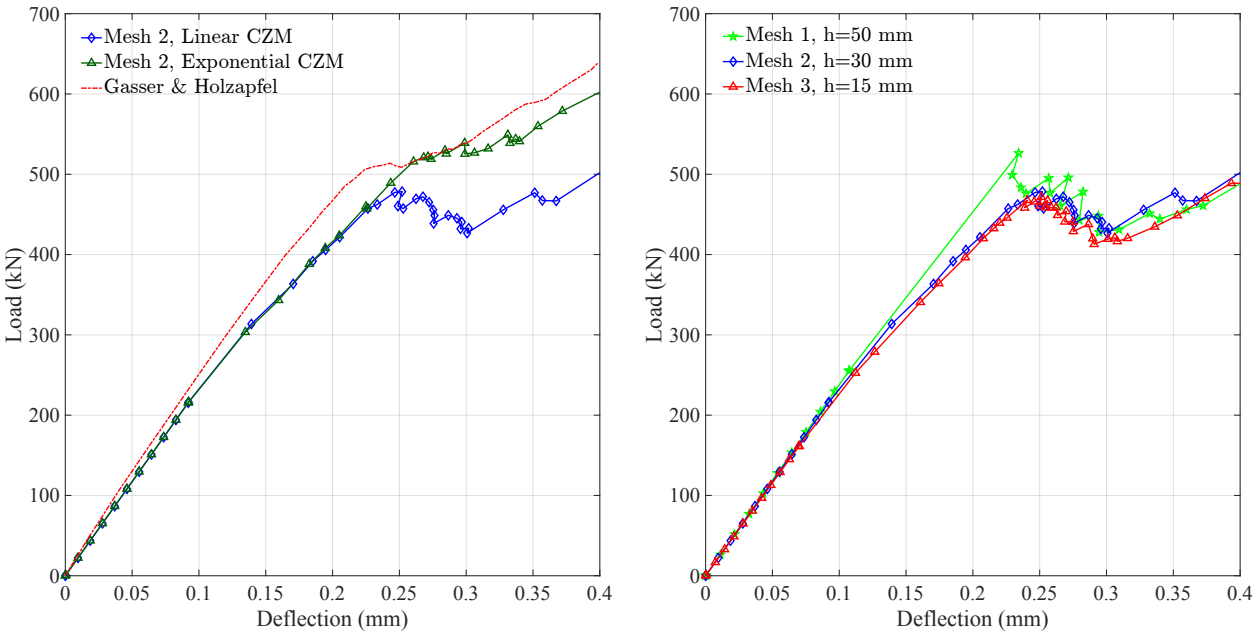

(a) Linear and exponential cohesive zone model. **(b)** SFM: Linear cohesive zone model.

FIGURE 27 Load-deflection curves for the three-dimensional pull-out test. On the left, a comparison of the exponential cohesive zone model for nonlinear elasticity of[34], against the SFM with a linearly decaying cohesive zone model. A solution for the SFM for linear elasticity combined with the exponential cohesive zone model of[34] is also shown.

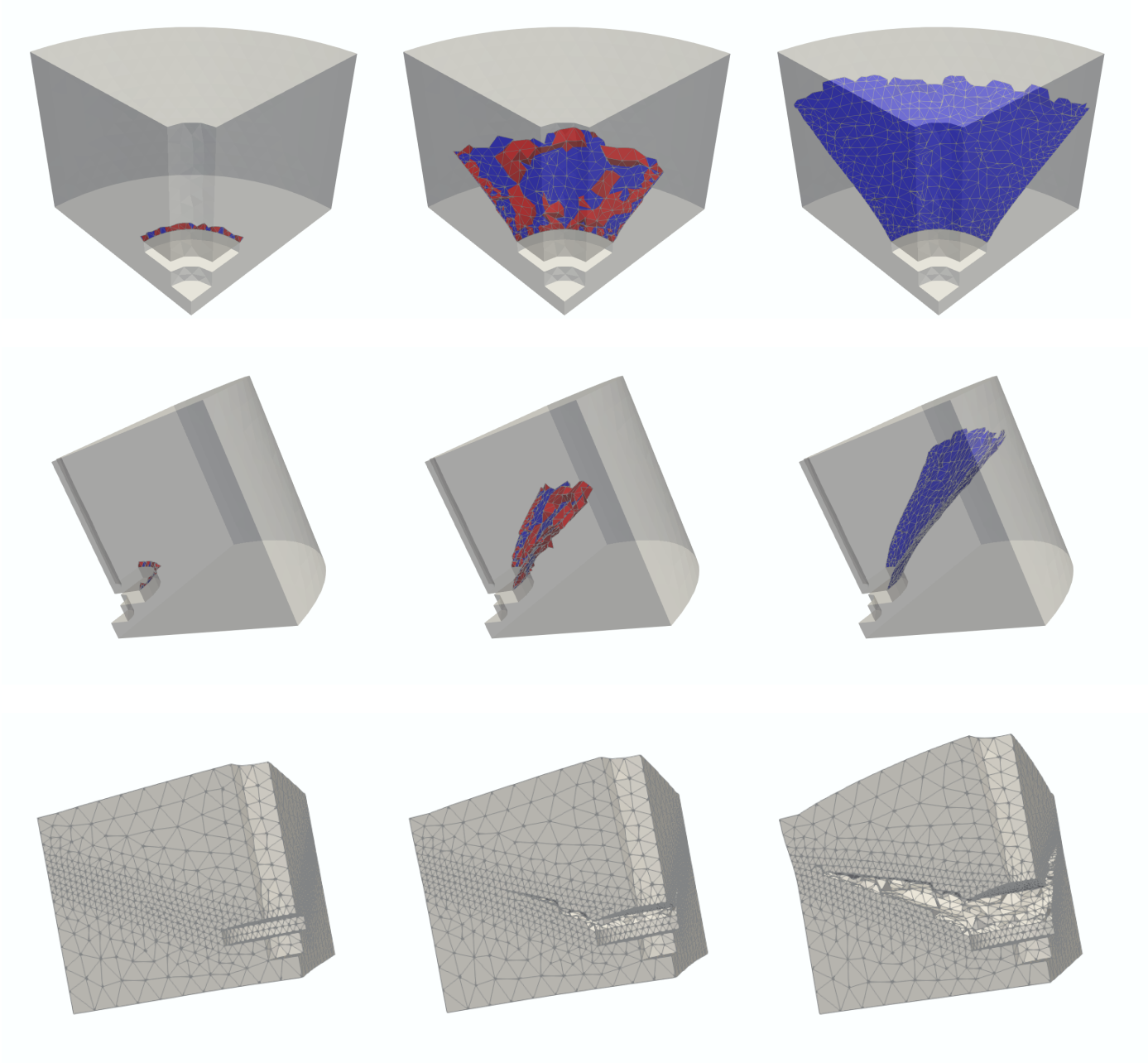

FIGURE 28 Three-dimensional pull-out test: True crack surface (blue) and surrogate crack surface (red).

We have also demonstrated, with theoretical derivations and numerical experiments, that the shifted fracture approach does not produce mesh-dependent results and is effective in capturing the energetics of the fracture. We presented an extensive suite of tests in two and three dimensions.

When considering future work, it is foreseen to explore the application of the Shifted Fracture Method to problems of crack branching and merging, which are inherently very complex. Crack branching involves the definition of the initiation criterion and the selection of propagating directions for crack branches. For example, in the context of dynamic crack branching, there is already a relatively rich theory on branching initiation criteria, based on a critical crack tip speed, and branching angles. The shifted fracture approach can be easily adapted to this case and the data structures developed in [77], for T-junction thermal

interfaces, can be appropriately modified. These are potential avenues of future development, beyond the scope of the present work.

ACKNOWLEDGMENTS

The support of the Army Research Office (ARO), under Grant W911NF-18-1-0308, and of ExxonMobil Upstream Research Company is gratefully acknowledged.

DATA AVAILABILITY STATEMENT

The data that support the findings of this study are available from the corresponding author upon reasonable request.

References

1. Carpinteri A, Colombo G. Numerical analysis of catastrophic softening behaviour (snap-back instability). *Computers & structures* 1989; 31(4): 607–636.

2. Xu XP, Needleman A. Numerical simulations of fast crack growth in brittle solids. *Journal of the Mechanics and Physics of Solids* 1994; 42(9): 1397–1434.

3. Camacho GT, Ortiz M. Computational modelling of impact damage in brittle materials. *International Journal of solids and structures* 1996; 33(20-22): 2899–2938.

4. Song JH, Wang H, Belytschko T. A comparative study on finite element methods for dynamic fracture. *Computational Mechanics* 2008; 42(2): 239–250.

5. Rangarajan R, Lew AJ. Universal meshes: A method for triangulating planar curved domains immersed in nonconforming meshes. *International Journal for Numerical Methods in Engineering* 2014; 98(4): 236–264.

6. Rangarajan R, Chiaramonte MM, Hunsweck MJ, Shen Y, Lew AJ. Simulating curvilinear crack propagation in two dimensions with universal meshes. *International Journal for Numerical Methods in Engineering* 2015; 102(3-4): 632–670.

7. Chiaramonte MM, Gawlik ES, Kabaria H, Lew AJ. Universal meshes for the simulation of brittle fracture and moving boundary problems. In: Weinberg K, Pandolfi A., eds. *Innovative numerical approaches for multi-field and multi-scale problems*Lecture Notes in Applied and Computational Mechanics, 81. Springer. 2016 (pp. 115–134)

8. Chiaramonte MM, Shen Y, Lew AJ. Mapped finite element methods: high-order approximations of problems on domains with cracks and corners. *International Journal for Numerical Methods in Engineering* 2017; 111(9): 864–900.

9. Rashid YR. Ultimate strength analysis of prestressed concrete pressure vessels. *Nuclear engineering and design* 1968; 7(4): 334–344.

10. Bažant ZP, Oh BH. Crack band theory for fracture of concrete. *Matériaux et construction* 1983; 16(3): 155–177.

11. Rots JG, Nauta P, Kuster G, Blaauwendraad J. Smeared crack approach and fracture localization in concrete. *HERON, 30 (1), 1985* 1985.

12. Rots JG. *Computational modeling of concrete fracture*. PhD thesis. Delft University of Technology, Delft (The Netherlands); 1988.

13. Oliver J, Cervera M, Oller S, Lubliner J. Isotropic damage models and smeared crack analysis of concrete. In: N. B, Mang H., eds. *Proceedings of the SCI-C Computer Aided Analysis and Design of Concrete Structures, held in Zell am See, Austria, April 4-6, 1990*Pineridge Press, Swansea, UK. ; 1990.

14. Cervera M, Chiumenti M, Codina R. Mixed stabilized finite element methods in nonlinear solid mechanics: Part I: Formulation. *Computer Methods in Applied Mechanics and Engineering* 2010; 199(37): 2559 - 2570. doi: https://doi.org/10.1016/j.cma.2010.04.006

15. Cervera M, Chiumenti M, Codina R. Mixed stabilized finite element methods in nonlinear solid mechanics: Part II: Strain localization. *Computer Methods in Applied Mechanics and Engineering* 2010; 199(37): 2571 - 2589. doi: https://doi.org/10.1016/j.cma.2010.04.005

16. Cervera M, Chiumenti M, Benedetti L, Codina R. Mixed stabilized finite element methods in nonlinear solid mechanics. Part III: Compressible and incompressible plasticity. *Computer Methods in Applied Mechanics and Engineering* 2015; 285: 752 - 775. doi: https://doi.org/10.1016/j.cma.2014.11.040

17. Lafontaine N, Rossi R, Cervera M, Chiumenti M. Explicit mixed strain-displacement finite element for dynamic geometrically non-linear solid mechanics. *Computational Mechanics* 2015; 55(3): 543–559.

18. Chiumenti M, Cervera M, Codina R. A mixed three-field FE formulation for stress accurate analysis including the incompressible limit. *Computer Methods in Applied Mechanics and Engineering* 2015; 283: 1095–1116.

19. Cervera M, Barbat G, Chiumenti M. Finite element modeling of quasi-brittle cracks in 2D and 3D with enhanced strain accuracy. *Computational Mechanics* 2017; 60(5): 767–796.

20. Barbat G, Cervera M, Chiumenti M, Espinoza E. Structural size effect: Experimental, theoretical and accurate computational assessment. *Engineering Structures* 2020; 213: 110555.

21. Cervera M, Wu JY, Chiumenti M, Kim S. Strain localization analysis of Hill's orthotropic elastoplasticity: analytical results and numerical verification. *Computational Mechanics* 2020; 65(2): 533–554.

22. Simo JC, Oliver J, Armero F. An analysis of strong discontinuities induced by strain-softening in rate-independent inelastic solids. *Computational mechanics* 1993; 12(5): 277–296.

23. Armero F, Garikipati K. An analysis of strong discontinuities in multiplicative finite strain plasticity and their relation with the numerical simulation of strain localization in solids. *International Journal of Solids and Structures* 1996; 33(20-22): 2863–2885.

24. Belytschko T, Fish J, Engelmann BE. A finite element with embedded localization zones. *Computer methods in applied mechanics and engineering* 1988; 70(1): 59–89.

25. Dvorkin EN, Cuitiño AM, Gioia G. Finite elements with displacement interpolated embedded localization lines insensitive to mesh size and distortions. *International journal for numerical methods in engineering* 1990; 30(3): 541–564.

26. Oliver J, Simo J. Modelling strong discontinuities in solid mechanics by means of strain softening constitutive equations. In: Mang H, Bicanic N, de Borst R., eds. *Computational modelling of concrete structures*Proceedings of the EURO-C Conference held in Innsbruck, Austria, 22nd-25th March 1994. Balkema, Rotterdam; 1994: 363–372.

27. Oliver J. Modelling strong discontinuities in solid mechanics via strain softening constitutive equations. Part 1: Fundamentals. *International journal for numerical methods in engineering* 1996; 39(21): 3575–3600.

28. Lotfi HR, Shing PB. Embedded representation of fracture in concrete with mixed finite elements. *International journal for numerical methods in engineering* 1995; 38(8): 1307–1325.

29. Larsson R, Runesson K. Element-embedded localization band based on regularized displacement discontinuity. *Journal of Engineering Mechanics* 1996; 122(5): 402–411.

30. Ortiz M, Leroy Y, Needleman A. A finite element method for localized failure analysis. *Computer methods in applied mechanics and engineering* 1987; 61(2): 189–214.

31. Oliver J, Huespe AE, Pulido M, Chaves E. From continuum mechanics to fracture mechanics: the strong discontinuity approach. *Engineering fracture mechanics* 2002; 69(2): 113–136.

32. Sluys L, Berends A. Discontinuous failure analysis for mode-I and mode-II localization problems. *International Journal of Solids and Structures* 1998; 35(31-32): 4257–4274.

33. Sluys L. Discontinuous modeling of shear banding. In: Proceedings of the fifth International Conference on Computational Plasticity held in Barcelona, Spain, 17th - 20th March, 1997. Int. Center for Numerical Methods in Eng., Barcelona, Spain; 1997: 735–744.

34. Gasser TC, Holzapfel GA. Geometrically non-linear and consistently linearized embedded strong discontinuity models for 3D problems with an application to the dissection analysis of soft biological tissues. *Computer Methods in Applied Mechanics and Engineering* 2003; 192(47-48): 5059–5098.

35. Areias PMA, Belytschko T. Analysis of three-dimensional crack initiation and propagation using the extended finite element method. *International Journal for Numerical Methods in Engineering* 2005; 63(5): 760-788.

36. Linder C, Armero F. Finite elements with embedded strong discontinuities for the modeling of failure in solids. *International Journal for Numerical Methods in Engineering* 2007; 72(12): 1391–1433.

37. Linder C, Armero F. Finite elements with embedded branching. *Finite Elements in Analysis and Design* 2009; 45(4): 280–293.

38. Armero F, Kim J. Three-dimensional finite elements with embedded strong discontinuities to model material failure in the infinitesimal range. *International Journal for Numerical Methods in Engineering* 2012; 91(12): 1291–1330.

39. Belytschko T, Black T. Elastic crack growth in finite elements with minimal remeshing. *International journal for numerical methods in engineering* 1999; 45(5): 601–620.

40. Moës N, Dolbow J, Belytschko T. A finite element method for crack growth without remeshing. *International journal for numerical methods in engineering* 1999; 46(1): 131–150.

41. Dolbow J, Moës N, Belytschko T. Discontinuous enrichment in finite elements with a partition of unity method. *Finite elements in analysis and design* 2000; 36(3-4): 235–260.

42. Duarte CA, Babuška I, Oden JT. Generalized finite element methods for three-dimensional structural mechanics problems. *Computers & Structures* 2000; 77(2): 215–232.

43. Duarte C, Hamzeh O, Liszka T, Tworzydlo W. A generalized finite element method for the simulation of three-dimensional dynamic crack propagation. *Computer methods in applied mechanics and engineering* 2001; 190(15-17): 2227–2262.

44. Duarte CA, Kim DJ. Analysis and applications of a generalized finite element method with global–local enrichment functions. *Computer Methods in Applied Mechanics and Engineering* 2008; 197(6-8): 487–504.

45. Belytschko T, Gracie R, Ventura G. A review of extended/generalized finite element methods for material modeling. *Modelling and Simulation in Materials Science and Engineering* 2009; 17(4): 043001.

46. Melenk JM, Babuška I. The partition of unity finite element method: basic theory and applications. *Computer methods in applied mechanics and engineering* 1996; 139(1-4): 289–314.

47. Babuška I, Melenk JM. The partition of unity method. *International journal for numerical methods in engineering* 1997; 40(4): 727–758.

48. Moës N, Belytschko T. Extended finite element method for cohesive crack growth. *Engineering fracture mechanics* 2002; 69(7): 813–833.

49. Wells GN, Sluys L. A new method for modelling cohesive cracks using finite elements. *International Journal for Numerical Methods in Engineering* 2001; 50(12): 2667–2682.

50. Wells G, Sluys L. Three-dimensional embedded discontinuity model for brittle fracture. *International Journal of Solids and Structures* 2001; 38(5): 897–913.

51. Marigo JJ, Maurini C, Pham K. An overview of the modelling of fracture by gradient damage models. *Meccanica* 2016; 51(12): 3107–3128.

52. Pham K, Amor H, Marigo JJ, Maurini C. Gradient damage models and their use to approximate brittle fracture. *International Journal of Damage Mechanics* 2011; 20(4): 618–652.

53. Pham K, Marigo JJ, Maurini C. The issues of the uniqueness and the stability of the homogeneous response in uniaxial tests with gradient damage models. *Journal of the Mechanics and Physics of Solids* 2011; 59(6): 1163–1190.

54. Bourdin B, Francfort GA, Marigo JJ. The variational approach to fracture. *Journal of elasticity* 2008; 91(1-3): 5–148.

55. Bourdin B, Francfort GA, Marigo JJ. Numerical experiments in revisited brittle fracture. *Journal of the Mechanics and Physics of Solids* 2000; 48(4): 797–826.

56. Miehe C, Hofacker M, Welschinger F. A phase field model for rate-independent crack propagation: Robust algorithmic implementation based on operator splits. *Computer Methods in Applied Mechanics and Engineering* 2010; 199(45-48): 2765–2778.

57. Miehe C, Welschinger F, Hofacker M. Thermodynamically consistent phase-field models of fracture: Variational principles and multi-field FE implementations. *International journal for numerical methods in engineering* 2010; 83(10): 1273–1311.

58. Pijaudier-Cabot G, Bažant Z. Nonlocal damage theory. *J. Eng. Mech.-ASCE* 1987; 118(10): 1512–1533.

59. Bažant Z, Jirásek M. Nonlocal integral formulations of plasticity and damage: survey of progress. *J. Eng. Mech.-ASCE* 2002; 128(11): 1119–1149.

60. Silling SA. Reformulation of elasticity theory for discontinuities and long-range forces. *Journal of the Mechanics and Physics of Solids* 2000; 48(1): 175–209.

61. Macek RW, Silling SA. Peridynamics via finite element analysis. *Finite Elements in Analysis and Design* 2007; 43(15): 1169–1178.

62. Silling SA, Lehoucq RB. Convergence of peridynamics to classical elasticity theory. *Journal of Elasticity* 2008; 93(1): 13.

63. Ha YD, Bobaru F. Studies of dynamic crack propagation and crack branching with peridynamics. *International Journal of Fracture* 2010; 162(1): 229–244.

64. Silling SA, Lehoucq RB. Peridynamic theory of solid mechanics. *Advances in applied mechanics* 2010; 44: 73–168.

65. Silling SA, Askari E. A meshfree method based on the peridynamic model of solid mechanics. *Computers & structures* 2005; 83(17-18): 1526–1535.

66. Belytschko T, Krongauz Y, Organ D, Fleming M, Krysl P. Meshless methods: an overview and recent developments. *Computer methods in applied mechanics and engineering* 1996; 139(1-4): 3–47.

67. Rabczuk T, Belytschko T. Cracking particles: a simplified meshfree method for arbitrary evolving cracks. *International Journal for Numerical Methods in Engineering* 2004; 61(13): 2316–2343.

68. Rabczuk T, Belytschko T. A three-dimensional large deformation meshfree method for arbitrary evolving cracks. *Computer methods in applied mechanics and engineering* 2007; 196(29-30): 2777–2799.

69. Mourad HM, Dolbow J, Harari I. A bubble-stabilized finite element method for Dirichlet constraints on embedded interfaces. *International journal for numerical methods in engineering* 2007; 69(4): 772–793.

70. Dolbow J, Harari I. An efficient finite element method for embedded interface problems. *International journal for numerical methods in engineering* 2009; 78(2): 229–252.

71. Harari I, Dolbow J. Analysis of an efficient finite element method for embedded interface problems. *Computational Mechanics* 2010; 46(1): 205–211.

72. Annavarapu C, Hautefeuille M, Dolbow JE. A robust Nitsche's formulation for interface problems. *Computer Methods in Applied Mechanics and Engineering* 2012; 225: 44–54.

73. Jiang W, Annavarapu C, Dolbow JE, Harari I. A robust Nitsche's formulation for interface problems with spline-based finite elements. *International Journal for Numerical Methods in Engineering* 2015; 104(7): 676–696.

74. Muixí A, Marco O, Rodríguez-Ferran A, Fernández-Méndez S. A combined XFEM phase-field computational model for crack growth without remeshing. *Computational Mechanics* 2020. doi: https://doi.org/10.1007/s00466-020-01929-8

75. Muixí A, Rodríguez-Ferran A, Fernández-Méndez S. A hybridizable discontinuous Galerkin phase-field model for brittle fracture with adaptive refinement. *International Journal for Numerical Methods in Engineering* 2020; 121(6): 1147–1169.

76. Muixí A, Fernández-Méndez S, Rodríguez-Ferran A. Adaptive refinement for phase-field models of brittle fracture based on Nitsche's method. *Computational Mechanics* 2020: 1–17.

77. Li K, Atallah NM, Main G, Scovazzi G. The Shifted Interface Method: A flexible approach to embedded interface computations. *International Journal for Numerical Methods in Engineering* 2019; 121(3): 492–518. doi: 10.1002/nme.6231

78. Main A, Scovazzi G. The Shifted Boundary Method for embedded domain computations. Part I: Poisson and Stokes problems. *Journal of Computational Physics* 2018; 372: 972–995. doi: 10.1016/j.jcp.2017.10.026

79. Bazant ZP, Planas J. *Fracture and size effect in concrete and other quasibrittle materials*. 16. CRC Press . 1997.

80. Dugdale DS. Yielding of steel sheets containing slits. *Journal of the Mechanics and Physics of Solids* 1960; 8(2): 100–104.

81. Barenblatt GI. The mathematical theory of equilibrium cracks in brittle fracture. *Advances in Applied Mechanics* 1962; 7: 55–129.

82. Hillerborg A, Modéer M, Petersson PE. Analysis of crack formation and crack growth in concrete by means of fracture mechanics and finite elements. *Cement and Concrete Research* 1976; 6(6): 773–781.

83. Atallah NM, Canuto C, Scovazzi G. The Shifted Boundary Method for solid mechanics. *International Journal for Numerical Methods in Engineering* 2021; https://doi.org/10.1002/nme.6779.

84. Margolin L. A generalized Griffith criterion for crack propagation. *Engineering fracture mechanics* 1984; 19(3): 539–543.

85. Dienes J. Comments on 'a generalized Griffith criterion for crack propagation' by LG Margolin. *Engineering Fracture Mechanics* 1986; 23(3): 615–617.

86. Ortiz M, Pandolfi A. Finite-deformation irreversible cohesive elements for three-dimensional crack-propagation analysis. *International journal for numerical methods in engineering* 1999; 44(9): 1267–1282.

87. Dumstorff P, Meschke G. Crack propagation criteria in the framework of X-FEM-based structural analyses. *International Journal for Numerical and Analytical Methods in Geomechanics* 2007; 31(2): 239–259.

88. Unger JF, Eckardt S, Könke C. Modelling of cohesive crack growth in concrete structures with the extended finite element method. *Computer methods in applied mechanics and engineering* 2007; 196(41-44): 4087–4100.

89. Atallah NM, Canuto C, Scovazzi G. The second-generation Shifted Boundary Method and its numerical analysis. *Computer Methods in Applied Mechanics and Engineering* 2020; 372: 113341.

90. Atallah N, Canuto C, Scovazzi G. Analysis of the shifted boundary method for the Poisson problem in domains with corners. *Mathematics of Computation* 2021; 90: 2041–2069.

91. Main A, Scovazzi G. The Shifted Boundary Method for embedded domain computations. Part II: Linear advection–diffusion and incompressible Navier-Stokes equations. *Journal of Computational Physics* 2018; 372: 996–1026. doi: 10.1016/j.jcp.2018.01.023

92. Masud A, Hughes TJ. A stabilized mixed finite element method for Darcy flow. *Computer Methods in Applied Mechanics and Engineering* 2002; 191(39-40): 4341–4370.

93. Hughes TJ, Masud A, Wan J. A stabilized mixed discontinuous Galerkin method for Darcy flow. *Computer Methods in Applied Mechanics and Engineering* 2006; 195: 3347–3381.

94. Brezzi F, Hughes TJ, Marini LD, Masud A. Mixed discontinuous Galerkin methods for Darcy flow. *Journal of Scientific Computing* 2005; 22(1-3): 119–145.

95. Jirásek M. Embedded crack models for concrete fracture. In: de Borst R, N. B, Mang H, G. M. , eds. *Computational modelling of concrete structures*Proceedings of the EURO-C Conference, held in Badgastein, Austria, 31 March-3 April 1998. Balkema, Rotterdam; 1998: 291–300.

96. Memon BA, Su XZ. Arc-length technique for nonlinear finite element analysis. *Journal of Zhejiang University-Science A* 2004; 5(5): 618–628.

97. Crisfield M. An arc-length method including line searches and accelerations. *International journal for numerical methods in engineering* 1983; 19(9): 1269–1289.

98. Bocca P, Carpinteri A, Valente S. Mixed mode fracture of concrete. *International Journal of Solids and Structures* 1991; 27(9): 1139–1153.

99. Rodrıguez-Ferran A, Morata I, Huerta A. Efficient and reliable nonlocal damage models. *Computer Methods in Applied Mechanics and Engineering* 2004; 193(30-32): 3431–3455.

100. Winkler BJ. *Traglastuntersuchungen von unbewehrten und bewehrten Betonstrukturen auf der Grundlage eines objektiven Werkstoffgesetzes für Beton*. Innsbruck University Press . 2001.

101. Carpinteri A, Valente S, Ferrara G, Melchiorri G. Is mode II fracture energy a real material property?. *Computers & structures* 1993; 48(3): 397–413.